Modelling Jet Trenching in Cohesive Soil

Computational Fluid Dynamics Simulation for Sedimentation Processes of Clay Particles

A.T. Schenau

TU Delft

DEME

Modelling Jet Trenching in Cohesive Soil

Computational Fluid Dynamics Simulation for Sedimentation Processes of Clay Particles

by

A.T. Schenau

to obtain the degree of Master of Science
at the Delft University of Technology,
to be defended publicly on Tuesday May 14, 2024 at 10:00 AM.

Student number:	4486099	
Project duration:	September 1, 2022 – May 14, 2024	
Thesis committee:	Dr. ir. G. H. Keetels,	TU Delft, Chairman
	Dr. ir. S. M. S. Alhaddad,	TU Delft, Committee member
	Ir. Q. Bourdos,	DEME Offshore NL, Supervisor
	Ir. H.S. Daanen,	DEME Offshore NL, daily supervisor

TU Delft

Abstract

Jet trenching operations in sandy seabeds have been extensively studied and are well understood, offering a preferred method for offshore cable installation due to its relatively low environmental impact. However, the transition to clay seabeds presents significant challenges, demanding a deeper comprehension of jet trenching dynamics in cohesive soils. Recognizing this need, DEME NL Offshore, a Dutch company specializing in offshore operations, seeks to develop a predictive model tailored for jet trenching in cohesive soil environments.

This thesis addresses the complexity of jet trenching in clay seabeds through a comprehensive computational fluid dynamics (CFD) modelling approach. Beginning with an extensive literature review, various methods for modelling jet trenching processes are explored, highlighting the critical parameters influencing trenching outcomes. While existing models primarily focused on jet penetration depth, this study identifies the need to integrate fluid dynamics principles and particle behavior to achieve a better understanding of jet trenching dynamics. A CFD model is developed to cover the fluid dynamics in the trench behind the jetting sword. Subsequently, a langrangian model is applied to determine the trajectory of cohesive particles of different diameter in the trench.

Key Findings:

- For the scenarios considered in this thesis, jet trenching in clay soils is not feasible by the accumulation of particles at the trench bottom before the cable touchdown point.
- Particle diameter significantly influences trenching outcomes, underscoring the importance of further investigation.
- Existing models inadequately account for clay block formation and behavior, indicating a gap in understanding.
- Empirical validation and field testing are essential to enhance model accuracy and reliability.
- Integration of field observations and experimental data can refine the model for real-world scenarios.

In response to these findings, recommendations for future research endeavors are proposed, emphasizing the importance of empirical validation and field testing to enhance model accuracy and reliability. By integrating field observations and experimental data, trenching models can be refined to better predict real-world trenching scenarios, thereby optimizing offshore cable installation processes.

In conclusion, this thesis contributes valuable insights into the challenges of jet trenching operations in cohesive seabeds and lays the groundwork for future research in the field. By addressing the recommendations outlined herein, future endeavors can advance trenching methodologies, ultimately improving the efficiency, reliability, and sustainability of offshore cable installation.

Preface

I am excited to present my MSc thesis, the result of months of dedicated effort. I am grateful to my committee members, Dr. ir. G. H. (Geert) Keetels and Dr. ir. S. M. S. (Said) Alhaddad, for their support and guidance, and to my supervisors, ir. Q. (Quentin) Bourdos and ir. H.S. (Erik) Daanen from DEME Offshore NL, for their support, guidance and commitment.

I also wish to remember my second supervisor, Prof. Dr. Ir. C. (Cees) van Rhee, whose initial insights were invaluable. His passing is deeply felt.

My sincere appreciation goes to my family, girlfriend and friends for their support throughout this journey.

A.T. Schenau
Delft, May 6, 2024

Contents

Abstract iii

Preface v

Nomenclature xviii

1 Introduction 1
- 1.1 Background and Motivation . . . 1
- 1.2 Problem Statement and Research Questions . . . 3
- 1.3 Scope and Limitations . . . 3
- 1.4 Thesis Outline . . . 4

Abstract Literature Review 5

Literature Review 7

2 Theoretical Background 9
- 2.1 Overview of Jet Trenching Technique . . . 9
- 2.2 Soil Characteristics of Cohesive Soils . . . 12
  - 2.2.1 Soil Particle Size . . . 12
  - 2.2.2 Definition of Soil Parameters . . . 13
  - 2.2.3 Plasticity . . . 15
  - 2.2.4 Undrained Shear Strength . . . 15

3 Cutting Depth of a Single Jet in Cohesive Soils 17
- 3.1 Principle of a Stationary Jet in Cohesive Soils . . . 18
  - 3.1.1 Flow Field of a Free Jet . . . 18
  - 3.1.2 Cavitating Jets . . . 19
  - 3.1.3 Stagnation Pressure . . . 20
  - 3.1.4 Penetration Depth of a Stationary Jet . . . 21
  - 3.1.5 Time Dependent Jet Erosion . . . 22
- 3.2 Previous Research on Moving Vertical Jets in Cohesive Soils . . . 22
  - 3.2.1 Failure Mechanisms of Clay Exposed to a Moving Jet . . . 22
  - 3.2.2 Failure Modes of Clay Exposed to a Moving Jet . . . 24
  - 3.2.3 Moving Penetrating Jet Modelling . . . 24
  - 3.2.4 Comparison of Different Theories and Experiments . . . 32

4 Sedimentation of Cohesive Material 33
- 4.1 Settling Velocity . . . 34
  - 4.1.1 Stokes' Law . . . 34
  - 4.1.2 Hindered Settling . . . 35
  - 4.1.3 Settling Velocity of Particles of Different Size and Shape . . . 35
  - 4.1.4 Settling Velocity of Clay Particles . . . 36
- 4.2 Sediment Transport . . . 37
  - 4.2.1 Camp Based Model . . . 37
  - 4.2.2 Influence of Turbulence . . . 40
- 4.3 Clay Block Formation in between the Nozzles . . . 41

5 Conclusions of Literature Review 43

6 Methodology 45
- 6.1 Computational Fluid Dynamics (CFD) . . . 46
  - 6.1.1 Governing Equations . . . 46
  - 6.1.2 CFD Operation . . . 46

6.2 Introducing openFOAM . . . 47
6.2.1 Core Features . . . 48
6.2.2 Solvers . . . 48
6.3 Simulation Setup and Boundary Conditions . . . 50
6.3.1 Geometry Definition . . . 50
6.3.2 Boundary Conditions . . . 52
6.3.3 Mesh Generation. . . . 53
6.3.4 Pump Pressure and Flow Velocity . . . 55
6.4 Simulation of Particle Motion . . . 56
6.4.1 Verlet Integration . . . 56
6.4.2 Application of Verlet Integration . . . 56
6.5 Simulation of Particle Motion at the Bottom of the Trench . . . 57
6.5.1 Shields Parameter . . . 57
6.5.2 Simulation of the Particle Motion . . . 58

7 Simulation Results and Analysis 59
7.1 Initial Conditions . . . 60
7.1.1 Initial Conditions Simulation . . . 60
7.1.2 Initial Conditions Particle Trajectory Integration . . . 61
7.2 Simulation Results . . . 61
7.2.1 Running openFOAM simulation . . . 61
7.2.2 Visualising Results . . . 62
7.3 Post-Processing . . . 64
7.3.1 Setting Up the Flow Field. . . . 64
7.3.2 Checking Shields Criterion . . . 64
7.3.3 Verlet Integration . . . 65
7.3.4 Sensitivity Analysis . . . 65
7.4 Interpretation of Results . . . 68
7.5 Loss of Burial Depth . . . 70

8 Conclusions & Recommendations 73
8.1 Conclusions & Discussion. . . . 74
8.2 Recommendations . . . 75

Bibliography 78

Appendices 79

A Equipment CBT 1100 81

B Geometry 85

C Validation Flowfield 87

D Visualization Results 89

E Post-Processing 93

F Loss of Burial Depth 101

G Python Code 105

List of Figures

1.1 Inter array & export cables (DEME, 2021) . . . 1
1.2 Different methods of cable burial (Brunning and Machin, 2014) . . . 2
1.3 Processes during jet trenching . . . 7

2.1 Jet trenching equipment . . . 9
2.2 Schematic illustration of a jetting sword (Njock et al., 2020) . . . 10
2.3 Jet trenching principle (Njock et al., 2020) . . . 10
2.4 Trench profile (Srinil, 2016) . . . 11
2.5 Grain size distribution (Lodhi et al., 2017) . . . 13

3.1 Flow field of a jet in free water (Nobel, 2013) . . . 18
3.2 Cavitation of a free jet (Nobel, 2013) . . . 19
3.3 Jet impact and stagnation pressure (Blevins, 1984) . . . 20
3.4 Time dependence cavity depth (Machin et al., 2011) . . . 22
3.5 Loading conditions of single moving jet (Nobel, 2013) . . . 23
3.6 Non-deflection and deflection zone (Nobel, 2013) . . . 23
3.7 Vertical penetrating moving jet: (a) overview (b) horizontal cross section (c) vertical cross section (Nobel, 2013) . . . 25
3.8 Jet soil interface (Zhang, Ge, et al., 2016) . . . 27
3.9 Fluid velocity and cavity shape (Wang et al., 2021) . . . 29
3.10 Typical cavity shape of a penetrating jet (Nobel, 2013) . . . 31
3.11 Conical shaped cavities of penetrating jets . . . 31

4.1 Free-body diagram of a sphere in a quiescent fluid (Shearer and Hudson, 2008) . . . 34
4.2 Settling velocity for $w_{mud,max} = 0.001\ \mathrm{m\,s^{-1}}$ and $w_{mud,min} = 0.0001\ \mathrm{m\,s^{-1}}$ . . . 37
4.3 Ideal settling tank according to Camp (Van Rhee, 2017) . . . 38
4.4 Camp based model for jet trenching . . . 39
4.5 DOC and DOL with Camp based model . . . 39
4.6 Clay blocks mechanism (Machin et al., 2011) . . . 41
4.7 Clay blocks during jet trenching in clay (photo: DEME) . . . 41
4.8 Logarithmic interpolation required flow velocity (Cathie, 2018) . . . 42

6.1 3D geometry of trench behind the 2.1 [m] jetting swords . . . 50
6.2 3D geometry of nozzles inside the 2.1 [m] trench . . . 52
6.3 Sideview of the mesh 2.1 [m] trench . . . 54
6.4 Refinement of the mesh close to the nozzles 2.1 [m] trench . . . 54
6.5 Pump working point (DEME, 2021) . . . 55
6.6 Critical shields parameter as a function of particle diameter (Cao et al., 2006) . . . 57

7.1 Side view of trench profile with starting position lines . . . 61
7.2 Flow velocity direction scenario 4 . . . 63
7.3 Imported data paraView scenario 4 . . . 64
7.4 Representation of the flowfield in `Python` scenario 4 . . . 64
7.5 Wall shear stress along the bottom of the trench scenario 4 . . . 65
7.6 Shields parameter along the bottom of the trench scenario 4 . . . 65
7.7 Path of a single particle with diameter 50 mm scenario 4 . . . 65
7.8 Paths of multiple particles with diameter 50 mm scenario 4 . . . 66
7.9 Detailed paths of multiple particles with diameter 50 mm scenario 4 . . . 66
7.10 Shields parameter along the bottom of the trench for multiple diameters scenario 4 . . . 67

7.11 Trajectories of particles with different particle size scenario 4 67
7.12 Trajectory of particles with different particle size and cable shape scenario 4 (cable 1) 69
7.13 Trajectory of particles with different particle size and cable shape scenario 4 (cable 2) 69
7.14 Trajectory of particles with different particle size and cable shape scenario 4 (cable 3) 69
7.15 Trench profile & touchdown point scenario 1 (cable 1) 70
7.16 Trench profile & touchdown point scenario 2 (cable 1) 70
7.17 Trench profile & touchdown point scenario 3 (cable 1) 71
7.18 Trench profile & touchdown point scenario 4 (cable 1) 71

B.1 Side view trench 1.5 [m] 86
B.2 Top view trench 1.5 [m] 86

C.1 Validation flowfield sand particle 1 88
C.2 Validation flowfield sand particle 2 88
C.3 Validation flowfield sand particle 3 88
C.4 Validation flowfield sand particle 4 88

D.1 Flow velocity magnitude scenario 1 90
D.2 Flow velocity direction scenario 1 90
D.3 Flow velocity magnitude scenario 2 91
D.4 Flow velocity direction scenario 2 91
D.5 Flow velocity magnitude scenario 3 92
D.6 Flow velocity direction scenario 3 92

E.1 Imported data paraView scenario 1 94
E.2 Imported data paraView scenario 2 94
E.3 Imported data paraView scenario 3 94
E.4 Representation of the flowfield in `Python` scenario 1 95
E.5 Representation of the flowfield in `Python` scenario 2 95
E.6 Representation of the flowfield in `Python` scenario 3 95
E.7 Trajectories of particles with different particle size scenario 1 96
E.8 Trajectories of particles with different particle size scenario 2 96
E.9 Trajectories of particles with different particle size scenario 3 96
E.10 Trajectory of particles with different particle size and cable shape scenario 1 (cable 1) 97
E.11 Trajectory of particles with different particle size and cable shape scenario 1 (cable 2) 97
E.12 Trajectory of particles with different particle size and cable shape scenario 1 (cable 3) 97
E.13 Trajectory of particles with different particle size and cable shape scenario 2 (cable 1) 98
E.14 Trajectory of particles with different particle size and cable shape scenario 2 (cable 2) 98
E.15 Trajectory of particles with different particle size and cable shape scenario 2 (cable 3) 98
E.16 Trajectory of particles with different particle size and cable shape scenario 3 (cable 1) 99
E.17 Trajectory of particles with different particle size and cable shape scenario 3 (cable 2) 99
E.18 Trajectory of particles with different particle size and cable shape scenario 3 (cable 3) 99

F.1 Trajectory of particles with different particle size and cable shape scenario 1 (cable 1) 102
F.2 Trajectory of particles with different particle size and cable shape scenario 1 (cable 2) 102
F.3 Trajectory of particles with different particle size and cable shape scenario 2 (cable 1) 103
F.4 Trajectory of particles with different particle size and cable shape scenario 2 (cable 2) 103
F.5 Trajectory of particles with different particle size and cable shape scenario 3 (cable 1) 104
F.6 Trajectory of particles with different particle size and cable shape scenario 3 (cable 2) 104

List of Tables

2.1 Grain size diameter D_p (NEN), (Verruijt, 2001) . . . 12
2.2 Main properties of most common clays (Mitchell and Soga, 2005) . . . 12
2.3 Typical values for hydraulic conductivity (Verruijt, 2001) . . . 13
2.4 Variation measured undrained shear strength for different tests (data from Nobel (2013)) . . . 16

3.1 Different values factor f . . . 21
3.2 Different test apparatus . . . 32

7.1 Jet setting scenarios . . . 60
7.2 Cables included in the research . . . 68

Listings

G.1 Import packages . . . 105
G.2 Import data . . . 105
G.3 Wall shear stress . . . 105
G.4 Setting up flowfield . . . 105
G.5 Functions . . . 106
G.6 Simulation for clay blocks . . . 107
G.7 Flow path of clay particles of different diameter . . . 107
G.8 Cable definition and plots . . . 109
G.9 Cable range . . . 110
G.10 Cable range . . . 111

Nomenclature

Abbreviations

CFD	Computational Fluid Dynamics
CSV	Comma-Seperated Values
DOC	Depth of Cover
DOL	Depth of Lowering
$ODEs$	Ordinary Differential Equations
ROV	Remotely Operated Vehicle
SOD	Stand-Off Distance
STL	Stereolithography
WTG	Wind Turbine Generator

Greek Symbols

$\alpha_1, \alpha_2, \alpha_3$	Constants depending on $w_{mud,max}$ and $w_{mud,min}$	-
Δt	Time between cycles	s
Δx	Distance travelled by jet before failure	m
η	Dynamic viscosity	Pa s
γ'	Submerged unit weight	$\mathrm{kg\,m^{-3}}$
Γ	Diffusion coefficient	-
γ	Volumetric weight	$\mathrm{kg\,m^{-3}}$
Γ_x	Horizontal diffusion coefficient	-
Γ_y	Vertical diffusion coefficient	-
∇	Divergence operator	-
ν	Kinematic viscosity	$\mathrm{m^2\,s^{-1}}$
ρ_f	Density of the fluid	$\mathrm{kg\,m^{-3}}$
ρ_p	Density of solid particles	$\mathrm{kg\,m^{-3}}$
ρ_s	Density of the particle	$\mathrm{kg\,m^{-3}}$
ρ_s	Specific density	$\mathrm{kg\,m^{-3}}$
ρ_w	Density of water	$\mathrm{kg\,m^{-3}}$
σ'	Effective stress	Pa
σ	Total stress	Pa
σ_1	Major principle stress	Pa

σ_3	Minor principle stress	Pa
τ_b	Bed shear stress	Pa
τ_p	Peak shear stress	Pa
τ_y	Shear stress	Pa
$\triangle$	Specific density	-
ζ	Empirical constant with units of velocity	$\mathrm{m\,s^{-1}}$

Roman Symbols

$\frac{dh}{ds}$	Hydraulic gradient	-
$\mathbf{u}$	Fluid velocity vector	$\mathrm{m\,s^{-1}}$
a, b, c	Longest, intermediate and shortest particle axis (Dietrich, 1982)	m
a, b, c, k	Emperical constants (Zhang, Ge, et al., 2016)	-
A_s	Specific surface	$\mathrm{m^2\,g^{-1}}$
B_{size}	Length of the clay lump measured along the direction of trenching	m
c	Volume concentration of particles	-
C_f	Wall shear stress stress coefficient	-
c_f	Friction coefficient	-
d	Cavity depth (Nobel, 2013)	m
d	Jet diameter	m
D_n	Nozzle diameter	m
D_p	Particle diameter	mm
E	Geometric shape factor	-
e	Void ratio	-
f	Emperical constant for critical shear strength (Kamphuis and Hall, 1983)	-
F_g	Drag force	N
g	Gravitational acceleration	$\mathrm{m\,s^{-2}}$
H	Height at which the particle enters the trench	m
h	Cavity depth	m
k	Hydraulic conductivity	$\mathrm{m\,s^{-1}}$
k_1, k_2	Empirical entrainment coefficients	-
L	Distance from the jetting sword where the particle settles	m
l	Arc length of the jet soil interface trajectory	m
LL	Liquid limit	%
n	Exponential function as a function of Re_p	-
n	Porosity	-

N_c	Bearing capacity factor for cohesive soils	-
N_{sp}	Nozzle spacing of the inward nozzles	m
p_j	Jet pressure at the exit of the nozzle	Pa
p_w	Pore water pressure	Pa
p_{stag}	Stagnation pressure	Pa
PL	Plastic limit	%
q	Bearing capacity	Pa
q	Specific Discharge	$\mathrm{m\,s^{-1}}$
Q_0	Flow rate at the exit of the nozzle	$\mathrm{m^3\,s^{-1}}$
Q_s	Flow rate at nozzle distance s	$\mathrm{m^3\,s^{-1}}$
r	Nozzle radius	m
r	Radial distance from center line	m
r	Radius of the particle	m
Re_p	Particle Reynolds number	-
S	Degree of saturation	-
s	Distance from the nozzle at the center line	m
s_u	Undrained shear strength	Pa
s_{dr}	Distance from the nozzle where the fully developed region starts	m
u	Horizontal flow velocity in the trench	$\mathrm{m\,s^{-1}}$
u	Horizontal velocity of the particle	$\mathrm{m\,s^{-1}}$
u_0	Uniform jet velocity at the nozzle	$\mathrm{m\,s^{-1}}$
$u_j(s,r)$	Jet velocity in the developed flow region	$\mathrm{m\,s^{-1}}$
u_s	Jet velocity at the interface of the jet and the surface	$\mathrm{m\,s^{-1}}$
$u_\star$	Friction velocity	$\mathrm{m\,s^{-1}}$
$u_{bl,max}$	Jet velocity at the edge of the boundary layer	$\mathrm{m\,s^{-1}}$
V	Volume of the soil	$\mathrm{m^3}$
v_c	Dislodgment velocity	$\mathrm{m\,s^{-1}}$
v_j	Jet velocity	$\mathrm{m\,s^{-1}}$
V_p	Volume of pores	$\mathrm{m^3}$
v_p	Velocity of the particle	$\mathrm{m\,s^{-1}}$
V_s	Volume of solid particles	$\mathrm{m^3}$
V_t	Total volume	$\mathrm{m^3}$
v_t	Forward velocity	$\mathrm{m\,s^{-1}}$
V_w	Volume of water within the pores	$\mathrm{m^3}$

$V_{req,10mm}$	Flow velocity required to transport lumps of 10 mm	$m s^{-1}$
$V_{req,200mm}$	Flow velocity required to transport lumps of 200 mm	$m s^{-1}$
W	Weight of the soil	kg
w	Cavity width	m
w	Vertical velocity of the particle	$m s^{-1}$
w	Water content	-
w_0	Settling velocity	$m s^{-1}$
W_c	Width of the cavity	m
W_p	Weight of solid particles	kg
w_s	Effective settling velocity	$m s^{-1}$
W_w	Weight of water	kg
$w_{mud,max}$	Maximum settling velocity at $c = 0.0025$	$m s^{-1}$
$w_{mud,min}$	Minimum settling velocity at $c = 0.00001$	$m s^{-1}$
w_{mud}	Concentration-dependent mud settling velocity	$m s^{-1}$
x	Horizontal component of the jet soil interface trajectory (Zhang, Ge, et al., 2016)	m
x	Penetration depth (Atmatzidis and Ferrin, 1983)	m
x_{max}	Limiting penetration for a stationary jet after infinite time	m
y	Vertical component of the jet soil interface trajectory (Zhang, Ge, et al., 2016)	m

1

Introduction

1.1. Background and Motivation

As climate change and its consequences become more apparent, governments around the world have set goals for 2030 and 2050 to reduce emissions and limit global warming. The need for an energy transition is growing, and renewable energy is becoming increasingly important. Offshore wind energy is a form of renewable energy that has seen significant growth in recent years.

Offshore wind energy projects are complex and involve numerous components, a key element are the subsea cables that transport electricity from the wind turbine generators (WTGs) to substations and ultimately to the shore. Cable laying vessels are used to install these cables, which include inter-array cables connecting the WTGs to each other and an offshore substation, and export cables that transport the energy generated by the WTGs to the onshore transformer station.

As shown in Figure 1.1, the inter-array cables connect the WTGs to an offshore substation, where the energy generated by the WTGs is collected before being transported to shore. The export cables are transport the energy to shore, where it is transformed in the transformer station and distributed through the electricity grid.

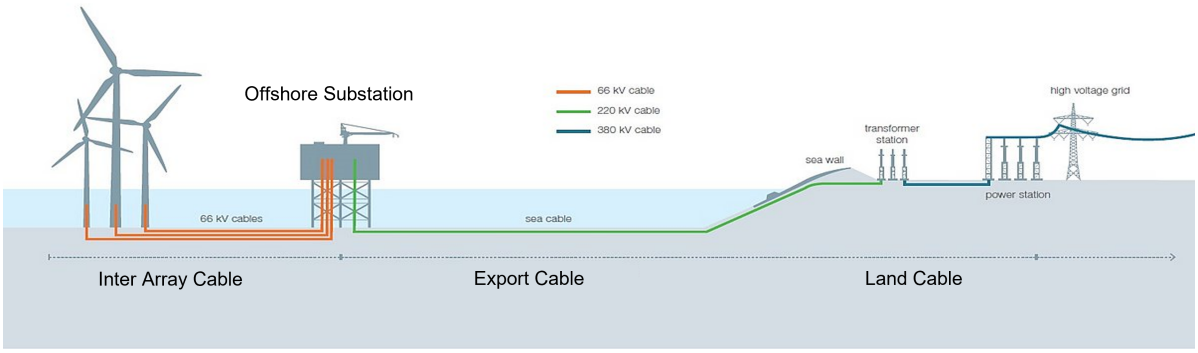

Figure 1.1: Inter array & export cables (DEME, 2021)

Subsea cables are laid on the seabed using cable laying vessels. In order to protect these cables against external threats such as anchors, fishing gear, and dredging activities, various protection methods can be implemented. The most commonly used and preferred method is burying the cable, as it provides the best protection and causes the least disturbance to the environment. Other methods are to cover the cable with rocks, concrete mattresses or rock bags or by using a cable protection system. Burying the cable is typically preferred because its protection capabilities and relatively low environmental impact. There are several methods to bury offshore cables, including:

1. **Jet Trenching:** In this method, high-pressure water jets are used to create a trench in the seabed for the cable to be laid in. The cable is then lowered into the trench, which is backfilled with soil to provide protection.
2. **Mechanical Cutting:** This method involves using mechanical equipment (chain cutter) to cut a trench in the seabed for the cable to be laid in. The cable is then placed in the trench and covered with soil.
3. **Ploughing:** A plough is used to cut a narrow trench in the seabed for the cable to be laid in. The plough can be towed behind a vessel or attached to a remotely operated vehicle (ROV). Once the cable is in place, the trench is backfilled with soil.
4. **Dredging:** This method involves using dredging equipment to excavate a trench in the seabed for the cable to be laid in. The cable is then placed in the trench and covered with soil.

The best choice for burying a cable depends on several factors, including the specific energy, disturbance to the environment, and economics. In general, jet trenching is the preferred method for burying cables in sandy or clay seabeds, as it causes the least disturbance to the environment. Jet trenching requires less power than other methods, which makes it more energy-efficient and less expensive.

For rocky seabeds, mechanical cutting may be necessary to create a trench. However, mechanical cutting can cause more disturbance to the environment than other methods. Ploughing can also be used in hard seabeds, but it requires a high level of power and may not be the most energy-efficient option.

Dredging is the most environmentally damaging method of burying cables, and it is typically used only when other methods are not feasible. It also requires a large amount of power and creates a significant amount of disturbance to the seabed and marine life (Srinil, 2016).

When making a choice between these different methods, it is important to consider the specific energy, the disturbance to the environment, and the economics of each method. The decision should be based on a comprehensive analysis of these factors and the project's specific needs. Which method is most suitable for different types of soils can generally be determined by the strength of the soil as depicted in figure 1.2.

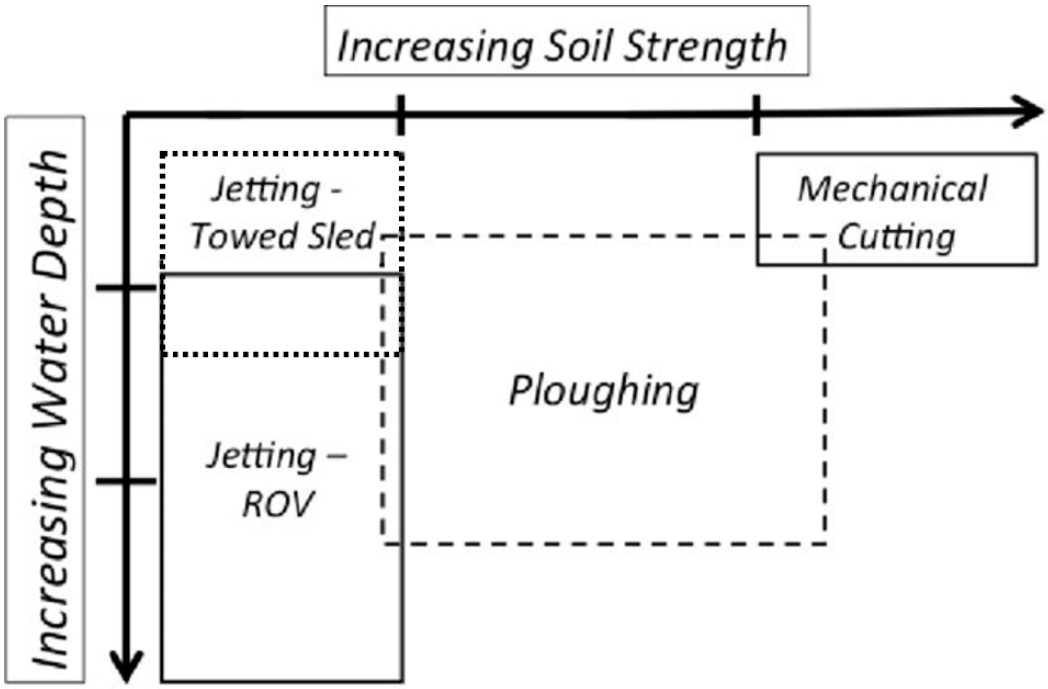

Figure 1.2: Different methods of cable burial (Brunning and Machin, 2014)

DEME Offshore NL, a Dutch company specialized in foundation/turbine transport & installation, rock placement, offshore cable installation, and operation and maintenance activities, aims to develop a model to predict the performance of a jet trenching tool operating in clay. By doing so, they can optimize the trenching process and reduce costs associated with cable installation. While jet trenching is a preferred method for burying subsea cables, its performance in cohesive materials such as clay is not well understood. Developing a model that accurately predicts the performance of the jet trenching process in clay can help DEME to determine the optimal nozzle configuration, flow rate, pressure required and forward velocity to achieve a specific trench depth.

1.2. Problem Statement and Research Questions

Jet trenching is a well-established method for burying subsea cables in non-cohesive soils like sand. However, when it comes to cohesive soils like clay, jet trenching is still a relatively new technique. The success of jet trenching in cohesive soils depends on soil parameters such as undrained shear strength, plasticity index, soil density, and grain size distribution, as well as jetting settings like jet pressure, nozzle diameter, and forward velocity. The interaction of these parameters is essential in determining the feasibility of jet trenching in cohesive soils and predicting the performance of the jet trenching tool.

It has been found difficult to accurately predict and model the jet trenching process in cohesive soils, despite DEME having experience in the field. This is due to the complexity of the soil structure in cohesive soils, which behaves differently from sandy soils. Currently, DEME uses a model which is solely based on the penetration depth of the water jet, which may not accurately predict other important processes, such as the formation of clay blocks and sedimentation. Therefore, a thorough understanding of the processes occurring during jet trenching in cohesive soils is necessary to develop an accurate model for predicting the jetting process.

The overall problem of the study is to better understand the jet trenching principle in cohesive soils, which is crucial for the installation of subsea cables. Specifically, the focus will be on investigating the flow behind the jet trenching machine using CFD to accurately predict the sedimentation of soil particles and improve the existing models for jet penetration used by DEME.

The research question that will guide the study is:

> *How can the performance of a jet trenching tool be modelled in cohesive soils and what accuracy can be achieved?*

Sub-questions that will be explored to answer the main research question include:

1. What processes take place during jet trenching with water jets in cohesive soils?
2. How can these processes be predicted in a quantitative model?
3. How can CFD be used to improve the existing models for jet trenching in cohesive soils used by DEME?

Answering these sub-questions will contribute to a better understanding of the jet trenching principle in cohesive soils and provide insight into improving the existing models for jet penetration used by DEME. The study will also provide recommendations for future research and development in this area.

1.3. Scope and Limitations

The scope of this thesis will be to investigate the flow behind the jet trenching machine in cohesive soils and develop an accurate model using CFD to predict the sedimentation of soil particles and improve the existing models for jet penetration used by DEME. The study will focus on understanding the key factors that influence the flow behind the jet trenching machine in cohesive soils, exploring how CFD can be used to accurately model the flow behavior behind the jet trenching machine, and analyzing how different jet settings and soil properties affect the sedimentation of soil particles during the jet trenching process. The limitations of the existing models for jet penetration used by DEME will also be assessed, and recommendations for future research and development in this area will be provided.

1.4. Thesis Outline

An overview of each chapter in the thesis:

Chapter 1: Introduction
This chapter provides an overview of the research topic, including the background and motivation behind the study. It also presents the research problem and questions, and outlines the scope and limitations of the research. Finally, this chapter provides an overview of the thesis outline.

Chapter 2: Theoretical Background
This chapter provides an overview of the jet trenching technique and the general soil conditions of cohesive soils. It explores key soil parameters and jetting settings that affect the feasibility of jet trenching in cohesive soils, such as undrained shear strength, plasticity index, jet pressure, and nozzle diameter.

Chapter 3: Cutting Depth of a Single Jet in Cohesive Soils
This chapter focuses on the cutting depth of a single jet in cohesive soils, including the flow field of a free jet, cavitating jets, stagnation pressure, and penetration depth. It also discusses previous research on moving vertical jets in cohesive soils, failure mechanisms of clay exposed to a moving jet, failure modes of clay exposed to a moving jet, and moving penetrating jet modelling.

Chapter 4: Sedimentation of Cohesive Material
This chapter covers the sedimentation of cohesive material, including the settling velocity of different-sized particles and the sediment transport of clay particles. It also discusses the influence of turbulence and clay block formation in between the nozzles.

Chapter 5: Conclusions of Literature Review
This chapter summarizes the key findings of the literature review, including the most important processes in jet trenching of cohesive soils: jet cutting depth, block formation in between the nozzles, and sedimentation.

Chapter 6: Methodology
This chapter focuses on the methodology employed in this study to investigate the feasibility of jet trenching in cohesive soils. It outlines the CFD approach utilized to simulate the behavior of the jetting process in clay seabeds. Additionally, it details the Verlet integration method employed for particle tracking and the sensitivity analysis conducted to assess the impact of various parameters on trenching outcomes.

Chapter 7: Simulation Results and Analysis
In this chapter, the results obtained from the simulations and analyses are presented and discussed comprehensively. It includes the findings regarding the behavior of particles and fluid flow within the trenching environment, as well as the validation of the model against experimental data where applicable. The analysis delves into the implications of the results on the feasibility and efficiency of jet trenching in cohesive soils, considering factors such as particle size, trench dimensions, and flow rates.

Chapter 8: Conclusions & Recommendations
The concluding chapter synthesizes the key findings of the study and offers insights into the implications for trenching operations in cohesive soils. It reflects on the limitations of the current modelling approach and provides recommendations for future research directions to address these challenges. Additionally, it underscores the importance of empirical validation and field testing to corroborate the insights gleaned from computational modelling, ensuring the relevance and applicability of the findings in real-world scenarios.

Abstract Literature Review

This literature review provides an overview of various methods and models proposed for analyzing the processes involved in jet trenching operations. The focus of the study is on the penetration depth of a single jet in cohesive soils, the settling velocities and sedimentation of soil particles and clay block formation during jet trenching in cohesive soils. Experimental testing, mathematical models, and empirical equations have been explored to predict the cutting depth of the jet and the behavior of soil particles.

The review highlights the importance of considering factors such as the forward velocity of the jet, soil properties, and jet settings in accurately predicting cutting depth. Experimental data has been studied to determine optimal nozzle design, jet pressure, and forward velocity required for specific penetration depths. Mathematical models and empirical equations have also been adressed to predict the cutting depth based on these factors.

In addition, the study addresses the settling velocities and sedimentation transport of soil particles, which depend on the flow pattern experienced by the particles. The complex flow behind a jet trenching machine requires further investigation through experiments or CFD. A new CFD model is proposed in this study to predict the flow behind the trenching machine. The model aims to accurately account for sedimentation of soil particles and its impact on the depth achieved during the trenching process.

Furthermore, the occurrence of clay blocks during jet trenching is observed, but the precise process behind their formation remains poorly understood. Existing models for predicting clay block size have limitations and do not account for factors such as block breakage due to collisions with other jets or blocks stacking up on each other. Therefore, assumptions regarding block size will be made in this study to account for clay block formation.

Overall, this literature review lays the foundation for a thesis that aims to develop an enhanced model for jet trenching operations. The focus will be on investigating the flow pattern and sedimentation of soil particles behind the trenching machine using CFD. The study intends to improve the existing models used by integrating the flow pattern with the jet trenching model, considering sedimentation effects, and addressing the assumptions made regarding clay block size.

Literature Review

Jet trenching is a widely used technique for burying subsea cables and pipelines. However, trenching in cohesive soils presents challenges due to their complex properties, which can make the trenching process difficult. To model and optimize the jet trenching process in cohesive soils, it is essential to understand the three main processes involved:

- Penetration depth & cavity shape of individual jets (figure 1.3a)
- Clay block formation in between the nozzles (figure 1.3b)
- Sedimentation of the clay particles in the trench (figure 1.3c)

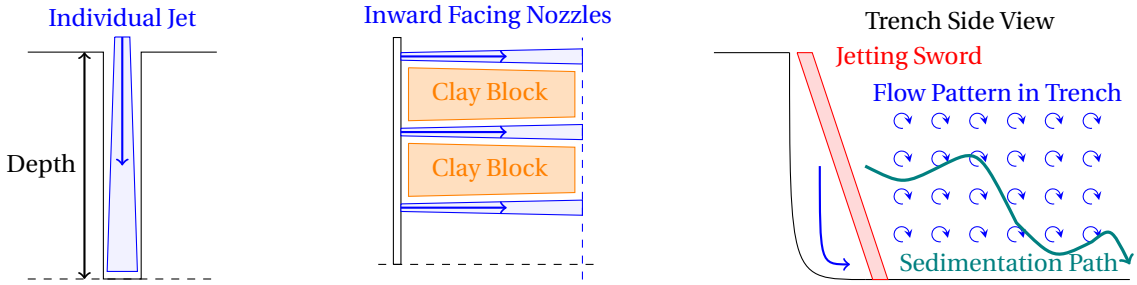

(a) Penetration depth (b) Clay block formation (c) Sedimentation

Figure 1.3: Processes during jet trenching

The first process, penetration depth of single jets, is determined by various factors such as soil conditions, the nozzle diameter, jet pressure, and forward velocity of the jet trenching machine. The ability of the inward nozzles to reach each other and clear the area in front of the jetting sword is essential for the trenching process to be successful. The review will examine existing research on the effect of these factors on the cutting depth of the jet and the optimization of nozzle configuration.

The second process, clay block formation in between the nozzles, can obstruct the lowering of the cable. The literature study will review existing research on the formation of these blocks and how/if they can be avoided or removed during the jet trenching process.

The third process, sedimentation, is the behavior of clay particles (block formations) after they are impacted by the jet. The size and behavior of the particles depend on the soil properties and jetting settings as well as the flow patern behind the jet trenching machine. The review will examine existing research on the sedimentation process and the impact of particle behavior on the trenching process.

The purpose of this literature review is to provide a comprehensive understanding of the processes involved in jet trenching of cohesive soils. It will begin with a theoretical background to facilitate understanding of the topic, followed by a focus on the three main processes: jet cutting depth, block formation between nozzles, and sedimentation. The review aims to give an overview of the current theories and techniques in jet trenching technology, and identify areas where further research is needed to improve the models for the jet trenching process in cohesive soils.

2

Theoretical Background

2.1. Overview of Jet Trenching Technique

Jet trenching is a method used for burying cables and pipelines, which involves creating a trench in the seabed by using high-pressure water jets. The technique is commonly used in offshore projects, such as offshore wind farms, where cables must be buried in the seabed to protect them from fishing gear (for export cables to shore), underwater currents and other environmental factors. The process can be carried out using a remotely operated vehicle (ROV) equipped with jetting tools.

A ROV is a machine which can be used for trenching the seabed for offshore wind farm inter-array and export cables. The machine can be equipped with jetting swords or mechanical cutting tools depending on the method of excavation. Figure 2.1a shows the CBT 1100 trenching ROV used by DEME. The ROV is deployed from a cable laying vessel after the cable has been laid on the seabed. The umbilical cable is used to control the ROV from the vessel once it is deployed. A specification sheet of the
CBT 1100 is provided in appendix A.

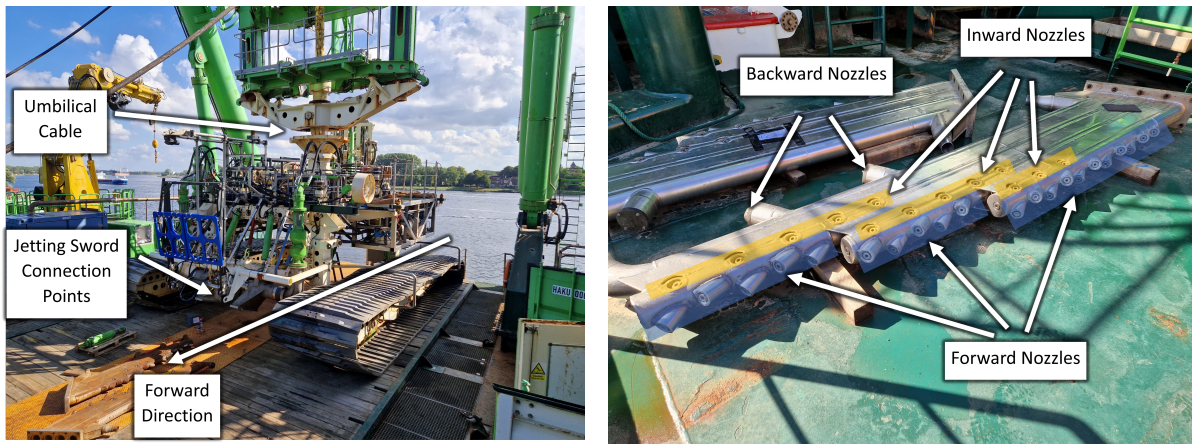

(a) Jet Trenching Machine CBT 1100

(b) Jet Trenching Sword

Figure 2.1: Jet trenching equipment

For jet trenching in sand and clay, the ROV is equipped with jetting swords (figure 2.1b) that create a trench in the seabed for the cable to sink into.The jetting swords are equipped with multiple nozzles that generate water jets. A schematic illustration of a typical jetting sword is given in figure 2.2. The front view on the top of figure 2.2 shows the forward facing nozzles which clear the area for the jetting swords to move forward. On the bottom, the side view shows the inward facing nozzles which create the actual trench between the jetting swords.

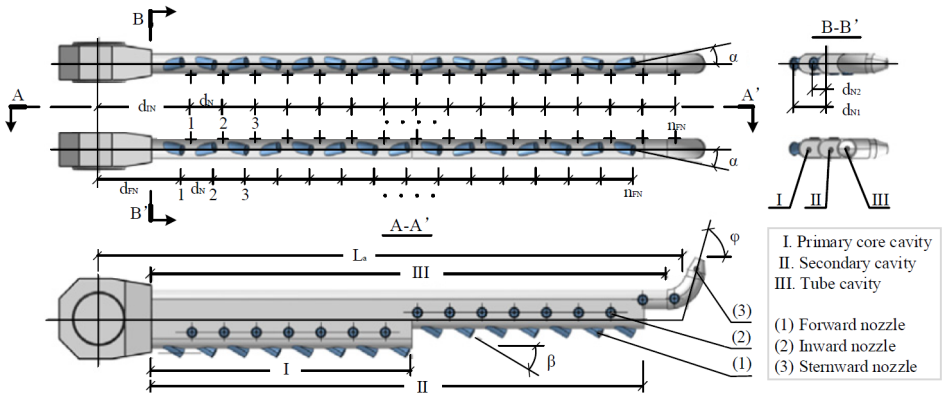

Figure 2.2: Schematic illustration of a jetting sword (Njock et al., 2020)

As the ROV moves over a sandbed, the jetting swords are gradually lowered into the soil. The high-pressure water jets create a fluidized zone between the jetting swords, which allows the cable to sink into the trench. The process of jet trenching in sand is depicted in figure 2.3 (a) and (b).

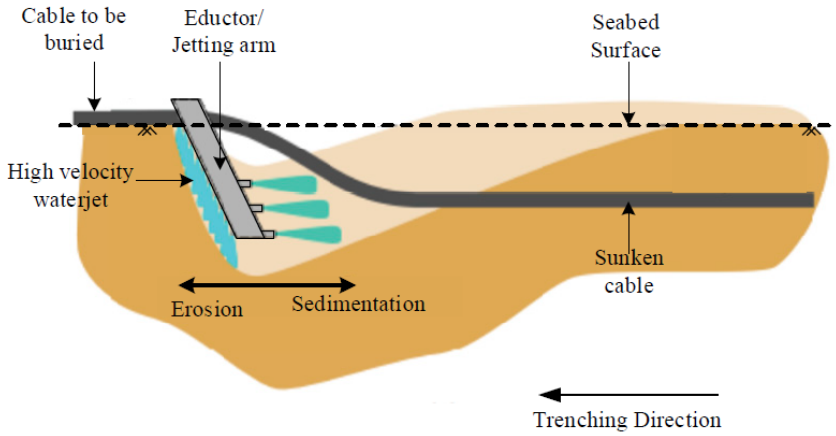

(a) Jet trenching process in sand

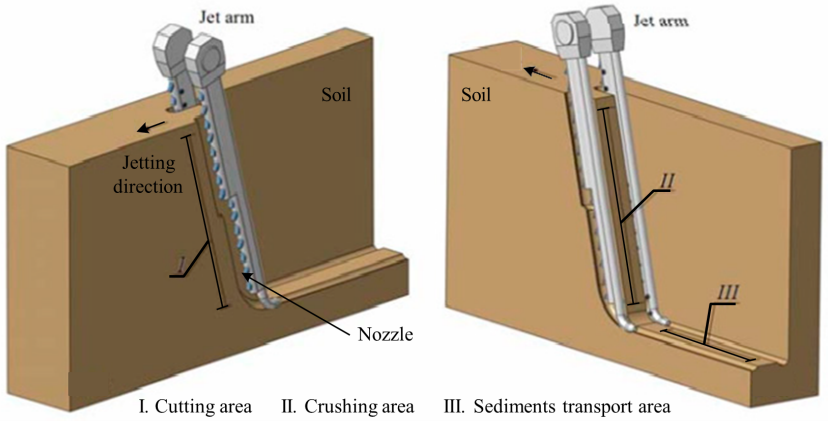

(b) Jet trenching schematization

Figure 2.3: Jet trenching principle (Njock et al., 2020)

As the soil particles are fluidized, they are transported backwards by the water flow, creating a trench behind the jetting sword. The size and shape of the trench depend on the diameter of the jetting sword and the water pressure and flow rate. The ability of the cable to sink into the trench depends on the soil properties, water

pressure, flow rate, and the weight and flexibility of the cable. The trench must be deep enough to provide adequate protection and support for the cable or pipeline (Njock et al., 2020).

Ensuring the protection of the cable, it is necessary to cover it with soil after it is lowered into the trench. The trench profile, depicted in Figure 2.2, shows the trench depth, depth of lowering (DOL) and depth of cover (DOC). The DOC is creating by a one-pass burial. These depths are usually prescribed by either the client or local government regulations, making it crucial for contractors to meet the requirements while carrying out the project.

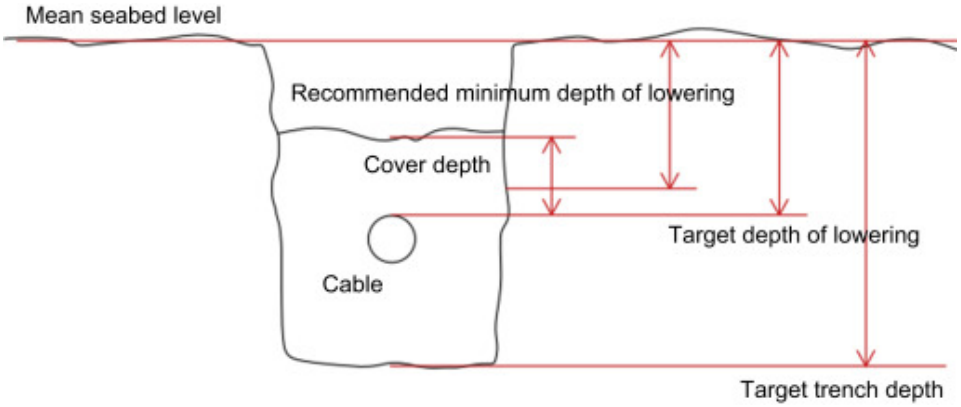

Figure 2.4: Trench profile (Srinil, 2016)

Jet trenching is an effective and efficient method for burying cables and pipelines in relatively loose and non-cohesive soils. The process is less disruptive for the environment than traditional dredging or mechanical excavation methods. This process is well-known for trenching in sand, where the soil is fluidized by the water jets, creating a trench that allows the cable to sink in. However, trenching in cohesive soils, such as clay, is a different process due to the difference in soil structure.

Clay soils are hard to penetrate by water pressure due to their high undrained shear strength and low hydraulic conductivity. The cohesion causes a strong attraction between soil particles resists water infiltration, while the small pore spaces restrict water flow through the soil. These properties make cohesive soils less permeable and more resistant to water penetration compared to non-cohesive soils.This makes jet trenching in cohesive material more challenging than in non-cohesive material such as sand. (Zhou and Li, 2000).

2.2. Soil Characteristics of Cohesive Soils

The general soil conditions of cohesive soils play a crucial role in understanding the behaviour of a penetrating jets during jet trenching operations. This section covers the important aspects of soil properties, soil characteristics, plasticity, and undrained shear strength that are relevant for jet trenching. These parameters affect the behaviour of the soil and the response of the soil to the jet, which in turn, determines the efficiency and effectiveness of the jet trenching process. Understanding the general soil conditions of cohesive soils is therefore essential for predicting and optimizing the jet trenching process.

2.2.1. Soil Particle Size

Different types of soils can generally be divided by their grain size. Table 2.1 shows the classification of soil types according to the Dutch classification system (NEN). As can be seen in the table, clays and silts have small grain sizes.

Soil Type	minimum [mm]	maximum [mm]
Clay	-	0.002
Silt	0.002	0.063
Sand	0.063	2
Gravel	2	63

Table 2.1: Grain size diameter D_p (NEN), (Verruijt, 2001)

Cohesive soils consist of clay minerals. These minerals are responsible for the cohesive behaviour found in these soils. Clay minerals are characterized by: a small particle size, a flat platy shape, a negative electrical charge and a very large specific surface [1]. The surface area interacts with water which gives clays the ability to attract and bind to water. Some properties of the most common clay minerals are given in table 2.2 (Mitchell and Soga, 2005).

		Kaolinite	Montomorillonite	Illite
Particle dimensions	[µm]	$0.1-4\times0.05-2$	$>0.001\times<10$	$0.003-0.1\times<10$
Specific surface (A_s)	[$m^2\,g^{-1}$]	15 ± 5	770 ± 70	80 ± 20
Specific density (ρ_s)	[$kg\,m^{-3}$]	2670 ± 10	2530 ± 170	2800 ± 200
[2] Liquid limit (LL)	[%]	$30-110$	$100-900$	$60-120$
[3] Plastic limit (PL)	[%]	$25-40$	$50-11$	$35-60$

Table 2.2: Main properties of most common clays (Mitchell and Soga, 2005)

Another important characteristic for soils is the grain size distribution. The grain size distribution shows the percentage of particles in a soil sample which are smaller than a certain diameter. Figure 2.5 shows typical grain size distributions for sand and a silty clay. A steeper curve indicate the soil is rather uniform in terms of particle diameter whereas a shallow shape indicated a more grades soil composition. Cohesive materials are often composed of clay, silt and sand. The clay particles instigate the cohesive behaviour. A soil is considered cohesive if more than 50% by weight of the particles are fine (i.e. clay and silt $D_p < 0.63$[mm]) (Nobel, 2013).

[1] The specific surface area is the total area of solid particles of a material per unit of mass [$\frac{m^2}{g}$]

[2] See subsection 2.2.3

[3] see subsection 2.2.3

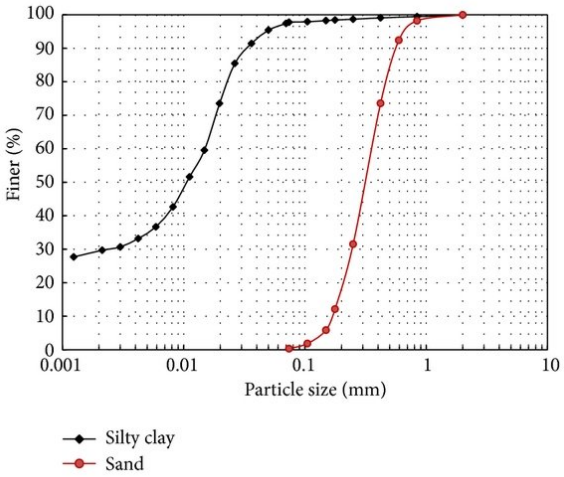

Figure 2.5: Grain size distribution (Lodhi et al., 2017)

Due to the small size of clay particles, clay soils has a low permeability. This means that they have a limited ability to allow fluids, such as water, to pass through. Additionally, the high concentration of particles within clay soils results in a low porosity, which refers to the amount of empty space or voids within the soil. Consequently, the combination of low permeability and low porosity leads to a very low hydraulic conductivity within clay and silt soils. Typical values of the hydraulic conductivity for different types of soils are given in table 2.3.

Type of soil	Hydraulic Conductivity k [m s^{-1}]
Gravel	$10^{-3} - 10^{-6}$
Sand	$10^{-6} - 10^{-3}$
Silt	$10^{-8} - 10^{-6}$
Clay	$10^{-10} - 10^{-8}$

Table 2.3: Typical values for hydraulic conductivity (Verruijt, 2001)

2.2.2. Definition of Soil Parameters

Soils usually consist of a mixture of particles, water and air. The distribution of these components is important to describe the soil parameters which are needed to predict the behaviour of the soil. An important parameter to describe this distribution is the porosity n (equation 2.1), which is the ratio between the volume of pores and the total volume of the soil (Verruijt, 2001).

$$n = \frac{V_p}{V_t} \tag{2.1}$$

where n : porosity [-]
V_p : Volume of pores [m^3]
V_t : Total volume [m^3]

Another way to describe the amount of pores within a soil is by using the void ratio e (equation 2.2), which is defined as the ratio between the volume of the pores and the volume of the solid particles within the soil. The void ratio and the porosity can easily be related as shown in equation 2.2, which quantity is used in different countries is based on preference.

$$e = \frac{V_p}{V_s} = \frac{n}{1-n} \tag{2.2}$$

where e : Void ratio [-]
V_s : Volume of solid particles [m^3]

The volume of pores can be filled with water or air. Therefore, soil has a degree of saturation S (equation 2.3), which is defined as the ratio between the volume of water within the pores and the the total volume of pores between the solid particles. For this study, the soils will be considered fully saturated (S=1).

$$S = \frac{V_p}{V_w} \tag{2.3}$$

where S : Degree of saturation [-]
V_w : Volume of water within the pores [m^3]

To perform calculation regarding soil mechanics, more often than not the volumetric weight is required. If the soil is fully saturated and the densities of the soil particles and of water are known, the volumetric weight can be calculated using equation 2.4. The volumetric weight is defined as the weight of the soil mixture per unit volume.

$$\gamma = \frac{W}{V} = n\rho_w g + (1-n)\rho_p \tag{2.4}$$

where γ : Volumetric weight [$kg\,m^{-3}$]
W : Weight of the soil [kg]
V : Volume of the soil [m^3]
ρ_w : Density of water [$kg\,m^{-3}$]
ρ_p : Density of solid particles [$kg\,m^{-3}$]

Another useful soil parameter, especially for clay, is the water content (equation 2.5). The water content w is defined as ratio of the weight of the water and the solid particles.

$$w = \frac{W_w}{W_p} (= e\frac{\rho_w}{\rho_p}, \, for \, S = 1) \tag{2.5}$$

where w : Water content [-]
W_w : Weight of water [kg]
W_p : Weight of solid particles [kg]

Permeability is the ability of water to flow through the soil. The ability of to flow through the soil can also be described by the hydraulic conductivity. The hydraulic conductivity k. Similarly to the permeability, the hydraulic conductivity represents the ability of a fluid to flow trough a soil. The flow of a fluid through a porous medium can be determined using Darcy's law (equation 2.6). The flow depends on the hydraulic conductivity and the hydraulic gradient, a dimensionless quantity which indicates the slope of the phreatic surface.

$$q = -k\frac{dh}{ds} \tag{2.6}$$

where q : specific discharge [$m\,s^{-1}$]
k : Hydraulic Conductivity [$m\,s^{-1}$]
$\frac{dh}{ds}$: Hydraulic gradient [-]

2.2.3. Plasticity

In geotechnical engineering, the term plasticity refers to the ability of a soil to undergo permanent deformation without cracking or breaking. In cohesive soils, such as clays and silts, the plasticity is related to the behavior of the clay mineral particles in the soil. When water is added to a cohesive soil, the clay particles can absorb the water and become more hydrated, resulting in an increase in the soil's plasticity. Conversely, if the water content of the soil is reduced, the clay particles can become more compacted, resulting in a decrease in plasticity. The plasticity of a cohesive soil is an important property that affects its strength, compressibility, and permeability (Waltham, 1994).

Plasticity of a material is very much dependent in the water contented (equation 2.5). The plastic state of materials can be divided into 3 states: liquid, plastic and solid. They are separated by the 2 *Atterberg limits*. The boundary between the liquid and plastic state is called the liquid limit LL, it represents the lowest water content [%] at which the soil is still in liquid state. The plastic limit PL represents the water content at which the material transitions from plastic to solid state. The difference between PL and LL is called the plasticity index:

$$PI = LL - PL \tag{2.7}$$

The plasticity index represents the compressibility and the volume change when the material is loaded or unloaded.

2.2.4. Undrained Shear Strength

The behaviour of cohesive material during jet trenching can be assumed to be unconsolidated and undrained. This assumption can be made because the permeability of cohesive soils is very low and the loading during jet trenching is relatively rapid. Undrained behavior refers to the response of a soil or sediment when it is loaded without allowing significant drainage of pore water. In other words, the excess pore water pressure generated during loading is not dissipated. This behavior is typically observed in saturated cohesive soils, such as clays, where the permeability is very low and water cannot flow out quickly.

In undrained conditions, the stress-strain behavior of the soil can be determined using only the total stresses (i.e., the applied stresses without considering the pore water pressure). This is because the undrained response of the soil is primarily controlled by the effective stress σ', which is the difference between the total stress σ and the pore water pressure p_w (Terzaghi et al., 1943). The excess pore water pressure that develops during loading affects only the pore pressure and does not contribute directly to the effective stress. Therefore, the stress-strain relationship can be established by considering only the total stresses. This simplification is possible because the undrained behavior focuses on the immediate response of the soil without allowing time for pore water pressure dissipation.

Undrained shear strength s_u is a property of soils that measures their resistance to shear deformation when they are unable to dissipate excess pore water pressure. It is a measure of the soil's cohesive strength and is particularly relevant for saturated or partially saturated soils. The undrained shear strength represents the maximum shear stress that a soil can sustain without undergoing excessive deformation or failure. It is a measure of the soil's ability to resist shear forces in the absence of drainage. This cohesive strength is primarily associated with clayey or silty soils. The undrained shear strength can be defined by the Mohr-Circle as:

$$s_u = \frac{1}{2}(\sigma_1 - \sigma_3) \tag{2.8}$$

where s_u : Undrained shear strength [Pa]
σ_1 : Major principle stress [Pa]
σ_3 : Minor principle stress [Pa]

The undrained shear strength of soils is typically determined through several laboratory tests or in-situ measurements. These include the triaxial test, direct shear test, vane shear test in the laboratory, or the use of a penetrometer or a hand-torvane in-situ. Each method has its advantages and limitations, and the resulting undrained shear strength values can vary.

Nobel (2013) found that different methods for determining undrained shear strength can yield values that differ by up to 24% (table 2.4). This is a significant difference, highlighting the variability in measurement results. To create an accurate and reliable model, it is important to use a consistent and well-defined method for determining undrained shear strength.

However, in practice, organizations like DEME (a company specialized in dredging, marine engineering, and environmental remediation) often receive undrained shear strength values from a specific method. Conducting additional survey work to determine undrained shear strength more precisely can be economically impractical. As a result, they work with the values provided, even though they may not fully capture the true range of undrained shear strength that could be obtained from other methods.

		20 kPa sample	45 kPa sample	70 kPa sample
Penetrometer	s_u [kPa]	22	45	82
Hand-torvan	s_u [kPa]	27	48	85
Vane shear test	s_u [kPa]	18	35	86
Triaxial test	s_u [kPa]	18.3	32.6	71.2
Variation	[%]	24	19	10

Table 2.4: Variation measured undrained shear strength for different tests (data from Nobel (2013))

3

Cutting Depth of a Single Jet in Cohesive Soils

The cutting depth of a single jet is a critical process for jet trenching operations in cohesive soils, which is used to install subsea cables and pipelines in the offshore industry. This process depends on various soil condition parameters and jet settings as well as the horizontal forward velocity of the jet. Understanding the factors that influence the cutting depth of a single jet in cohesive soils is crucial for modelling the jet trenching operation.

To predict the cutting depth of the single jet in cohesive soils, various approaches have been proposed, including experimental testing, mathematical models, and empirical equations. These approaches consider soil properties and jet settings to predict the cutting depth of the jet accurately. Experimental testing involved conducting laboratory tests to determine the optimal nozzle design, jet pressure, and forward velocity to achieve a specific penetration depth.

This chapter will examine these factors and explore the different approaches to predict the cutting depth of a single jet in cohesive soils. The different approaches will be evaluated and compared based on their experimental parameters, with the goal of selecting the most suitable method for jet trenching in clay.

3.1. Principle of a Stationary Jet in Cohesive Soils

Before one can understand the principle of jet trenching in cohesive soil, it is essential to comprehend the process of a single jet in cohesive soil. This process has been a subject of extensive research in various industries, including the dredging industry, mining, and grouting techniques. Understanding the fundamentals of how a jet interacts with cohesive soil can provide insights into the mechanics of jet trenching and its effectiveness in excavating the seabed.

3.1.1. Flow Field of a Free Jet

To be able to understand and predict the cavities created while jetting, the flow field of a single jet in free water will be considered first. The flow field of a free jet with a uniform velocity u_0 at the exit of the nozzle is shown in figure 3.1. A shear/mixing layer develops due to the difference in flow velocity and viscosity between the ambient water and the jet. This layer is the interface where transfer of mass and momentum (ambient water entrainment) take place. Due to water entrainment, the potential core (see figure 3.1) in which unhindered velocity is possible becomes smaller with increasing distance from the nozzle s (Nobel, 2013).

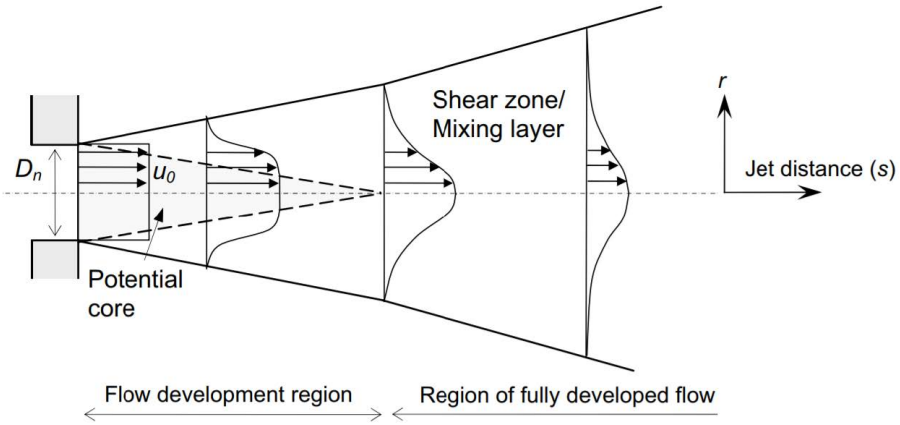

Figure 3.1: Flow field of a jet in free water (Nobel, 2013)

In the fully developed flow region, the flow velocity is Gaussian. From the Gaussian distribution equation 3.1 can be derived for the velocity of the jet depending on the distance from the nozzle and the radial distance from the center line. The maximum velocity is found at the interface distance between the flow development region and the fully devoloped region at $r = 0$ (Nobel, 2013).

$$u_j(s,r) = \sqrt{\frac{k_1}{2}}\, u_0 \frac{D_n}{s} e^{-k_2 \frac{r^2}{s^2}} \tag{3.1}$$

where

$u_j(s,r)$	:	Jet velocity in the developed flow region	[m s^{-1}]
k_1, k_2	:	Empirical entrainment coefficients	[-]
s	:	Distance from the nozzle at the center line	[m]
D_n	:	Nozzle diameter	[m]
u_0	:	Uniform jet velocity at the nozzle	[m s^{-1}]
r	:	Radial distance from center line	[m]

Based on experiments, Fischer (1979) found average values of $k_1 = 77$ and $k_2 = 87.3$. However, according to Albertson et al. (1950), the entrainment coefficients should be equal due to preservation of momentum (at $r = 0$). Therefore, in this study, the coefficient will be denoted as $k = k_1 = k_2 = 77$. The development region starts when the velocity at the center of the jet is equal to the jet velocity at the nozzle. Using $k = 77$, the distance from the nozzle where the fully developed region starts s_{dr} can be calculated (Nobel, 2013).[1]

[1] Similar to Nobel (2013), Machin et al. (2011) describe the flow development of a jet in free water according to this principle but have found $s_{dr} = 6D_n$ as the interface distance. Ho (2005) found a value of $s_{dr} = 6.25D_n$

$$u_j(s = s_r, r = 0) = u_0 \tag{3.2}$$

$$\sqrt{\frac{k}{2}} u_0 \frac{D_n}{s_{dr}} = u_0 \tag{3.3}$$

$$s_{dr} = \sqrt{\frac{k_1}{2}} D_n \approx 6.2 D_n \tag{3.4}$$

In the boundary layer, transfer and of mass and momentum take place due to entrainment of water. The amount of entrainment of water can be determined by the flow rate development with increasing distance from the nozzle s. Equation 3.1 has to be integrated to determine the flow rate in the developed flow region:

$$\int_{r=0}^{r=\infty} \frac{u_j}{u_0} dr = \int_{r=0}^{r=\infty} \sqrt{\frac{k}{2}} \frac{D_n}{s} e^{k\frac{r^2}{s^2}} dr \tag{3.5}$$

$$\frac{Q_s}{Q_0} = \sqrt{\frac{8}{k}} \frac{s}{D_n}, \text{for } s > 6.2 D_n \tag{3.6}$$

where Q_s : Flow rate at nozzle distance s [$m^3 s^{-1}$]
Q_0 : Flow rate at the exit of nozzle [$m^3 s^{-1}$]

Equation 3.6 shows that that the entrainment of water increases linearly with distance s from the nozzle. Differentiation to s yields the amount of entrainment per unit length:

$$\frac{dQ_s}{ds} = \sqrt{\frac{8}{k}} \frac{Q_0}{D_n}, \text{for } s > 6.2 D_n \tag{3.7}$$

3.1.2. Cavitating Jets

Cavitation in jets occurs when high-velocity fluid jets entrain ambient fluid into their mixing layer, causing a decrease in static pressure around the jet. When the static pressure drops below the vapor pressure of the fluid, vapor bubbles form, and these bubbles grow and collapse, creating strong pressure waves. Figure 3.2 shows cavitation of a jet in free water.

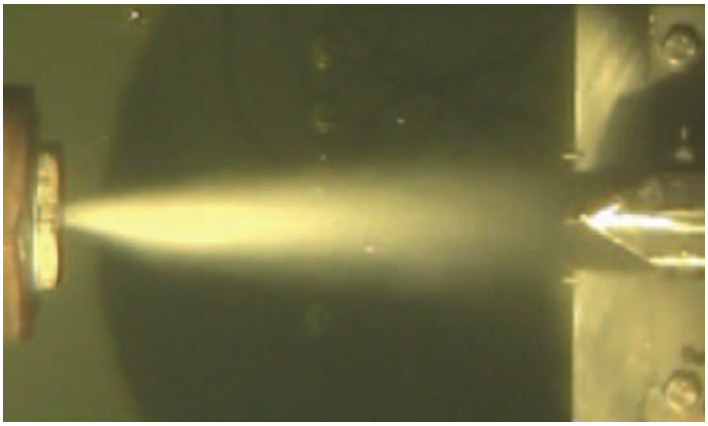

Figure 3.2: Cavitation of a free jet (Nobel, 2013)

In the case of cavitating jets penetrating cohesive soils, the cavitation can have an important influence on the penetration depth of the jet. When a non-cavitating jet impinges on soil, the axial velocity development of the jet is well-known and it decreases with distance from the jet (section 3.1.1). However, in the presence of cavitation, a cone of bubbles forms around the jet, decreasing the momentum exchange between the jet and the ambient water, as well as the associated entrainment. As a result, the decay of the jet velocity and stagnation pressure with jet distance decreases, which increases the penetration depth of the jet in cohesive soil.

It is important to note that the direct contribution of bubble implosions on the excavation capacity of the jet is probably negligible, since the amount of cavitation bubbles at the interface between the moving vertical jet and soil is assumed to be limited. Instead, the increase in penetration depth of the jet in cohesive soil due to cavitation is due to the reduction in the momentum exchange and entrainment associated with the formation of the cone of bubbles around the jet.

Based on the findings of Nobel (2013), cavitation only has a significant impact on the penetration depth of a jet at high pressures (>10 bar). Given the significant uncertainties and difficulties involved in predicting and modelling cavitation, this study will not take it into account. Furthermore, including cavitation in the study would only result in an increase in penetration depth, if it has any effect.

3.1.3. Stagnation Pressure

When a jet as described in subsection 3.1.1 hits a surface, like a seabed, it creates an impact (illustrated in figure 3.3). The impact on the surface exerts a pressure on the surface, this is called the stagnation pressure p_{stag}.

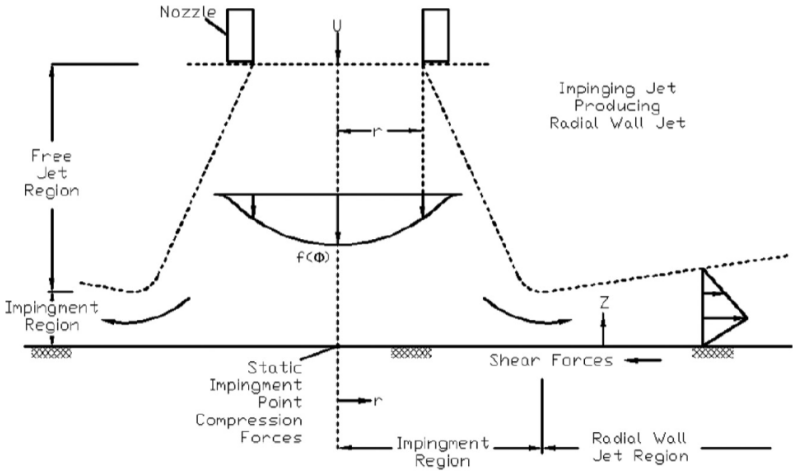

Figure 3.3: Jet impact and stagnation pressure (Blevins, 1984)

The stagnation pressure can be calculated using Bernoulli's principle:

$$p_{stag} = \frac{1}{2}\rho_w u_s^2 \tag{3.8}$$

where p_{stag} : Stagnation pressure [Pa]
u_s : Jet velocity at the interface of the jet and the surface [$\mathrm{m\,s^{-1}}$]

The same principle holds for the jet pressure at the exit of the nozzle:

$$p_j = \frac{1}{2}\rho_w u_0^2 \tag{3.9}$$

where p_j : Jet pressure at the exit of the nozzle [Pa]
u_0 : Jet velocity at the exit of the nozzle [$\mathrm{m\,s^{-1}}$]

Using equation 3.1, 3.8 and 3.9, a relation between stagnation pressure p_{stag} and jet pressure p_j can be formulated:

$$\frac{p_{stag}}{p_j} = \frac{\frac{1}{2}\rho_w u_s^2}{\frac{1}{2}\rho_w u_0^2} = \frac{u_s^2}{u_0^2} = (\sqrt{\frac{k}{2}}\frac{D_n}{s})^2 \approx 38.5(\frac{D_n}{s})^2 \tag{3.10}$$

From equation 3.10 it follows that the stagnation pressure decreases with the distance from the nozzle to the impact surface (denoted with s in equation 3.8). According to Machin et al. (2011), the stagnation pressure p_{stag} is roughly equal to the jet pressure p_j at small stand of distances (SOD). In this study, the process of trenching with jetting swords which are lowered into the soil is considered. Therefore, the SOD can be assumed to be small since the nozzles will always be relatively close to the soil.

$$p_{stag} = p_j = \frac{1}{2}\rho_w u_0^2 \tag{3.11}$$

3.1.4. Penetration Depth of a Stationary Jet

Jet erosion is widely used in many engineering applications, therefore it has been studied extensively. Much research on jetting in cohesive material is focused on prediction of the penetration depth. Many of the prediction methods which have been studied are based on the bearing capacity theory. In essence this theory assumes that the soil will fail if the stagnation pressure (section 3.1.3) is equal or larger than the bearing capacity of the soil. For cohesive soils, the bearing capacity is calculated by multiplying the undrained shear strength s_u of the soil with the bearing capacity factor N_c (Zhang, Ge, et al., 2016).

$$q = N_c s_u \tag{3.12}$$

where q : Bearing capacity [Pa]
N_c : Bearing capacity factor for cohesive soils [-]

For purely cohesive soils, the bearing capacity factor is found to be: $N_c = 2 + \pi \approx 5.14$ (Prandtl, 1920). Another value for the bearing capacity factor which is widely used is $N_c = 6$. Using equation 3.11 and 3.12, a threshold for the jet velocity at the exit of the nozzle can be formulated.

$$u_0 \geq \sqrt{\frac{2N_c s_u}{\rho_w}} \tag{3.13}$$

Using this theory, different depth predictions formulas have been formulated. They are summarized in equation 3.14. Various studies have found different values for f, the most commonly used are given in table 3.1.

$$\frac{d}{D_n} = f\sqrt{\frac{p_j}{N_c s_u}} \tag{3.14}$$

where d : Cavity depth [m]

Study	Factor f
Nobel (2013)	6.2
Machin et al. (2011)	6
Ho (2005)	6.25

Table 3.1: Different values factor f

Using the factor f Nobel (2013) found and N_c = 6, an equation for the penetration depth in the form of equation 3.14 can be found by combining equation 3.1 and 3.11. The cavity depth can be calculated with the nozzle diameter, the jet pressure and the shear strength of the clay. Typically these parameters will be known during a jet trenching operation.

$$d = 24.8 D_n \frac{\sqrt{p_j}}{\sqrt{s_u}} \tag{3.15}$$

Equation 3.15 applies to a single stationary nozzle and predicts the penetration depth only on the bearing capacity theory. Other factors such as the time dependent erosion are not taken into account. Generally the penetration depth of a single jet can be divided into two parts, the quasi-instantaneous part and the time-dependent part (see figure 3.4a and 3.4b).

3.1.5. Time Dependent Jet Erosion

The quasi-instantaneous part is the initial phase of the jet penetration, which is characterized by a high-velocity impact of the jet on the soil surface. This component is related to the formation of the impact cavity and the immediate soil erosion caused by the high-pressure jet. The time-dependent part of the jet penetration is the slower, long-term process that occurs after the initial impact. This component is related to the soil erosion caused by the jet over time and is influenced by factors such as the soil type, the water content, and the jet pressure.

Understanding the interaction between these two components is important for predicting the penetration depth and the overall effectiveness of jet trenching. Experiments performed by Machin et al. (2001) confirm that the quasi-instantaneous cavity depth occurs almost immediately whereas the time-dependent part takes a few seconds to develop. When a jet has a horizontal velocity, the jet exposure time can be translated to the forward velocity. From figure 3.4b it follows that for a very low forward velocity, the fully (or close to fully) developed cavity depth can be used.

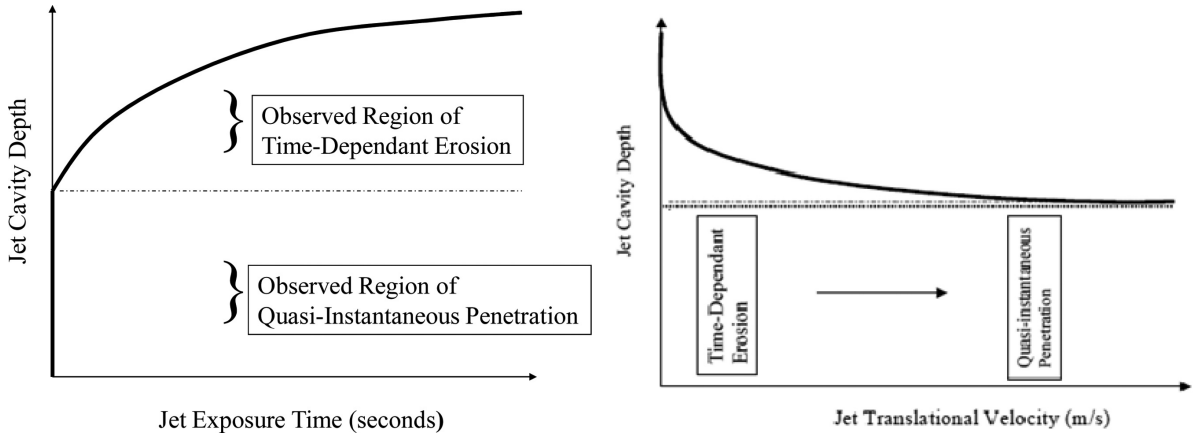

(a) Jet cavity depth versus exposure time

(b) Jet cavity depth versus forward velocity

Figure 3.4: Time dependence cavity depth (Machin et al., 2011)

Tests performed by Machin et al. (2011) show that the quasi-instantaneous cavity depth correlates very closely to bearing capacity theory. The theory assumes the soil to fail as long as the stagnation pressure is higher than the bearing capacity (section 3.1.4).

3.2. Previous Research on Moving Vertical Jets in Cohesive Soils

Understanding the effect of forward velocity on the penetration and behavior of a jet in cohesive material is crucial for jet trenching since it involves a moving operation. As noted earlier, the time-dependent aspect of jet penetration in cohesive materials means that the forward velocity of a moving jet can have a significant impact on penetration depth. Over the years, various methods have been developed to study the behavior of moving vertical jets, including physical experiments, analytical models, and numerical simulations. These methods aim to provide insight into the factors that affect the performance of the jet, such as forward velocity, nozzle geometry, soil properties, flow velocity and water pressure. By better understanding these factors, it is possible to develop more accurate models for moving jet behavior.

3.2.1. Failure Mechanisms of Clay Exposed to a Moving Jet

Cohesive soil fails if it exposed to a certain pressure which is higher than the bearing capacity as described in 2.2.4. The failure will occur along a shear plane. When a soil is exposed to a stagnation pressure by a moving jet it experiences different loading conditions. The conditions are illustrated in figure 3.5.

Nobel (2013) showed that the impact of failure mechanism a, b and c is significantly larger than the other two. Therefore, failure mechanism d and e from figure 3.5 are negligible.

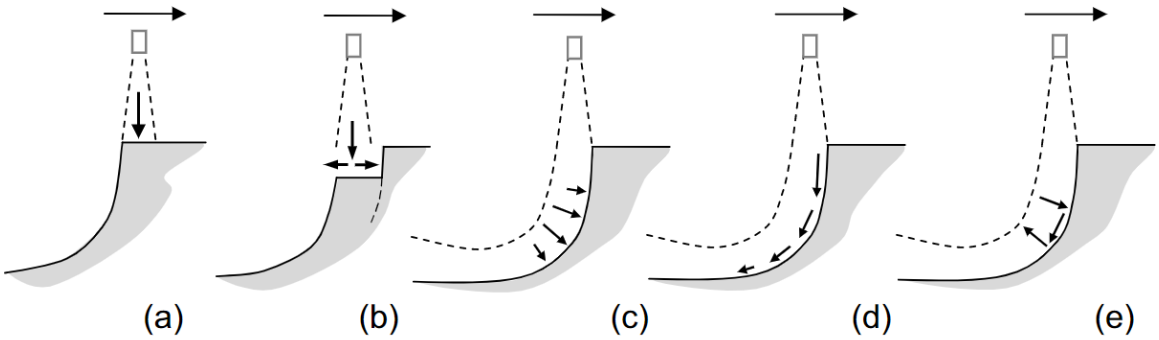

Figure 3.5: Loading conditions of single moving jet (Nobel, 2013)

where	a :	Normal pressure parallel to the jet flow	[Pa]
	b :	Normal pressure perpendicular to the jet flow	[Pa]
	c :	Normal pressure perpendicular to the jet flow due to deflection	[Pa]
	d :	Shear stress exerted by the jet flow	[Pa]
	e :	Temporary normal pressure due to turbulence	[Pa]

When a moving jet is penetrating into the soil, the penetration can be divided into two zones. The non-deflection zone and the deflection zone. The two zones are illustrated in figure 3.6. The non-deflection zone is characterized by the small shear planes along which the soil fails, this results in small particles which are transported by the jet. The shear planes in the deflection zone are much larger which naturally lead to larger "lumps" of soil being created by the penetrating jet.

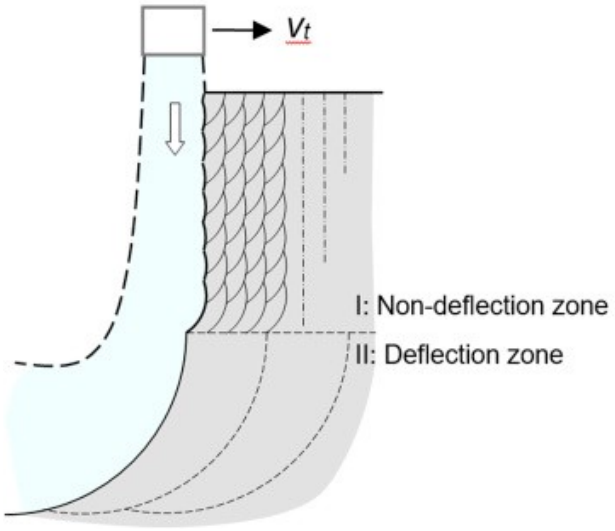

Figure 3.6: Non-deflection and deflection zone (Nobel, 2013)

The length of the non-deflection zone depends on the jet ratio $\frac{p_j}{su}$ and the forward velocity (denoted as v_t in figure 3.6). Experiments performed by Nobel (2013) show that for forward velocity $v_t < 0.1\ \mathrm{m\,s^{-1}}$ the deflection zone becomes small enough to be negligible compared to the non-deflection zone. Since a jet trenching operation in cohesive soil is usually slower than this ($v_t \approx 100\mathrm{m\,h^{-1}} \approx 0.03\mathrm{m\,s^{-1}}$), only non-deflecting jets will be considered. With a forward velocity $v_t < 0.1\ \mathrm{m\,s^{-1}}$, the entrainment of particles into the jet can also be neglected.

3.2.2. Failure Modes of Clay Exposed to a Moving Jet

In his thesis, Nobel (2013) has studied the process of a moving vertical jet above clay soil extensively. During the experiments, a variation of forward velocity and ratio between the jet pressure and undrained shear stress $\frac{p_j}{s_u}$ has been used. With the results from the experiments he found a linear relation between the normalized cavity depth $\frac{d}{D_n}$ and the jet ratio $\frac{p_j}{s_u}$. The relation was found to be valid up to a jet ratio $\frac{p_j}{s_u}$ of 400. Based on the cavity characteristics and the jet ratio, four failure modes can be distinguished.

- **Penetrating jet**
  - $\frac{p_j}{su} > 12$
  - Narrow deep cavities
  - A soil wall structure with small straight nearly vertical nerves
  - Excavated soil that dissolves completely in the jet and ambient water
- **Deflecting jet**
  - $7.3 < \frac{p_j}{su} < 12$
  - Shallow cavities
  - A soil wall texture with nerves deflecting in the direction opposite the traverse direction of the nozzle
  - Excavated soil that dissolves completely in the jet and ambient water
- **Dispersing jet**
  - $5.7 < \frac{p_j}{su} < 7.3$
  - Wide shallow cavities
  - An irregular soil wall structure
  - Dislodged soil lumps that can be found after the tests
- **Hydro-facturing**
  - Occurs sporadically at very low forward velocities $v_t < 0.15\ \mathrm{m\,s^{-1}}$
  - Irregular cavity dimensions
  - The soil fails along preferred weak surfaces
  - Cavity dimensions can increase significantly, compared to the penetrating and deflecting jet

Most tests conducted were of the penetration jet type with the same cavity shape and wall structure. The forward velocity of the jets during the the test which resulted in a penetration jet were $0.25 - 1.5\ \mathrm{m\,s^{-1}}$. It should be noted that this a lot faster than a jet trenching operation would take place. A typical speed for jet trenching in clay is $v_t \approx 100\ \mathrm{m\,h^{-1}} \approx 0.03\ \mathrm{m\,s^{-1}}$. As mentioned in section 3.2.1, the length of the deflection zone mainly depends on the jet ratio and the forward velocity of the jet. Nobel (2013) proposed an analytic approach to calculate the cavity shape if $v_t < 0.1$, which were failure modes of the penetration type. For that reason, only penetrating jets from his studies will be considered in this study. The analytical model will be elaborated in section 3.2.3.

3.2.3. Moving Penetrating Jet Modelling

Penetration Principle

To describe the behaviour of a moving penetrating jet, Nobel (2013) defined a boundary and a mixing layer (figure 3.7 b). The boundary layer is defined as the layer where soil particles entrain the jet whereas only ambient water entrains from the back of the jet, creating a mixing layer. The boundary layer at the front of the jet is comparable to the development of the boundary layer in an uniform flow on a rough plate. Assuming the influence of the decelerating flow and soil entrainment are negligible, they are not included. With that assumption, the bed shear stress exerted by the boundary layer at the front of the jet can be calculated.

$$\tau_b = c_f \frac{1}{2} \rho u_{bl,max}^2 \tag{3.16}$$

where τ_b : Bed shear stress [Pa]
c_f : Friction coefficient [-]
$u_{bl,max}$: Jet velocity at the edge of the boundary layer [$\mathrm{m\,s^{-1}}$]

From a calculation method proposed by Nobel (2013), the bed shear stresses are in the order of magnitude of 1-2% of the corresponding stagnation pressure. Therefore, the influence of the bed shear stresses can be neglected.

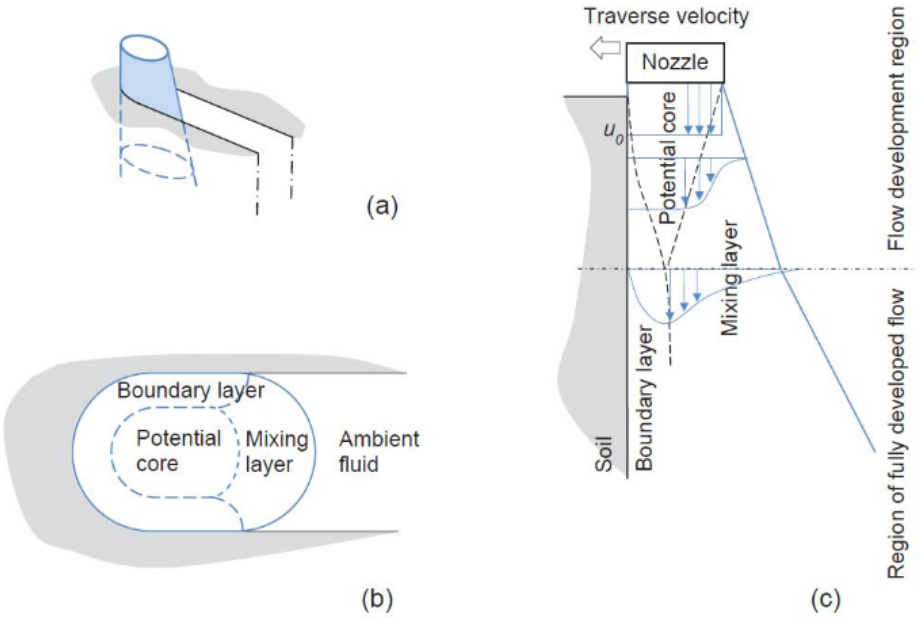

Figure 3.7: Vertical penetrating moving jet: (a) overview (b) horizontal cross section (c) vertical cross section (Nobel, 2013)

Entrainment of soil particles in the boundary influences the jet velocity development and with that the stagnation pressure. Entrainment of soil particles mainly depends on the forward velocity of the jet. For very small velocities ($v_t < 0.1\ \mathrm{m\,s^{-1}}$), the influence of entrainment on the velocity development of the jet can be neglected.

Penetration Depth

The maximum cut depth required for progress rate assessment in jet trenching is the maximum value calculated for inward and forward nozzles. The cut depth achievable by the jet nozzles depends on the pressure exerted on the clay surface by the jet, which can be calculated from the jet flow velocity. In order to start a cut, the jetting pressure must be high enough to cause a bearing capacity failure of the soil, which is given by Equation 3.17:

$$p_j > N_c S_u \tag{3.17}$$

where N_c is the bearing capacity factor (typically $N_c = 6$) and S_u is the undrained shear strength in kPa. The jet velocity required to cause bearing capacity failure is obtained from Equation 3.18:

$$v_j = \sqrt{\frac{2 N_c S_u}{\rho_w}} \approx 3.5 \sqrt{S_u} \tag{3.18}$$

where v_j : Jet velocity [$\mathrm{m\,s^{-1}}$]

Machin et al. (2011) demonstrated the relationship between SOD, x, and the nozzle pressure, p_j, to cause the bearing capacity failure. With the assumption of SOD, x, as the depth of cut that can be made for a jet located at the surface of the soil, the total depth of cut can be derived by combining the above equations as shown in Equation 3.19:

$$\frac{x}{d} = 2.53\sqrt{p_j S_u} \tag{3.19}$$

where d : Jet diameter [m]

The depth of cut derived from the bearing capacity theory appears to develop nearly instantaneously (in a fraction of a second). Subsequently, the cavity generally reaches its full depth over several seconds in cohesive soils, as indicated in Figure 3.4a.
Jet trenching involves the jets traversing rather than remaining static. Atmatzidis and Ferrin (1983) indicated that the penetration depth, x, could be related exponentially to the jet's traversing velocity, v_t, as shown in Equation 3.20:

$$x = x_{max}\left(1 - e^{-\frac{\zeta}{v_t}}\right) \tag{3.20}$$

where x : Penetration depth [m]
x_{max} : Limiting penetration for a stationary jet after infinite time [m]
ζ : Emperical constant with units of velocity [m s^{-1}]

Machin et al. (2011) suggests to use the quasi-instantaneous penetration from figure 3.4b when calculations are made for a jet trenching operation. He acknowledges that this is an over-conservative approach because the time dependent part of the penetration is always observed in the experiments. However, the process of estimating the time-dependent part of the penetration is a soil softening and and particle erosion effect which is dependent on the permeability, a property which is often difficult to predict with accuracy. In this case, the cavity depth should be calculated using the bearing capacity theory (equation 3.15).

For penetrating jets with a very small forward velocity ($v_t < 0.1$ m s^{-1}), Nobel (2013) proposed a simple analytical model. Due to the small velocity, entrainment of soil into the jet is neglected in this model. The model is only valid for non-cavitating jets (section 3.1.2). The cavity width is assumed to be equal to the diameter of the jet at the original impact point of the jet to the soil.

Penetrating jets were found at jet ratios ratios larger than 12, for a small SOD, jet pressure is about equal to the stagnation pressure.

$$\frac{p_j}{s_u} \approx \frac{p_{stag}}{s_u} > 12 \tag{3.21}$$

This is much larger than the theoretical stagnation pressure for the soil to fail which is $6.2 s_u$. Therefore, the whole jet is assumed to penetrate the soil and the cavity width is assumed to be equal to the jet diameter at the stagnation point ($W_c = D_j$), for small SOD this is approximately equal to the nozzle diameter ($W_c = D_j \approx D_n$).

The penetration depth in this model is based on the bearing capacity theory as described in section 3.1.4, however the bearing capacity factor N_c was found to be 8.2 for cavities larger than 1.6 times the jet diameter at the stagnation point. For this model, the jet diameter is assumed to be equal to the cavity width. With this, an equation can be derived for the cavity depth d.

$$\frac{d}{D_n} = a_1 \frac{p_j}{s_u} + b_1 \tag{3.22}$$

where:
for $d + SOD < s_{dr}$:

$$a_1 = \sqrt{\frac{k}{2}} \frac{1}{N_c(2N_1 + 1)} \tag{3.23}$$

$$b_1 = -\sqrt{\frac{k}{2}}(N_1 + 1) \tag{3.24}$$

for $d + SOD \geq s_{dr}$:

$$a_1 = \sqrt{\frac{k}{2}} \frac{1}{N_c(2N_1 + 1)} \tag{3.25}$$

$$b_1 = -\sqrt{\frac{k}{2}} N_1 \tag{3.26}$$

where N_1 is defined as:

$$N_1 = \frac{SOD}{s_{dr}} \tag{3.27}$$

For small stand-off distances ($SOD < D_n$), equation 3.22 becomes:

$$\frac{d}{D_n} = 0.65 \frac{p_j}{s_u} - 7.2, \text{if } 15 < \frac{p_j}{s_u} < 19 \tag{3.28}$$

$$\frac{d}{D_n} = 0.33 \frac{p_j}{s_u} - 1, \text{if } \frac{p_j}{s_u} > 19 \tag{3.29}$$

Another method to predict the penetration depth of a moving jet was proposed by Zhang, Ge, et al. (2016). In this study, the performance of traveling jet trenching in stiff clay was investigated, with all key parameters varied in the experiment including the jet velocity, shear strength of clay, diameter of the nozzle, and forward velocity of the nozzle. The jet-soil interface was found to be an arc, illustrated figure 3.8.

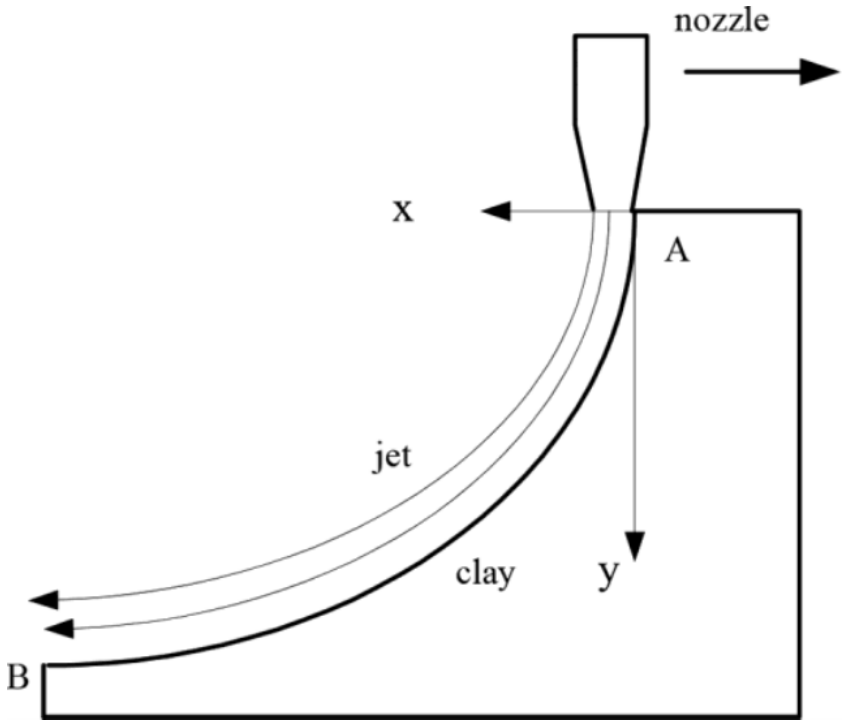

Figure 3.8: Jet soil interface (Zhang, Ge, et al., 2016)

Based on the jet-soil interface, a method for predicting jet-trenching depth was presented. First, the trajectory of the jet-soil interface was calculated, and then the distribution of the boundary layer shear stress along the interface was predicted. A set of equations was developed to perform these calculations. The ultimate trenching depth was found to be at the point where the wall shear stress was equal to the critical shear strength of clay.

$$\begin{aligned} \frac{y}{D_n} &= k(\frac{p_j}{s_u})^a(\frac{v_j}{v_t})^b(\frac{x}{D_n})^c \\ l &= \int_0^x \sqrt{1+(\dot{y})^2}dx \\ C_f \frac{2l}{D_n\sqrt{\pi}}\rho_w v_j &= f s_u \end{aligned} \tag{3.30}$$

where	x	:	Horizontal component of the jet soil interface trajectory	[m]
	y	:	Vertical component of the jet soil interface trajectory	[m]
	v_j	:	Jet flow velocity	[m s^{-1}]
	a, b, c, k	:	Empirical constants	[-]
	l	:	Arc length of the jet soil interface trajectory	[m]
	C_f	:	Wall shear stress coefficient	[-]
	f	:	Emperical constant for critical shear strength (Kamphuis and Hall, 1983)	[-]

Ho (2005) showed in his experiments that the value of f ranges from 0.001 to 0.002. To calculate the wall shear stress coefficient C_f, theory by Rajaratman (1982) can be used to derive equation 3.31.

$$\begin{aligned} C_f = &-5.533018 * 10^{-11}(\frac{2l}{D_n\sqrt{\pi}})^5 \\ &+1.3147 * 10^{-8}(\frac{2l}{D_n\sqrt{\pi}})^4 \\ &-1.171488 * 10^{-6}(\frac{2l}{D_n\sqrt{\pi}})^4 \\ &+1.931478 * 10^{-4}(\frac{2l}{D_n\sqrt{\pi}})^2 \\ &-3.697546 * 10^{-2}(\frac{2l}{D_n\sqrt{\pi}}) \\ &-2.314712 \end{aligned} \tag{3.31}$$

The experiments performed by Zhang, Zhao, et al. (2016), the following values for the empirical constants where found:

$$\begin{aligned} a &= 0.83 \\ b &= 0.445 \\ c &= 0.16 \\ f &= 0.001 \\ k &= 0.117 \end{aligned}$$

Using these constant together with equation 3.30 and 3.31, the following steps should be followed to calculate the trench depth (when D_n, s_u, p_j, v_t are known):

Step (1):
Calculate the jet soil interface according to equation 3.30 (a).
Step (2):
Find $\dot{y}$ and calculate the ultimate erosion arc length l according to equation 3.30 (c) and 3.31.
Step (3):
Find the horizontal component of the interface x according to the integral in equation 3.30 (b) by using the trial method.
Step (4):
Substitute x in equation 3.30 and solve for y. The trench depth is equal to the vertical component of the jet soil interface y.

Computational Fluid Dynamics (CFD)

CFD is a computational method used to simulate and analyze fluid flow and related phenomena using numerical techniques. It involves solving complex equations that describe fluid behavior using computer algorithms. CFD can be used to predict and understand fluid flow patterns, pressure distributions, and temperature profiles in various applications.

Wang et al. (2021) has developed a CFD model to simulate the behavior of high-pressure jets in cohesive soil during offshore and dredging operations. The model combines the finite volume method and a segregated approach inspired by the PISO algorithm by Issa (1985), to solve the momentum, transport, and pressure-poisson equations implicitly.

The input parameters for the model are the jet ratio (ratio of jet pressure p_j to undrained shear strength s_u), forward velocity, and flow velocity. The model's results are validated against data from Nobel (2013). The CFD simulations depicted in figure 3.9 clearly show a distinction between the deflection zone and the non-deflection zone as described in section 3.2.1.

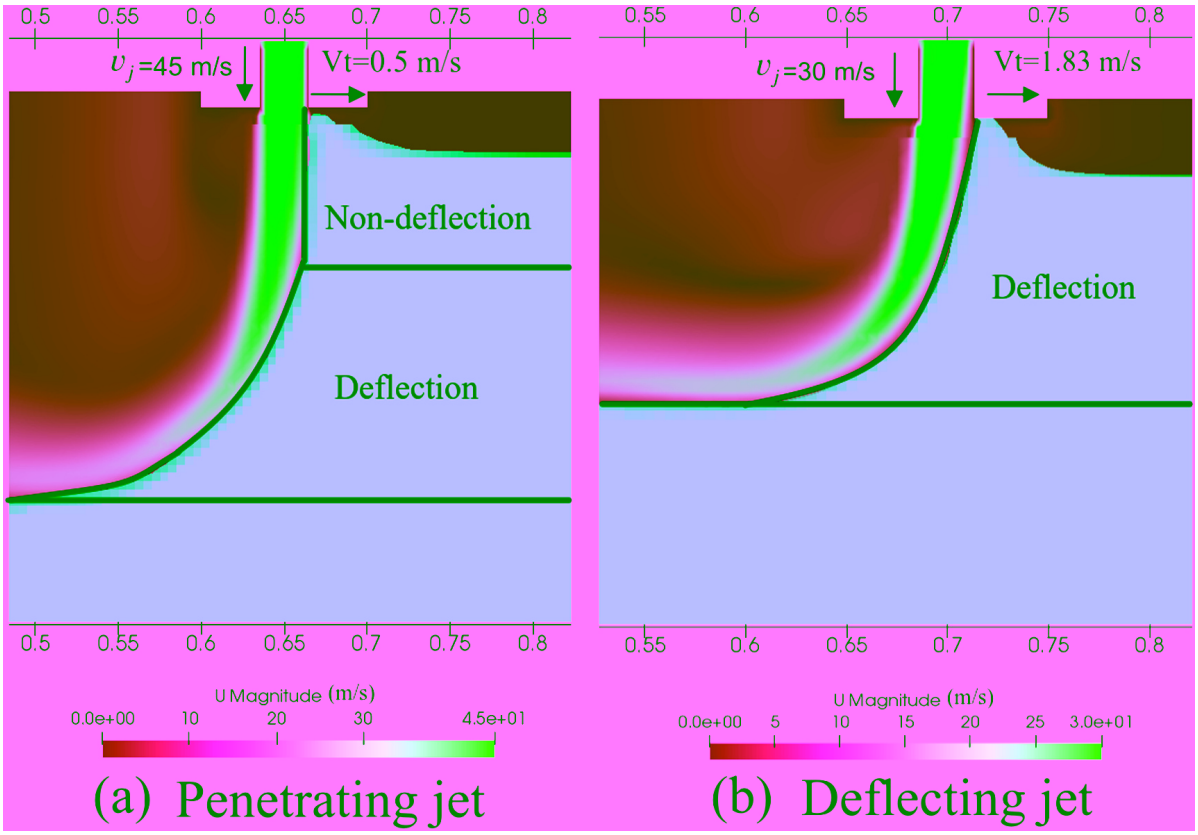

Figure 3.9: Fluid velocity and cavity shape (Wang et al., 2021)

The CFD simulation is compared to experimental data from Nobel (2013) to analyze the soil surface dislodgement rate and pressure exerted on the soil. The dislodgement rate calculated by CFD shows a cyclic behavior. The maximum pressure on the soil surface changes periodically, indicating a discontinuous failure mechanism. Based on these insights, Wang et al. (2021) proposed a simplified failure model which aims to understand the cyclic behavior of the jet excavation process. It assumes that the jet needs to travel a certain distance on the soil element before the momentum transfer is sufficient to overcome the soil strength and form a shear plane. The model aims to predict cavity depth, vertical dislodgement velocity, distance traveled by the jet before failure, and the time between cycles. It involves four equations that consider the jet velocity, nozzle diameter, undrained shear strength, and forward velocity.

$$
\begin{aligned}
v_c &= \frac{1}{2}\alpha v_j \\
h &= \frac{\alpha v_j}{8\tau_y v_t}\left(\sqrt{(w\tau_y)^2 + \frac{16\tau_y v_t \pi r^2 \beta \rho_f v_j}{\alpha}} - w\tau_y\right) \\
\Delta t &= \frac{h}{v_c} \\
\Delta x &= v_t \Delta t
\end{aligned}
$$

where	v_c	:	Dislodgment velocity	[m s^{-1}]
	v_j	:	Jet flow velocity	[m s^{-1}]
	v_t	:	Forward velocity	[m s^{-1}]
	h	:	Cavity depth	[m]
	w	:	Cavity width	[m]
	τ_y (= s_u)	:	Shear stress	[Pa]
	r	:	Nozzle radius	[m]
	Δt	:	Time between cycles	[s]
	Δx	:	Distance travelled by jet before failure	[m]

The simplified failure model's equations yield formulas for the vertical dislodgement velocity (v_c), cavity depth (h), distance traveled by the jet before failure (Δx), and the time between cycles (Δt). These formulas involve coefficients (α and β) that represent the distribution of momentum and energy in the jet flow and soil mechanical deformations. The coefficients are influenced by factors such as the jet traverse velocity, clay strength, and jet pressure.

The CFD model accurately predicts the cavity depth for a range of jet pressures, undrained shear strengths of the soil, and traverse velocities. It also confirms that the failure process of high-pressure jets in cohesive soil at high traverse velocities is a discontinuous process with a specific periodicity. The CFD simulations provide valuable information on shear and pressure evolution during cavity formation.

Cavity Shape

When jet trenching is performed in cohesive material, the shape of the cavities being created is an important parameter. It defines how much soil is being impacted by the jet. Different studies and experiments have found different cavity shapes. Nobel (2013) found that for penetrating jets (section 3.2.2) the cavity shape is narrow and deep en the walls are nearly vertical. Typical cavity shapes are shown in figure 3.10. It should be noted that these cavity shapes were identified with forward velocities of jet between 0.25 - 1.5 m s^{-1}. Jet trenching operations in cohesive soils usually take place at much lower forward velocities (typically around 100 m h^{-1} $\approx$ 0.03 m s^{-1}). Nobel (2013) found a relation between the width of the cavity (uniform over the depth) and the Nozzle diameter and SOD. Equation 3.32 shows the relation where s_{dr} is the distance from the nozzle where the fully developed region starts (= $6.2D_n$ equation 3.4).

$$
\begin{aligned}
W_c &= \sqrt{\frac{2}{k}} + D_n,\ SOD < s_{dr} \\
W_c &= \sqrt{\frac{2}{k}},\ SOD \geq s_{dr}
\end{aligned}
\tag{3.32}
$$

where W_c : Width of the cavity [m]

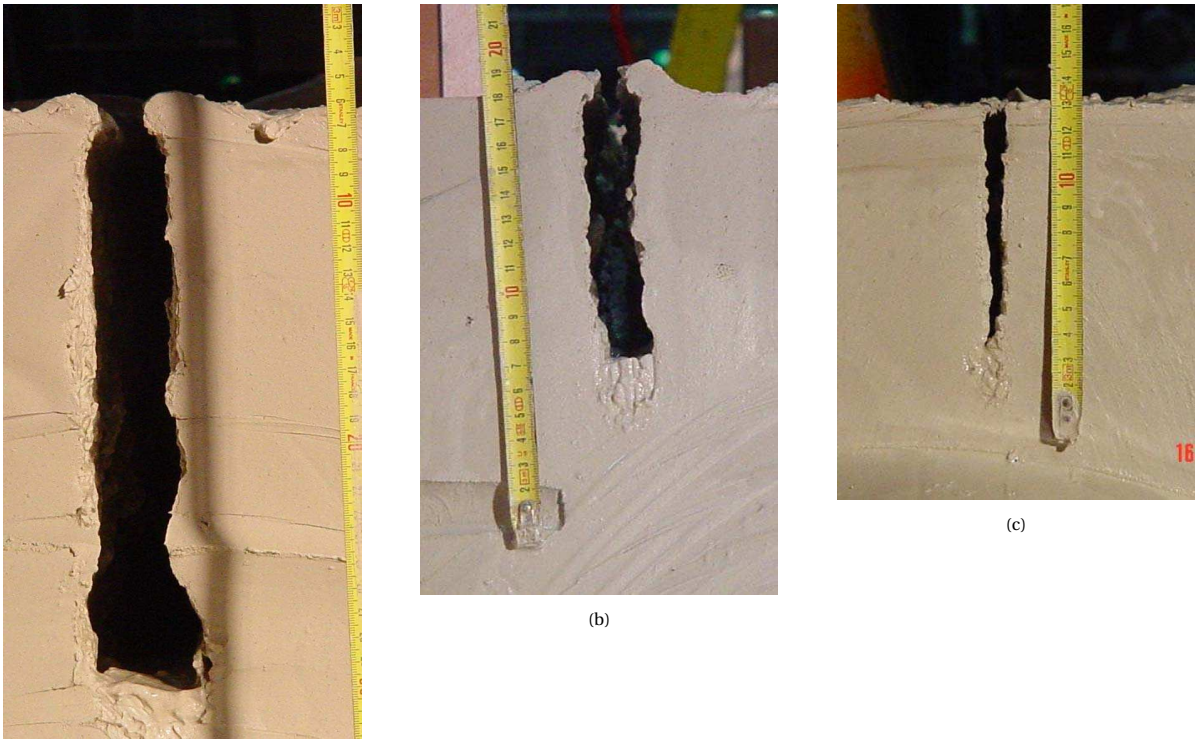

(a) (b) (c)

Figure 3.10: Typical cavity shape of a penetrating jet (Nobel, 2013)

Studies have shown that lower forward velocities lead to a different shape of the cavity created by penetrating jets in cohesive soil. Machin et al. (2011) found that for vertical jets, the cavity has a conical shape with an inclination angle α of approximately 14 degrees. Figure 3.11c provides an idealized view of the cavity. However, different studies have reported some variation in the inclination angle.

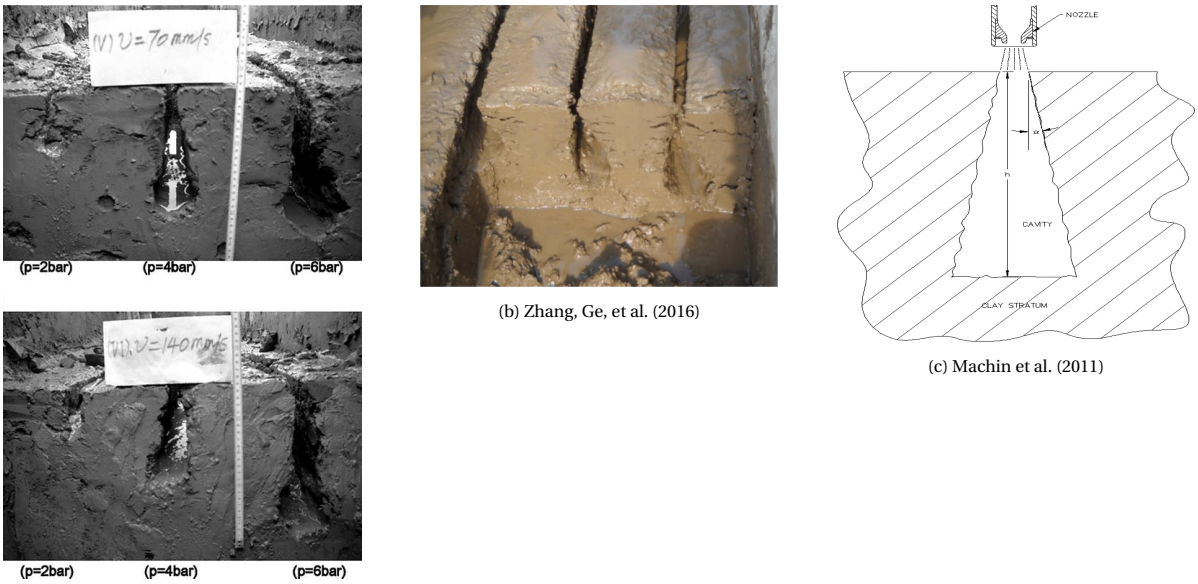

(a) Zhang, Zhao, et al. (2016) (b) Zhang, Ge, et al. (2016) (c) Machin et al. (2011)

Figure 3.11: Conical shaped cavities of penetrating jets

Experiments conducted by Zhang, Ge, et al. (2016) also revealed that the cavity shape of a penetrating jet at lower forward velocities is conical or "pear-shaped". The cavities observed in the experiments, as shown in Figure 3.11a and 3.11b, had forward velocities ranging from 0.07 - 0.28 $\mathrm{m\,s^{-1}}$. The results indicated that the lower forward velocities had a significant impact on the shape of the cavities, which differed from those observed in experiments performed by Nobel (2013).

This indicated that the exposure time of a single jet on cohesive soil defines the cavity shape it creates. At lower forward velocities, the exposure time is longer, allowing the jet disperse laterally. This leads to the formation of a conical or "pear-shaped" cavity with a narrower opening at the top and a wider base. In contrast, at higher forward velocities, the exposure time is shorter, resulting in a more cylindrical cavity with a more uniform diameter, as shown by Nobel, 2013.

3.2.4. Comparison of Different Theories and Experiments

To optimize the jet trenching process in cohesive soils, it is important to compare and analyze the different research on moving vertical jets, along with their testing settings. This is important as the shape and penetration of a moving vertical jet varies depending on various parameters, such as the undrained shear strength, jet pressure, jet velocity, forward velocity and nozzle diameter. Moreover, different research and theories have used different assumptions, which can have a significant impact on the outcome.

To make the comparison easier, a table will be included that shows the different testing settings used by Nobel, Zhang, and Machin, along with the typical jet trenching machine settings. This will allow for a better understanding of the differences between the studies and help to determine which methods are most effective for jet trenching in cohesive soils.

		Machin	Nobel	Zhang	Jet trenching
Undrained shear strength (s_u)	[kPa]	50-125	20-200	60-100	50-100
Jet pressure (p_j)	[kPa]	200-1700	400-3600	200-750	700-1400
Forward velocity (v_t)	[$\mathrm{m\,s^{-1}}$]	N/A (static tests)	0.1-2.0	0.07-0.28	$\approx$ 0.03
Nozzle diameter (D_n)	[mm]	10-38	3-40	7-28	5-20

Table 3.2: Different test apparatus

4

Sedimentation of Cohesive Material

Sedimentation is a natural process in which solid particles settle and accumulate at the bottom of a liquid due to gravity. It occurs in many natural systems, including oceans, rivers, and lakes. In the context of jet trenching, sedimentation plays a crucial role in the effectiveness of the trenching process and the depth of coverage (DOC) and depth of lowering (DOL) of the cable (figure 2.4).

During the jet trenching process, the water jets are used to cut into the soil, and the soil particles become suspended in the water. As the water carrying the suspended particles moves away from the trencher, the particles start to settle and accumulate at the bottom of the trench due to gravity. The accumulation of these particles forms a layer of sediment, which can provide protection for the cable by shielding it from any external forces and reducing the likelihood of cable damage.

However, if the sedimentation rate is too high, it can also reduce the cable's ability to sink into the trench, limiting the DOL and increasing the risk of damage due to cable curvature. This can lead to issues such as cable exposure or even cable failure. Therefore, understanding the sedimentation process is critical for ensuring the safe and effective installation of subsea cables and pipelines.

The sedimentation rate is influenced by various factors, including the soil type and properties, the water flow rate and direction, and the distance from the trencher. The properties of the soil, such as the particle size distribution, affect the settling velocity of the particles, which can impact the sedimentation rate. The water flow rate and direction also play a significant role in sedimentation.

This chapter will aim to investigate the sedimentation process in the context of jet trenching operations. It will cover the general settling velocity of particles and the specific settling velocity of clay particles as well as larger and differently shaped particles. Additionally, the chapter will explore sediment transportation and examine it from the perspective of jet trenching. Special attention will be given to the formation of clay blocks that can occur during the jet trenching process. Overall, this chapter will provide a comprehensive understanding of sedimentation and its impact on jet trenching operations.

4.1. Settling Velocity

Settling velocity refers to the speed at which a particle in a fluid (such as water) moves under the influence of gravity, as it falls or settles through the fluid. The settling velocity depends on several factors, including the size, shape, and density of the particle, as well as the properties of the fluid such as viscosity and density. The settling velocity is an important parameter in various fields of study, such as sediment transport.

4.1.1. Stokes' Law

When a solid particle is introduced into a liquid, it tends to move downwards due to its weight, while the liquid exerts an upward force called buoyancy. As the particle settles, it experiences a resistance from the liquid called the drag force (figure 4.2). The drag force was first described by George Gabriel Stokes in 1851.

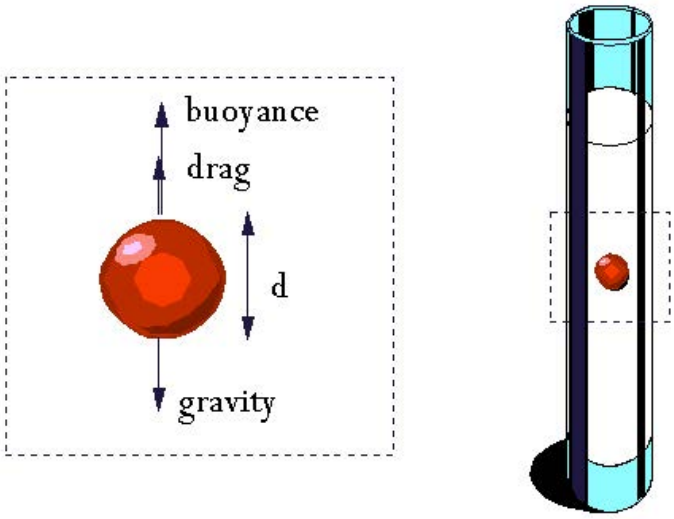

Figure 4.1: Free-body diagram of a sphere in a quiescent fluid (Shearer and Hudson, 2008)

Stokes's law describes the drag force experienced by a spherical particle in a viscous quiescent fluid.

$$F_g = 6\pi\eta r\, v_p \tag{4.1}$$

where
F_g : Drag force [N]
η : Dynamic viscocity [Pa s]
r : Radius of the particle [m]
v_p : Velocity of the particle [m s^{-1}]

Using the force balance and expressions for the gravitational and buoyancy force this can be written as the settling velocity (equation 4.2). That is the velocity at which the forces from figure 4.2 are in equilibrium.

$$\begin{aligned} w_0 &= \frac{2}{9}\frac{(\rho_s - \rho_f)gr^2}{\eta} = \frac{\triangle g d^2}{18\nu} \\ \triangle &= \frac{\rho_s - \rho_w}{\rho_w} \end{aligned} \tag{4.2}$$

where
w_0 : Settling velocity [m s^{-1}]
ρ_s : Density of the particle [kg m^{-3}]
ρ_f : Density of the fluid [kg m^{-3}]
g : Gravitational acceleration [m s^{-2}]
d : Diameter of the particle [m]
ν : Kinematic viscosity [m^2 s^{-1}]
$\triangle$: Specific density [-]

Stokes' law is only valid in the laminar regime, which is defined as the regime in which the particle Reynold number below 1.

$$Re_p = \frac{w_0 d}{\nu} \tag{4.3}$$

where Re_p : Particle Reynolds number [-]

Particles with small diameters, such as clay and silt, have a low particle Reynolds number, which is less than 1, and thus they fall into the laminar regime. On the other hand, larger particles like sand and gravel fall into the turbulence regime and settle more rapidly due to this turbulence.

Equation 4.2 shows that the settling velocity of a single particle is directly proportional to the square of its radius and the difference in density between the particle and the fluid, and inversely proportional to the viscosity of the fluid. In other words, larger and denser particles will settle faster, while particles in more viscous fluids will settle more slowly.

4.1.2. Hindered Settling

Equation 4.2 describes the settling velocity of a single particle. When multiple particles settle simultaneously, the upward water flow created by the downward motion of the particles reduces the effective settling velocity. The effective settling velocity for a large number of particles depends on the concentration and can be described by equation 4.4 proposed by Richardson and Zaki (1954):

$$w_s = w_0(1-c)^n \tag{4.4}$$

where w_s : Effective settling velocity [$\mathrm{m\,s^{-1}}$]
c : Volume concentration of particles [-]
n : Exponential value as a function of Re_p [-]

The exponent n can be calculated using the empirical method of Rowe (1987):

$$n = \frac{4.7 + 0.41 Re_p^{0.75}}{1 + 0.175 Re_p^{0.75}} \tag{4.5}$$

4.1.3. Settling Velocity of Particles of Different Size and Shape

Stokes' law is a fundamental equation used to calculate the settling velocity of particles in a fluid. However, it is not applicable to most natural particles such as rocks or large lumps of clay because it assumes several simplifying assumptions.

Firstly, Stokes' law assumes that the particle is spherical and has a smooth surface. Most natural particles are irregularly shaped and have rough surfaces, which can significantly affect their settling velocity. Secondly, Stokes' law assumes that the particle is much smaller than the fluid molecules, which is not the case for larger particles. In these cases, the Reynolds number is high and the flow around the particle becomes turbulent, which can cause a significant deviation from the Stokes' law predictions

To account for shape and size factors, Dietrich (1982) proposed a geometric shape factor:

$$E = c\left[\frac{a^2 + b^2 + c^2}{3}\right]^{-\frac{1}{2}} \tag{4.6}$$

where E : Geometric shape factor [-]
a : Longest particle axis [m]
b : Intermediate particle axis [m]
c : Shortest particle axis [m]

Dietrich (1982) fitted geometric shape factor to collected data to find an exponential value for E, $n = 0.28$. With that, Stokes' equation 4.2 becomes:

$$w_0 = \frac{\triangle g d^2}{18\nu} E^{0.28} \tag{4.7}$$

4.1.4. Settling Velocity of Clay Particles

Stokes' law describes the settling velocity of small spherical particles in a fluid medium. However, it makes certain assumptions that limit its applicability to other types of particles, such as clay particles. One key assumption of Stokes' Law is that the particles being considered are spherical in shape, which is generally true for most sand and silt particles. However, clay particles have a flat, plate-like shape (section 2.2.1), and this makes the assumption of spherical shape invalid for clay particles.

Moreover, Stokes' Law assumes that the particles do not interfere with each other, but clay particles tend to stick to each other due to electro-statical attraction and form aggregates known as 'flocs'. These flocs have a larger size than individual clay particles, and they can affect the settling velocity of the particles. The floc size and structure depend on various factors, mainly being the concentration of clay particles and the salinity of the liquid.

Therefore, Stokes' law is not directly applicable to clay particles, and other models or experimental methods are needed to accurately describe their behavior in a fluid medium. Some alternative methods for characterizing the settling behavior of clay particles include sedimentation tests, centrifugation, and laser diffraction. These methods take into account the unique physical and chemical properties of clay particles and can provide more accurate and comprehensive information about their behavior in a fluid medium (L. Van Rijn, 2020).

L. C. Van Rijn (2007) studied flocculation and the influence on the settling velocity extensively. He proposed an approach to represent the concentration-dependent mud (mixture of clay, silt and sand) settling velocity. It provides a simple yet effective method to estimate the settling velocity of mud particles in different concentration ranges. This approach was developed based on experimental observations and is widely used in the field of sediment transport research and engineering. The approach divides the influence of the concentration on the settling velocity into two ranges (see figure 4.2). The flocculation range, where the settling velocity increases because the particles settle in each others shadow. And the hindered settlement range, where the settling velocity decreases due to upward flow created by the settling particles.

The approach consists of two equations that describe the settling velocity of mud particles in different concentration ranges. In the flocculation range the settling velocity is determined as follows:

$$\begin{aligned} w_{mud} &= \exp(\alpha_1 \ln(c) + \alpha_2 - \alpha_3), \text{ for } c \leq 0.0025 \\ \alpha_1 &= 0.18 \ln(w_{mud,max} / w_{mud,min}) \\ \alpha_2 &= 2.1 \ln(w_{mud,max}) \\ \alpha_3 &= 1.1 \ln(w_{mud,min}) \end{aligned} \tag{4.8}$$

where

w_{mud}	:	Concentration-dependent mud settling velocity	$[\mathrm{m\,s^{-1}}]$
$w_{mud,max}$	:	Maximum settling velocity at $c = 0.0025$	$[\mathrm{m\,s^{-1}}]$
$w_{mud,min}$	:	Minimum settling velocity at $c = 0.00001$	$[\mathrm{m\,s^{-1}}]$
α_1, α_2 and α_3	:	Constants depending on $w_{mud,max}$ and $w_{mud,min}$	[-]

$w_{mud,max}$ and $w_{mud,min}$ are input parameters and range from 0.0005-0.003 $\mathrm{m\,s^{-1}}$ and 0.00005-0.0001 $\mathrm{m\,s^{-1}}$ respectively.

For the hindered settling range, in which the settling velocity decreases due to hindered settling effects, the settling velocity is determined as follows:

$$w_{mud} = w_{mud,max}(1-c)^4, \text{ for } c > 0.0025 \tag{4.9}$$

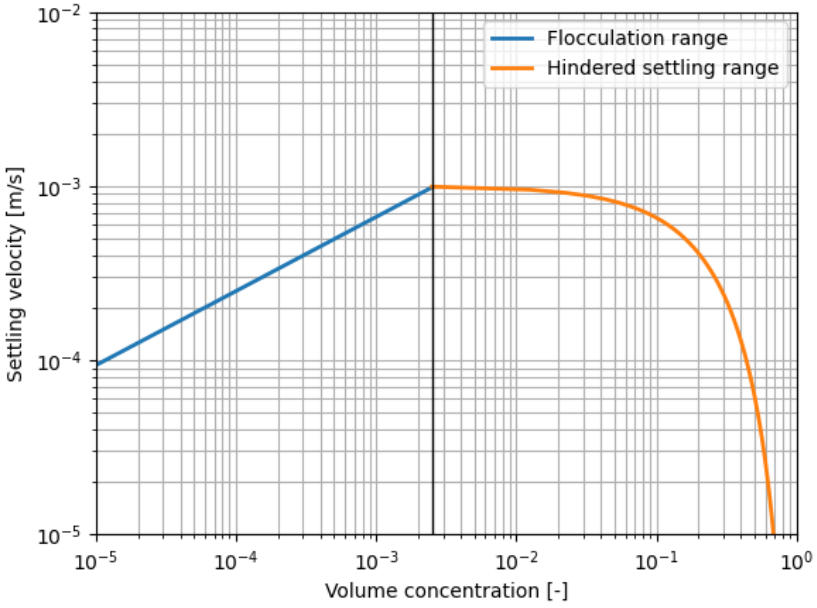

Figure 4.2: Settling velocity for $w_{mud,max} = 0.001\ \mathrm{m\,s^{-1}}$ and $w_{mud,min} = 0.0001\ \mathrm{m\,s^{-1}}$

4.2. Sediment Transport

In the context of jet trenching, it is essential to determine where sediment particles will deposit, whether it is before or after the cable sinks into the trench. To predict particle deposition accurately, it is necessary to take into account the flow behind the jet trenching machine. While the derivation of settling velocity in section 4.1 was based on particles in stationary water conditions, the Camp based model offers a solution for calculating grain settling efficiency in sedimentation tanks. With some modifications, this model can be adapted to predict the distance at which particles will settle after being suspended by jet trenching. In this section, the Camp model will be introduced and discussed to show it can be modified for use in predicting particle deposition in the context of jet trenching.

4.2.1. Camp Based Model

Camp (1936) introduced an ideal settlement tank which consists of 4 zones as shown in figure 4.3A:

1. **Inlet zone:** Inlet of a mixture where the concentration as well as the horizontal velocity distribution is uniform over the depth.
2. **Settling zone:** Zone where the settlement of particles takes place and the horizontal velocity distribution is uniform over the depth.
3. **Outlet zone:** Outlet zone where the fluid/mixture is collected uniformly over the cross-section.
4. **Sludge/Sediment zone:** Zone where the particles settle.

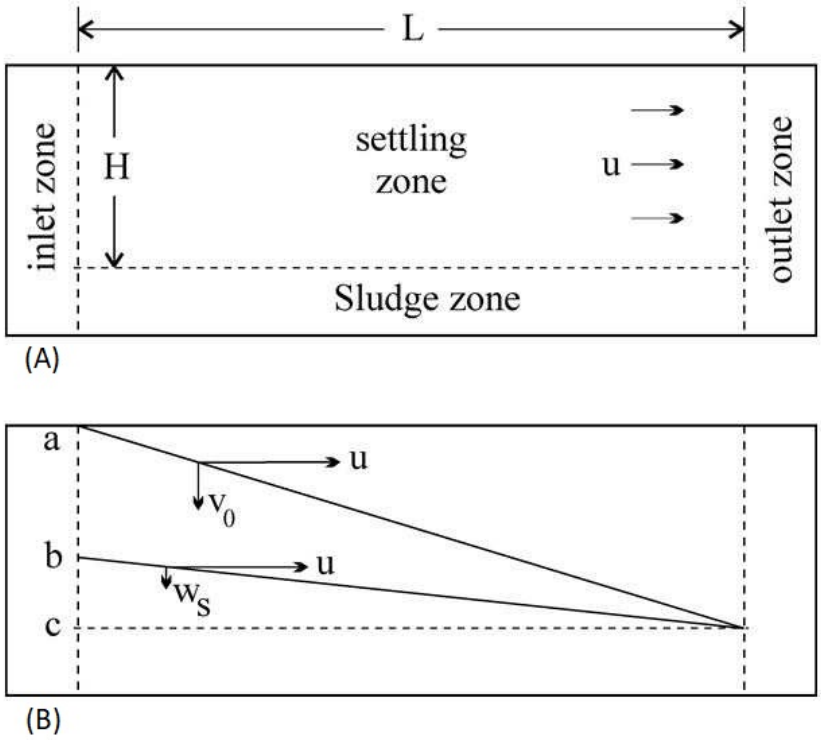

Figure 4.3: Ideal settling tank according to Camp (Van Rhee, 2017)

In Figure 4.3B, the trajectories of two particles are shown, one with a settling velocity of v_0 and the other with a settling velocity of w_s. Both particles have a horizontal velocity of u. The figure can be interpreted as follows: for particles with settling velocity v_0, all particles will settle in the tank. However, for particles with settling velocity w_s, only those particles that enter the inlet zone between points b and c will settle and deposit. Particles that enter above point b will be discharged from the settling tank without settling.

The Camp model is a widely used for calculating the settling efficiency of grains in a sedimentation tank or a hopper for dredging purposes. However, for jet trenching operations, the model needs to be modified. The application of the Camp model is depicted in figure 4.4. A jetting sword with forward velocity v_t is creating a trench and is shown in blue. Here the backward flow is assumed to be horizontal and uniform over the depth (in red). The trajectory of a particle with settling velocity w_s is shown in green.

In this modified model, the inlet zone is considered as the point where the jetting sword hits the trench depth, and initially an infinitely long settling zone is assumed behind it. By knowing the flow velocity u, settling velocity w_s, and the height at which the particle enters the inlet zone H, the length of the actual settling zone, denoted as L, can be calculated using basic geometry.

$$L = \frac{uH}{w_s} \tag{4.10}$$

where
L : Distance from the jetting sword where the particle settles [m]
u : Horizontal flow velocity in the trench [$\mathrm{m\,s^{-1}}$]
H : Heigth at which the particle enters the trench [m]
w_s : Settling velocity of the particle (section 4.1) [$\mathrm{m\,s^{-1}}$]

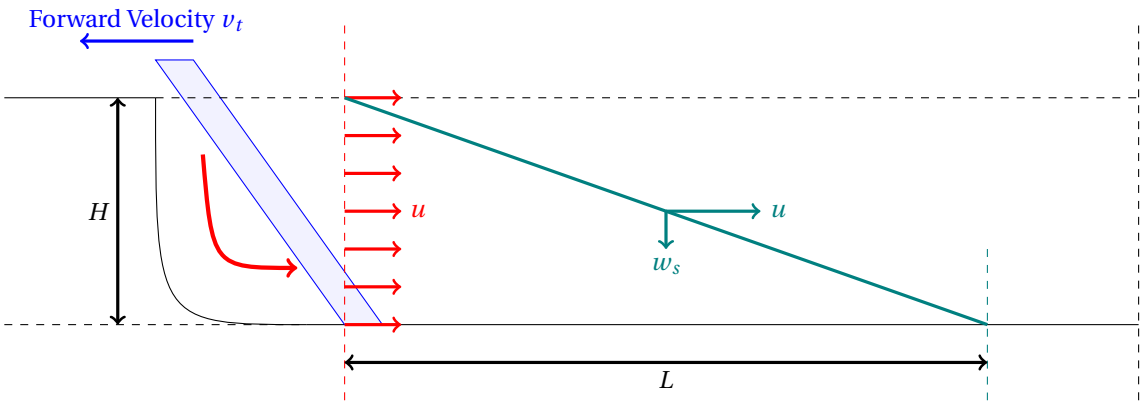

Figure 4.4: Camp based model for jet trenching

The model can predict the sediment zone behind the trencher by calculating the settling velocity and the distance at which particles will deposit. This allows for the determination of the amount of sediment cover that will be present over the cable. By combining this with the formulas for cable shape (equation 7.1), the DOC and DOL of the cable during jet trenching can be predicted as depicted in figure 4.5.

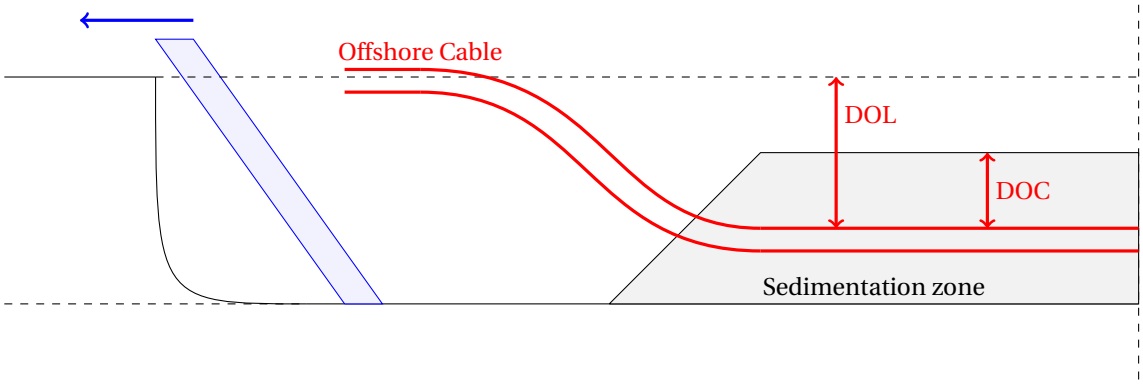

Figure 4.5: DOC and DOL with Camp based model

The assumptions made in the Camp-based model are critical for accurately predicting the behavior of sediment particles in jet trenching operations. It is essential to understand these assumptions to interpret the results correctly. The following assumptions are made in the Camp-based model:

- **The flow is assumed to be laminar:** In jet trenching operations, the flow is turbulent due to the high velocity of the water jet.
- **The flow is assumed to be horizontal:** The model assumes that the flow is horizontal, which may not be the case in practical situations. The flow may be inclined or vertical, which can affect the behavior of sediment particles.
- **The flow is assumed to be steady and uniform over the depth:** The model assumes that the flow is steady and uniform, which is the case of turbulent flows. In jet trenching operations, the flow can be highly dynamic and may vary over time and space.
- **The concentration is assumed to be constant:** The model assumes that the sediment concentration is constant, which may not be accurate for practical scenarios. The sediment concentration can vary with time and space, affecting the behavior of sediment particles.
- **The fluid is assumed to be incompressible, with a constant density and viscosity throughout the system:** The model assumes that the fluid is incompressible and that the density and viscosity of the fluid remain constant throughout the system. In practical scenarios, the fluid properties may vary with time and space, affecting the behavior of sediment particles.

4.2.2. Influence of Turbulence

In previous sections, the vertical transport of particles was assumed to be solely based on settling velocity (advection), due to the simplifying assumptions made. However, in practical applications such as in a sedimentation basin, turbulent flow is present, leading to diffusive transport of particles. To include the effects of turbulence, the advection-diffusion equation can be used to model particle transport. This section summarizes the contributions of Camp (1946), Dobbins (1944), and Miedema and Vlasblom (1995) in this area. The starting point is the two-dimensional advection-diffusion equation for a mono-sized mixture, considering only one particle diameter present.

$$\frac{\partial c}{\partial t} + \frac{\partial (uc)}{\partial x} + \frac{\partial (wc)}{\partial z} = \frac{\partial}{\partial x}\left(\Gamma_x \frac{\partial c}{\partial x}\right) + \frac{\partial}{\partial z}\left(\Gamma_z \frac{\partial c}{\partial z}\right) \tag{4.11}$$

where
c : Volume concentration of particles [-]
u : Horizontal velocity of the particle [$\mathrm{m\,s^{-1}}$]
w : Vertical velocity of the particle [$\mathrm{m\,s^{-1}}$]
Γ_x : Horizontal diffusion coefficient [$\mathrm{m^2\,s^{-1}}$]
Γ_z : Vertical diffusion coefficient [$\mathrm{m^2\,s^{-1}}$]

Assuming that the horizontal velocity of particles is equal to the horizontal flow velocity and the vertical velocity of particles is equal to the settling velocity w_s, the transport equation can be simplified to:

$$\frac{\partial c}{\partial t} + \frac{\partial (uc)}{\partial x} = \frac{\partial}{\partial x}\left(\Gamma_x \frac{\partial c}{\partial x}\right) + \frac{\partial}{\partial z}\left(\Gamma_z \frac{\partial c}{\partial z} + w_s c\right) \tag{4.12}$$

The equation can further be simplified when the following is assumed:

- Stationary flow ($\frac{\partial c}{\partial t} = 0$)
- Horizontal velocity only dependent on depth ($u = u(z)$)
- Horizontal diffusion is insignificant compared to advection and therefor neglected

This leads to the following equation:

$$u\frac{\partial c}{\partial x} = \frac{\partial}{\partial z}\left(\Gamma_z \frac{\partial C}{\partial z} + w_s c\right) \tag{4.13}$$

When the hindered settling from section 4.1.4 is included, taken into account that w_s is a function of the concentration, the equation becomes:

$$u\frac{\partial c}{\partial x} = \frac{\partial}{\partial z}\left(\Gamma_z \frac{\partial c}{\partial z}\right) + w_s \frac{\partial c}{\partial z} + c\frac{\partial w_s}{\partial c}\frac{\partial c}{\partial z} \tag{4.14}$$

Camp (1946) and Dobbins (1944) simplify the equation further by assuming the following:

- The horizontal flow velocity is uniform
- Diffusion coefficient is constant over the depth and horizontal distance

This yields the equation:

$$U\frac{\partial c}{\partial x} = \Gamma\frac{\partial^2 c}{\partial z^2} + w_s \frac{\partial c}{\partial z} + c\frac{\partial w_s}{\partial c}\frac{\partial c}{\partial z} \tag{4.15}$$

Camp (1946) used the following relation between the diffusion coefficient, friction velocity and water depth:

$$\Gamma = 0.0075 H u_\star \tag{4.16}$$

$$u_\star = \sqrt{\frac{f}{8}}U \tag{4.17}$$

where
Γ : Vertical Diffusion Coefficient [$\mathrm{m^2\,s^{-1}}$]
$u_\star$: Friction velocity [$\mathrm{m\,s^{-1}}$]

An analytical solution for the advection-diffusion equation (equation 4.15) can be found using separation of variables. By expressing this solution in terms of the settling velocity (w_s), it can be substituted into the settling distance equation (equation 4.10) to calculate the settling distance with the influence of turbulence. However, it should be noted that this solution still relies on several assumptions that may not reflect the actual conditions during jet trenching in clay.

4.3. Clay Block Formation in between the Nozzles

During the jet trenching process in cohesive soils, blocks of clay can form in between the nozzles where the soil is not impacted by the jets (figure 1.3b). These blocks can be a major obstruction for the lowering of the cable to its intended depth. If the blocks deposit too quickly, they can settle at the bottom of the trench before the cable has had a chance to sink to the desired depth, limiting the effectiveness of the trenching operation (figure 4.6). additionally, it can potentially cause damage to the cable due to undesired curvature in the cable caused by the presence of these blocks. Notably the mechanism shown in figure 4.6 is not well understood. A lot of uncertainty remains in the size of the clay blocks and the dis-aggregation process.

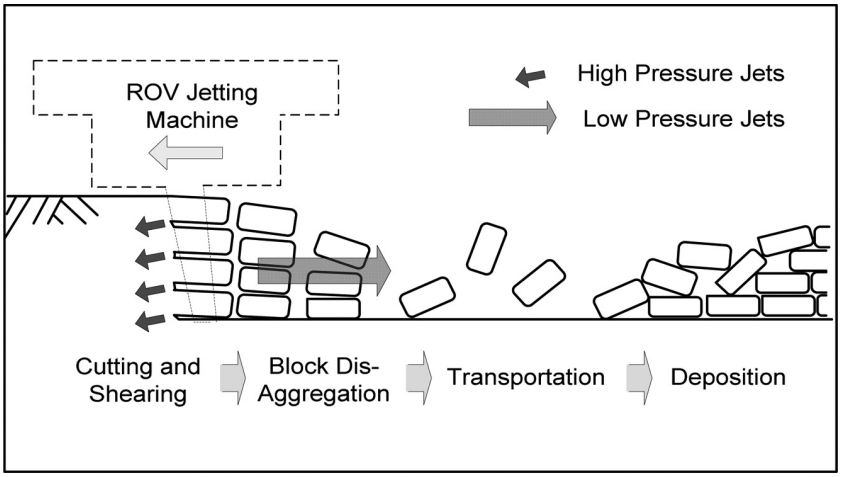

Figure 4.6: Clay blocks mechanism (Machin et al., 2011)

Although the process of clay block formation is not well understood, it is known to occur during jet trenching operations in cohesive soils. A photo taken during a project of DEME shows clay blocks that were formed during jet trenching in clay, as seen in figure 4.7. The steel cavity is part of the "Aft Cable Guide" and is positioned at the back of the jetting swords. While operating, clay lumps or blocks were produced that unintentionally get trapped in the steel frame. As a result, these blocks are brought to the surface with the machine.

Figure 4.7: Clay blocks during jet trenching in clay (photo: DEME)

In order to assess block sizes during jet trenching operations, a cantilever assessment is used as recommended by Machin et al. (2011). This means that a clay lump will be sheared off when its weight can no longer be supported by the shear strength of the clay. The cut block size depends on the spacing of inward-facing jets. It must be of a sufficient length to break under its self-weight acting as a cantilever. The limiting block size can be calculated using Equation 4.18, where the size depends on the on the undrained shear strength and clay plasticity (liquid limit *LL* see section 2.2.3), with highly plastic clay shearing off less readily.

$$B_{size} = \sqrt{\frac{N_{sp} s_u [0.1 + (1.9LL)]}{3\gamma'}} \tag{4.18}$$

where B_{size} : Length of a clay lump measured along the direction of trenching [m]
N_{sp} : Spacing between the inward facing nozzles, see figure 2.1b [m]
γ' : Submerged unit weight [kg m^{-3}]

According to Machin et al. (2011), clay lumps are transported rearwards by the flow in the same way as sand grains, and the necessary jet velocity can be assessed using a simple model based on the calculated lump size. If the size of clay lumps is too large, target burial may not be achieved, as they are deposited sooner than sand grains. The flow velocity required to transport lumps of a certain size is given by Equation 4.19.

$$B_{size} = \begin{cases} V_{req,10mm} & B_{size} \leq 10\,\text{mm} \\ V_{req,200mm} & B_{size} \geq 200\,\text{mm} \end{cases} \tag{4.19}$$

where $V_{req,10mm}$: Flow velocity required to transport lumps of 10 mm (default = 1 m s^{-1}) [m s^{-1}]
$V_{req,200mm}$: Flow velocity required to transport lumps of 200 mm (default = 6 m s^{-1}) [m s^{-1}]

Logarithmic interpolation is applied between these limits as shown in figure 4.8.

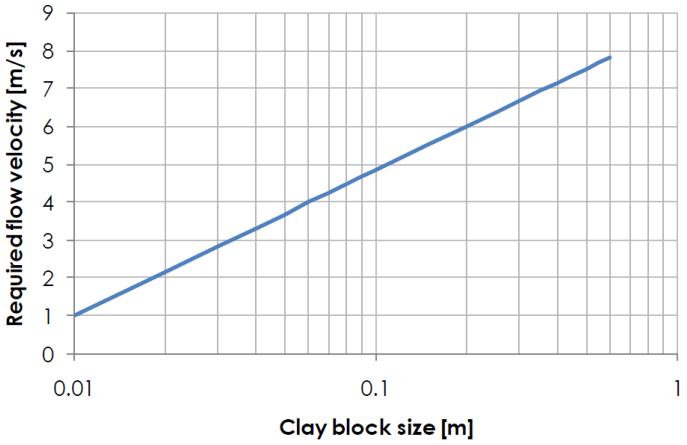

Figure 4.8: Logarithmic interpolation required flow velocity (Cathie, 2018)

The method to determine the size of blocks in jet trenching operations based on a cantilever assessment as suggested by Machin et al. (2011) has limitations in its applicability. One of the limitations is that it assumes that the clay lump will be sheared off when its weight can no longer be supported. This assumption does not take into account other factors that may cause the clay block to break or be hit by another jet during the jetting process. These factors can cause the block size to be different than predicted.

Furthermore, the method assumes that the clay blocks will fall freely without interfering with each other. However, in reality, the blocks are likely to fall on top of each other and affected by the inward and downward jets, leading to a smaller size of the blocks.

Moreover, the method relies on a simplified model to assess the necessary jet velocity based on the calculated lump size. This model assumes that clay lumps are transported rearwards by the flow in the same way as sand grains. However, in most cases, clay lumps will be deposited sooner than sand grains due to their higher settling velocity.

5

Conclusions of Literature Review

After conducting an extensive literature study, it is evident that various methods have been proposed for modelling the processes involved in jet trenching operations. These methods analyze the penetration depth of a single jet in cohesive soils, as well as studying settling velocities and sedimentation of soil particles. Accurately predicting cutting depth requires considering factors such as the forward velocity of the jet, soil properties, and jet settings. Experimental testing has been conducted to determine the optimal design of nozzles, jet pressure, and forward velocity required to achieve specific penetration depths. Mathematical models and empirical equations have also been explored to predict the cutting depth of a single jet in cohesive soils.

Furthermore, the study of settling velocities and sedimentation transport of soil particles has led to the development of methods for accurately calculating them. However, these methods depend on the flow pattern to which the soil particles are subjected. The flow behind a jet trenching machine is highly complex and requires further investigation through experiments or CFD. Although conducting a scale test in a water tank to observe the flow pattern behind a trenching machine would be ideal, building such a test setup and performing the necessary experiments is not feasible within the time-frame of this thesis. In this regard, CFD can serve as a valuable tool to accurately predict the flow pattern and sedimentation of soil particles. The CFD model proposed by Wang et al. (2021), while powerful, primarily focuses on soil failure mechanisms and requires substantial computational resources. For the purpose of this thesis, the primary focus will be on investigating the flow behind the trencher. Therefore, this thesis aims to develop a new CFD model that predicts the flow behind a trenching machine. By integrating the flow pattern with the existing jet trenching model (based on penetration depth), the model will incorporate sedimentation of soil particles, accounting for the lost depth due to sedimentation.

During the jet trenching process, the occurrence of clay blocks has been observed, but the precise process behind their formation remains poorly understood. The existing models used to predict the size of clay blocks have limitations and do not account for factors such as block breakage due to collisions with other jets or blocks stacking on top of each other. Accurate predictions of the actual size of clay blocks can only be obtained through experimental testing. Ideally, a laboratory-scale test setup, including a prepared clay and scaled jetting swords, could be utilized to establish a relationship between block size and jetting settings through multiple runs. However, constructing and conducting experiments with such a setup is beyond the scope of this thesis. Hence, an assumption regarding block size will be made to account for clay block formation.

In summary, this thesis will primarily focus on investigating the flow behind the jet trenching machine to accurately predict the flow pattern and sedimentation of soil particles. This research aims to enhance the existing models for jet penetration employed by DEME. By employing CFD, the study will simulate the flow behavior behind the trencher and develop a precise model for predicting soil particle sedimentation. The size of clay blocks will be assumed based on existing empirical equations or alternative assumptions.

6

Methodology

This chapter outlines the methodology adopted for the research, with a primary focus on two crucial aspects:

1. **Analysis of Flow Behavior:** The research employs CFD to simulate flow patterns and sedimentation of soil particles within the trench located behind the jetting swords. The primary objective is to acquire a comprehensive understanding of the flow characteristics in the trench.

2. **Lagrangian Model for Particle Motion:** The research incorporates the Verlet integration algorithm to model particle trajectories within the simulated flow field. This method involves updating particle positions and velocities at each time step, taking into account the evolving flow field. It provides valuable insights into the behavior of individual particles.

The research methodology emphasizes on numerical simulations, with CFD as a robust tool for predicting flow patterns and particle behavior. It ensures a thorough exploration of practical aspects while maintaining a strong theoretical foundation.

6.1. Computational Fluid Dynamics (CFD)

CFD is the utilization of computer-based simulations to analyze systems that involve fluid flow, heat transfer, and related phenomena. CFD is used in various engineering and scientific disciplines to simulate and analyze flow phenomena. It plays a crucial role in understanding, predicting, and optimizing fluid flow behaviors in a wide range of applications, such as aerospace, automotive design, marine engineering and environmental studies. CFD has changed the way engineers and scientists approach fluid dynamics problems, providing insights into complex flow patterns and allowing for the optimization of designs without the need for expensive and time-consuming physical experiments.

6.1.1. Governing Equations

The foundation of CFD lies in the mathematical description of fluid flow through a set of governing equations. These equations are based on fundamental principles and conservation laws, which provide a rigorous framework for modelling fluid behavior. In this section, the governing equations of fluid dynamics and the conservation laws that underpin them will be introduced.

Continuity Equation

The continuity equation, also known as the conservation of mass, represents the principle that mass is conserved within a fluid domain. It describes the rate of change of mass within a control volume:

$$\frac{\partial \rho}{\partial t} + \nabla \cdot (\rho \mathbf{u}) = 0 \tag{6.1}$$

where
ρ : Density of fluid [$\mathrm{kg\,m^{-3}}$]
t : Time [s]
∇ : Divergence operator [$\mathrm{m^{-1}}$]
$\mathbf{u}$: Fluid velocity vector [$\mathrm{m\,s^{-1}}$]

Navier-Stokes Equations

The Navier-Stokes equations are the cornerstone of fluid dynamics and describe the conservation of momentum within a fluid.They arise from applying Newton's second law to fluid motion. They consist of three separate equations, one for each dimension (x, y, z), and, for incompressible flow, can be written in vector form as follows:

$$\frac{\partial \mathbf{u}}{\partial t} + \nabla \cdot (\mathbf{u} \otimes \mathbf{u}) = -\frac{1}{\rho} \nabla p + \nabla \cdot \tau + \mathbf{f} \tag{6.2}$$

where
p : Fluid pressure [Pa]
τ : Stress tensor [Pa]
$\mathbf{f}$: External forces vector per unit volume [$\mathrm{N\,m^{-3}}$]

These equations govern the motion of the fluid and are responsible for describing phenomena such as fluid acceleration, pressure variations, and viscous effects.

6.1.2. CFD Operation

The effective utilization of CFD codes relies on a structured workflow and a clear understanding of its components. CFD codes are designed to tackle fluid flow problems through a systematic process encompassing three main elements: pre-processing, the solver, and post-processing. In this section, the functionality and significance of each of these elements within the context of a CFD code is discussed (Versteeg and Malalasekera, 2007).

Pre-processing

The pre-processing phase is the first step in setting up a CFD simulation. It involves the preparation of the input data that defines the problem to be solved. The pre-processing phase consists of the following steps:

1. **Geometry Definition:** The core of every CFD simulation is the definition of the computational domain's geometry. This domain represents the physical space in which fluid flow will be studied. The user specify the dimensions, shape, and boundaries of this domain, ensuring it accurately reflects the real-world scenario under investigation.

2. **Grid Generation:** Grid generation, also known as meshing, involves dividing the computational domain into smaller, discrete elements or cells. These cells create a grid or mesh that serves as the spatial discretization for the CFD simulation. The quality and density of the grid have a direct impact on the accuracy and computational time of the simulation. To accelerate computational processes, non-uniform grids are generated, allocating more cells to regions where flow variations are pronounced and fewer cells to areas where flow remains relatively constant.

3. **Phenomena Selection:** CFD simulations aim to model various physical and chemical phenomena that influence fluid flow. Users select the specific phenomena that are relevant to their problem. These may include turbulence, heat transfer, chemical reactions, and more, depending on the nature of the fluid flow.

4. **Boundary Conditions:** Boundary conditions are essential for defining how the fluid interacts with the domain's boundaries or specified regions within the computational domain. Properly specifying boundary conditions is crucial for achieving meaningful and accurate results. These conditions may involve defining the fluid's velocity, temperature, pressure, or other relevant properties at the domain boundaries.

The Solver
The solver is the component of a CFD code responsible for numerically solving the governing equations of fluid flow. Various solvers are accessible, each based on distinct algorithms. Typically, a solver involves three fundamental steps:

1. **Control Volume Integration:** The governing equations of fluid flow are integrated over all finite control volumes (cells in the grid) within the computational domain. This integration ensures the conservation of relevant properties, mass, momentum, and energy, within each control volume.

2. **Discretization:** The integral equations are discretized to transform them into a system of algebraic equations. This discretization step approximates derivatives and gradients, allowing the equations to be solved numerically.

3. **Solution of Algebraic Equations:** An iterative method is employed to solve the resulting system of algebraic equations. This iterative process aims to converge to a solution that satisfies the conservation equations and boundary conditions.

Post-processing
The post-processing phase is crucial for extracting meaningful insights from the numerical results obtained through the solver. Developments in post-processing capabilities have introduced data visualization tools within leading CFD packages. These tools include:

- Domain geometry and grid display.
- Vector plots illustrating flow directions and magnitudes.
- Contour plots with shading to represent scalar properties.
- Surface plots in 2D and 3D for visualizing results on geometry.
- Color-coded visualizations.

These visualization tools provide insight in complex fluid flow behavior. They facilitate the understanding of flow patterns, pressure distributions, temperature gradients, and other critical information. In addition to graphical outputs, CFD codes generate numerical results and data which can be exported for further analysis with external software.

6.2. Introducing openFOAM

The CFD simulations in this thesis will utilize openFOAM, short for Open-source Field Operation And Manipulation, an open-source C++ CFD software package. Developed by the openFOAM foundation in collaboration with a global community of users and developers, openFOAM has a strong presence in both academic and industrial CFD simulations. This section aims to provide an introduction to openFOAM, shedding light on its core attributes and, in particular, its solver framework.

6.2.1. Core Features

openFOAM offers features and functionalities that make it an attractive choice for CFD simulations. Some of its key attributes are:

- **Geometry and Mesh Handling:** openFOAM provides tools for defining geometries and generating meshes. These tools can be used to accurately represent complex domains and specify meshing requirements.
- **Solver Library:** openFOAM has an extensive solver library, facilitating a wide spectrum of fluid flow and heat transfer problems. These solvers were developed to address the Navier-Stokes equations, energy equations, and other equations governing fluid flow. The solver library consists of both steady-state and transient solvers. Different solvers are available for compressible and incompressible flows, multiphase flows and turbulent flow modelling.
- **Boundary Conditions:** openFOAM offers different boundary conditions to be specified for different scenarios. This flexibility enables the accurate modelling of various physical scenarios, including features such as no-slip walls, inflow/outflow conditions, and heat transfer boundaries.
- **Turbulence modelling:** openFOAM provides a package of turbulence models. This thesis will use the RANS model. The RANS (Reynolds-Averaged Navier-Stokes) turbulence model is used in fluid dynamics to predict the behavior of fluid flow. It simplifies the Navier-Stokes equations by averaging the effects of turbulence, which are otherwise very complex to solve for every point in space and time.
- **Parallel Computing:** openFOAM allows for parallel computing, which distributes the computational workload across multiple processor cores, resulting in reduced computation time.

6.2.2. Solvers

As previously mentioned, openFOAM provides an extensive library of solvers for a wide range of simulation scenarios. These solvers can typically be categorized into five distinct categories, each designed to address specific fluid dynamics and CFD challenges and needs.

- Incompressible flow solvers
- Compressible flow solvers
- Multi-phase flow solvers
- Turbulent flow solvers
- Heat transfer solvers

For this thesis, the flow behind the jetting swords in the trench is modeled. This is considered an incompressible flow regime, which is appropriate for substances like water due to their nearly incompressible nature. Additionally, the flow is turbulent, primarily due to the high Reynolds number. To address this modelling scenario, an incompressible turbulent solver that seeks the steady-state solution is selected. A steady-state solver is chosen because it aligns with the ultimate objective of this study.

One of the solvers commonly employed for such purposes within the openFOAM framework is simpleFOAM. simpleFOAM is an iterative solver used for simulating steady-state, incompressible, and turbulent flow problems. It operates based on the finite volume method, which discretizes the governing equations for fluid flow and turbulence using a control volume approach.

The SIMPLE (Semi-Implicit Method for Pressure Linked Equations) algorithm is a widely-used numerical method for solving incompressible flow equations. It was originally introduced by Caretto et al. (2007) and has since become a fundamental tool in CFD. The method is designed for steady-state, incompressible, turbulent flow simulations and is utilized in solvers like simpleFOAM. This is a summary of the characteristics and procedures for this solver:

simpleFOAM Solver:
Overview:

- **Category:** Incompressible
- **Flow Regime:** Steady State
- **Key Features:** Incompressible, Turbulence modelling (RANS)
- **Finite Volume Method:** Yes

Equations Solved:

As discussed in section 6.1.1, equation 6.1 and 6.2 are solved with the simpleFOAM solver.

Solver Sequence for Each Iteration:

1. Advance to the next iteration $t_{n+1} = t_n + \Delta t$.
2. Initialize $\mathbf{u}_{n+1}$ and p_{n+1} using the latest available values of $\mathbf{u}$ and p.
3. Construct the momentum equations.
4. Under-relax the momentum matrix.

   Under-relaxation is a technique used in iterative solvers to dampen the effect of each iteration's update on the solution.
5. Solve the momentum equations to obtain a prediction for $\mathbf{u}_{n+1}$.
6. Construct the pressure equation.
7. Solve the pressure equation for p_{n+1}.
8. Correct the flux for ϕ_{n+1}.

   This step involves adjusting any fluxes or quantities (represented by ϕ) to ensure consistency with the newly computed pressure field p_{n+1}.
9. Under-relax p_{n+1}.

   Similar to step 4, this involves applying under-relaxation to the newly computed pressure field before using it in subsequent iterations.
10. Correct the velocity for $\mathbf{u}_{n+1}$.
11. If not converged, go back to step 2.

Input Requirements:

- Mandatory Fields:
  - p: Kinematic pressure [m²/s²]
  - U: Velocity [m/s]

simpleFOAM is the preferred solver for this study because it aligns with the study's specific needs. It is widely used and well-documented, making it relatively easy to work with. Additionally, it excels at handling steady-state, incompressible, and turbulent flow simulations, which are crucial for the study's objectives. Its flexibility also allows for customization to match the unique characteristics of the trench and jetting sword configuration. In summary, simpleFOAM is the ideal choice to ensure the accuracy and success of this research.

6.3. Simulation Setup and Boundary Conditions

In this section, an overview of the CFD simulation setup for this thesis is provided, focusing on the geometry, critical boundary conditions and initial conditions. Key steps, such as domain definition and mesh generation are outlined. Special attention is given to the selection and setup of boundary conditions, including considerations for no-slip walls and inflow/outflow.

6.3.1. Geometry Definition

As mentioned in section 6.1.2, the first step during the pre-processing phase is to define the geometry, which will be the domain in which the fluid will flow. In the case of this study, this domain represents a trench situated behind two jetting swords, which are placed at a specific distance apart from each other. To achieve this, the 3D modelling software Blender is used to create a geometry that represents the trench behind a jet trenching machine. The depth of the trench is specific to the type of jetting swords being used, and the width is project-specific (in this thesis, a width of 0.5 m is used, figure 6.1b).

For modelling the trench, a rectangular shape is assumed in traverse direction. The jetting swords are inclined at an angle of 60 degrees (as illustrated in Figure 2.3) relative to the horizontal. To replicate this configuration, the trench is modeled accordingly, as shown in Figure 6.1a. On the right side, the trench is inclined at an angle of 60 degrees, following the orientation of the jetting swords.

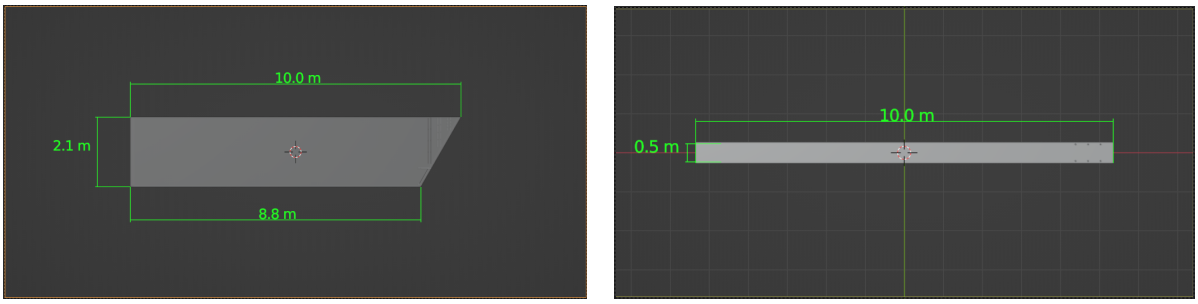

(a) Side view

(b) Top view

Figure 6.1: 3D geometry of trench behind the 2.1 [m] jetting swords

A notable aspect of this study is the modelling of the nozzles on the swords. Rather than individually modelling each nozzle, which would consume considerable computational resources, a more efficient approach is adopted. The inward and downward facing nozzles are grouped into groups which represent a certain number of nozzles. Each group is represented by one equivalent nozzle using the principle of conservation of mass. While the downward and inward-facing nozzles are grouped and collectively represented by less nozzles, the backward-nozzles are modeled individually since there are only two per jetting sword. This grouping is achieved by considering the conservation of mass, which efficiently capture the behavior of the jetting nozzles.

To model multiple individual nozzles as one equivalent nozzle using the conservation of mass, a systematic approach is employed to find the diameter of the equivalent nozzle:

1. **Mass flux:**

$$P = \rho * A * u \tag{6.3}$$

where P : Mass flux of the fluid stream [$\mathrm{kg\,s^{-1}}$]
A : Cross-sectional area of the nozzle [$\mathrm{m^2}$]
u : Flow velocity at the exit of the nozzle [$\mathrm{m\,s^{-1}}$]

2. **Total mass flux for m individual nozzles (with equal diameter and flow velocity)**

$$\sum_{i=1}^{m} P_i = \rho * u * \sum_{i=1}^{m} A_i \tag{6.4}$$

3. **Mass flux of equivalent nozzle**

$$P_{equiv} = \rho * A_{equiv} * V \tag{6.5}$$

4. **Conservation of mass**

$$\sum_{i=1}^{m} P_i = P_{equiv} \tag{6.6}$$

$$A_{equiv} = \sum_{i=1}^{m} A_i \tag{6.7}$$

$$\frac{1}{4}\pi D_{equiv}^2 = \frac{1}{4}\pi \sum_{i=1}^{m} D_i^2 \tag{6.8}$$

$$D_{equiv} = \sqrt{\sum_{i=1}^{m} D_i^2} \tag{6.9}$$

where A_{equiv} : Cross-sectional area of the equivalent nozzle [$\mathrm{m^2}$]
D_{equiv} : Nozzle diameter of equivalent nozzle [m]
D_i : Nozzle diameter of multiple modeled nozzles [m]

With the equivalent diameter (D_{equiv}), the combined flow from all the nozzles can be modeled as if it were a single nozzle, simplifying the analysis while conserving mass. This approach assumes that the interactions between individual nozzles are minimal and that flow conditions are consistent across all the nozzles, reducing computational complexity. The sum of the areas of each individual nozzle is not the same as the area of the equivalent nozzle. Therefore, there will be a difference in entrainment. The effect of entrainment is neglected in this assumption.

Using the principle of conservation of momentum, a geometry for the nozzles has been created inside the trench (See figure 6.2a and 6.2b), serving as the foundation for the subsequent CFD simulations, these nozzles will be the inlet of the model. The total geometry represents the trench behind the jetting swords and provides the basis for studying the flow dynamics. This study considers two types of jetting swords, one with a depth of 2.1 meters (shown in the figures) and the other with a depth of 1.5 meters (constructed in the same manner see appendix B). The length of the trench is set at 10 meters as shown in figure 6.1a. By this distance from the jetting swords, the flow has reached a state of near uniformity, and particles of interest have reached the bottom of the trench. This aligns with the primary focus of this study.

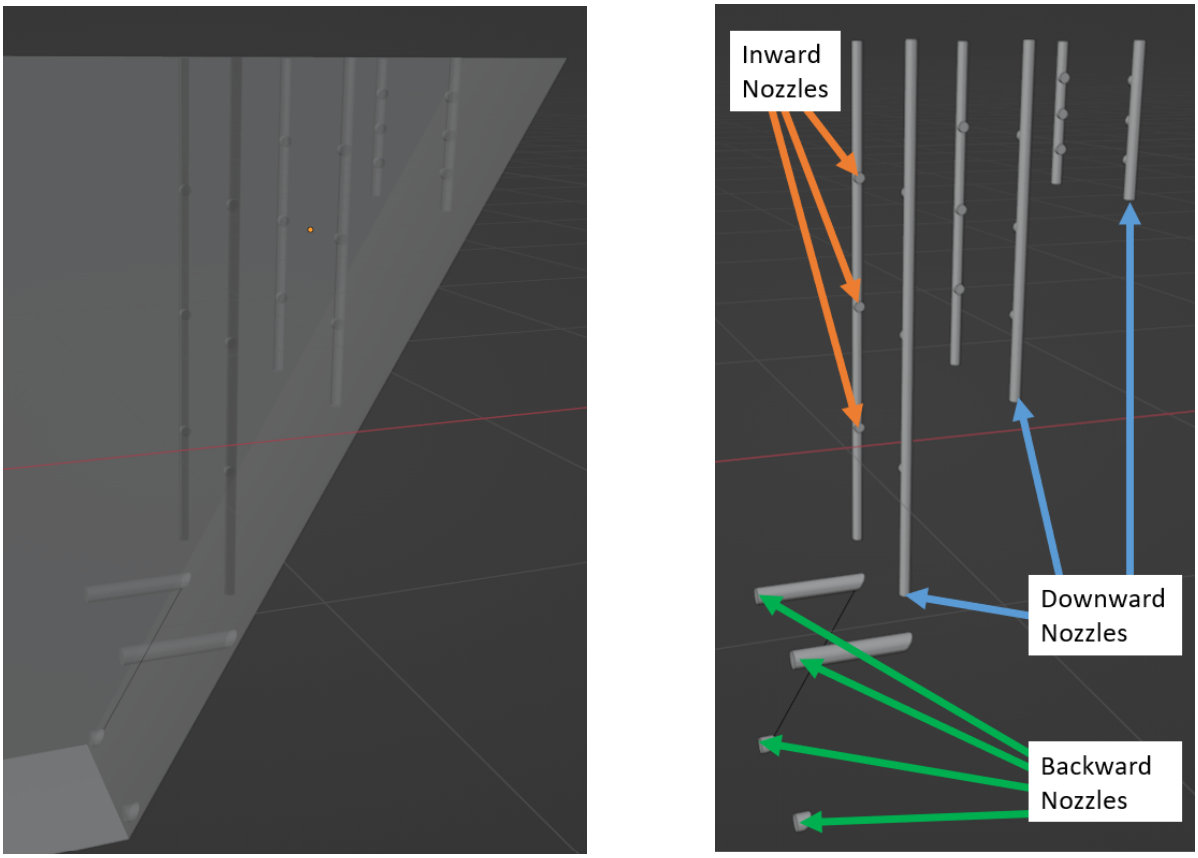

(a) Overview

(b) Configuration

Figure 6.2: 3D geometry of nozzles inside the 2.1 [m] trench

6.3.2. Boundary Conditions

This section will be dedicated to the boundary conditions which were set for the this study. Boundary conditions are an critical aspect of any CFD simulation. Boundary conditions define how the fluid interacts with the domain's boundaries, playing a important role in determining the behavior of the fluid within the simulation. The geometry, representing the trench behind two jetting swords, consists of three distinct types of boundaries: **inlet**, **outlet**, and **wall**. In this case, the nozzles shown in figure 6.2b are the inlet. In figure 6.1a and 6.1b, the top and back in figure of the trench are the outlet and the sides and bottom of the trench are specified as wall. Each boundary type is associated with specific boundary conditions for pressure (p) and flow velocity (U), specified to accurately model the flow dynamics in our particular case.

1. **Inlet Boundary:** At the inlet boundary, where fluid enters the domain, it is crucial to prescribe appropriate conditions to represent the fluid's characteristics accurately. For pressure (p), a '`zeroGradient`' condition is applied. This choice ensures that there is no abrupt change in pressure at the inlet, aligning with the assumption of a smooth and continuous flow entry. For velocity (U), a '`fixedValue`' condition is employed. This means that the velocity values at the inlet are specified based on the problem's requirements. The '`fixedValue`' condition allows to control and define the inflow velocity profile, which is important to accurately capture the behavior of fluid entering the trench.

2. **Outlet Boundary:** The outlet boundary represents the region where fluid exits the domain. Here, it is essential to consider the impact of the flow as it leaves the simulation. For pressure (p), a '`zeroGradient`' condition would not be appropriate as it would imply that the pressure at the outlet is identical to the pressure within the domain, which is not generally the case. Instead, a '`fixedValue`' condition is applied, where the pressure is set to a specified constant value (in this case, zero). This choice implies that the velocity gradients are small at the domain boundaries and the pressure obtains the same value as the hydrostatic pressure at that point. For velocity (U), an '`inletOutlet`' condition is used. This

condition allows for both inflow and outflow at the outlet boundary. It accounts for the possibility of fluid either entering or leaving the domain at the outlet, depending on the local flow conditions.

3. **Wall Boundary:** The wall boundaries correspond to the surfaces of the trench and the nozzles, where the fluid interacts with solid boundaries. For pressure (p), a 'zeroGradient' condition is employed. This choice ensures that the pressure gradient across the wall is minimal, assuming a negligible pressure difference across the boundary, which is often valid for solid walls.

   For velocity (u), a 'noSlip' condition is applied, assuming that the fluid adheres to and does not slip along the solid surfaces. However, to properly account for turbulence effects near the wall, wall functions are employed. These functions model the behavior of the turbulent boundary layer close to the wall and adjust the near-wall velocity values accordingly.

   Additionally, the dimensionless wall distance (y^+) is evaluated to ensure that the mesh resolution near the wall is sufficient to accurately capture the flow physics. The y^+ value indicates whether the flow is in the viscous sublayer, the buffer layer, or the fully turbulent region. Properly resolving y^+ is essential for accurate turbulence modelling and reliable predictions of flow properties near solid boundaries, such as the trench walls and nozzles.

6.3.3. Mesh Generation

The accuracy and reliability of CFD simulations heavily depend on the quality and suitability of the mesh used to discretize the computational domain. In this study, 'snappyHexMesh' is employed, a powerful mesh generation tool within the openFOAM framework, to create a mesh that accurately represents the complex geometry of the trench behind the jetting swords. Meshing of the geometry involves the following steps:

1. **Preparing the Geometry:** Before initiating the mesh generation process, it is essential to ensure that the geometry is well-prepared. As discussed in section 6.3.1, the geometry represents the trench and the nozzles on the jetting sword. This geometry is the foundation for the mesh generation efforts. The geometry preparation involves checking for geometric errors, ensuring watertightness, and converting it to a format that 'snappyHexMesh can readily work with. The chosen geometry format is STL (stereolithography) and should accurately represent the boundaries and features of the domain.

2. **Setting up Meshing Parameters:** Meshing parameters play a critical role in determining the mesh density, refinement levels, and overall mesh quality. The choice of mesh parameters should align with the objectives of the CFD simulation and the complexity of the geometry. In this, parameters such as the target mesh size, refinement levels near critical regions (e.g., jetting sword nozzles), and boundary layer settings are specified to capture the boundary behavior accurately. The goal is to achieve a mesh that is both fine enough to resolve the flow details and efficient enough to minimize computational resources.

3. **Running 'snappyHexMesh:** Once the geometry is prepared, and meshing parameters are set, 'snappyHexMesh' can run to create the mesh. It employs a multi-stage process to generate the mesh:

   - **Creating background mesh** First a background mesh of hexahedral cells will be generated using 'blockMesh'
   - **Cell splitting at feature edges and surfaces:** Cell splitting is applied according to the refinement level. This means more cells will be created close to the surface of the geometry as well as other regions specified by the user.
   - **Cell removal:** 'snappyHexMesh' proceeds by removing the cells within the space of the geometry. To create a domain which represents the geometry.

Using these steps, a mesh has been generated based on the geometry defined in section 6.3.1. The resulting mesh will serve as the foundation for the upcoming CFD simulation. In Figure 6.3, you can observe the mesh created by 'snappyHexMesh' in accordance with the geometry.

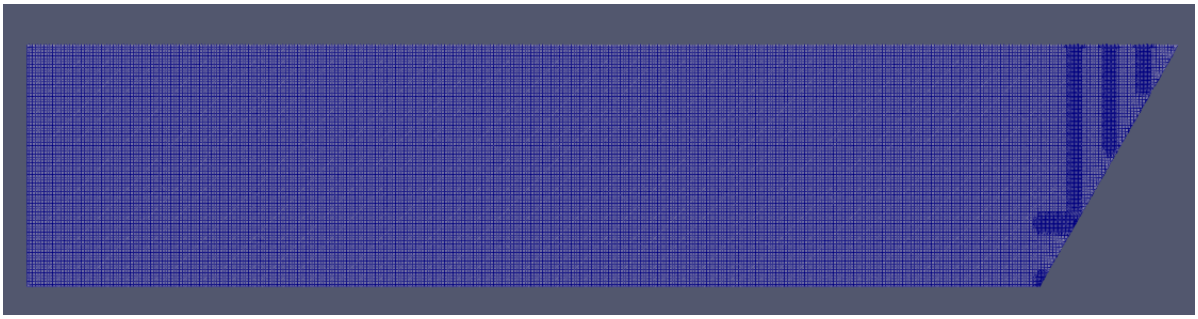

Figure 6.3: Sideview of the mesh 2.1 [m] trench

Further away from the nozzles and deeper into the trench, where the flow is expected to be more stable, a lower cell density is applied. This refined meshing strategy optimizes the utilization of computational resources and significantly reduces computation time. In essence, it allows allows for allocating computational power efficiently to areas where it is most needed, ensuring the simulation's accuracy without unnecessary computation time.

To ensure the reliability of the simulation results, several mesh refinement strategies were implemented. One such strategy involves maintaining a maximum refinement ratio, ensuring that adjacent cells do not differ in size by more than a certain percentage, typically 10% for RANS simulations.

By systematically varying the mesh parameters and observing the resulting changes in the simulation output, it was verified that the solution remains consistent and convergent across the mesh configurations as shown in figure 6.4a and 6.4b.

The showcased mesh corresponds to the geometry of a 2.1-meter jetting sword, and this refined meshing strategy has also been applied to the 1.5-meter jetting sword geometry.

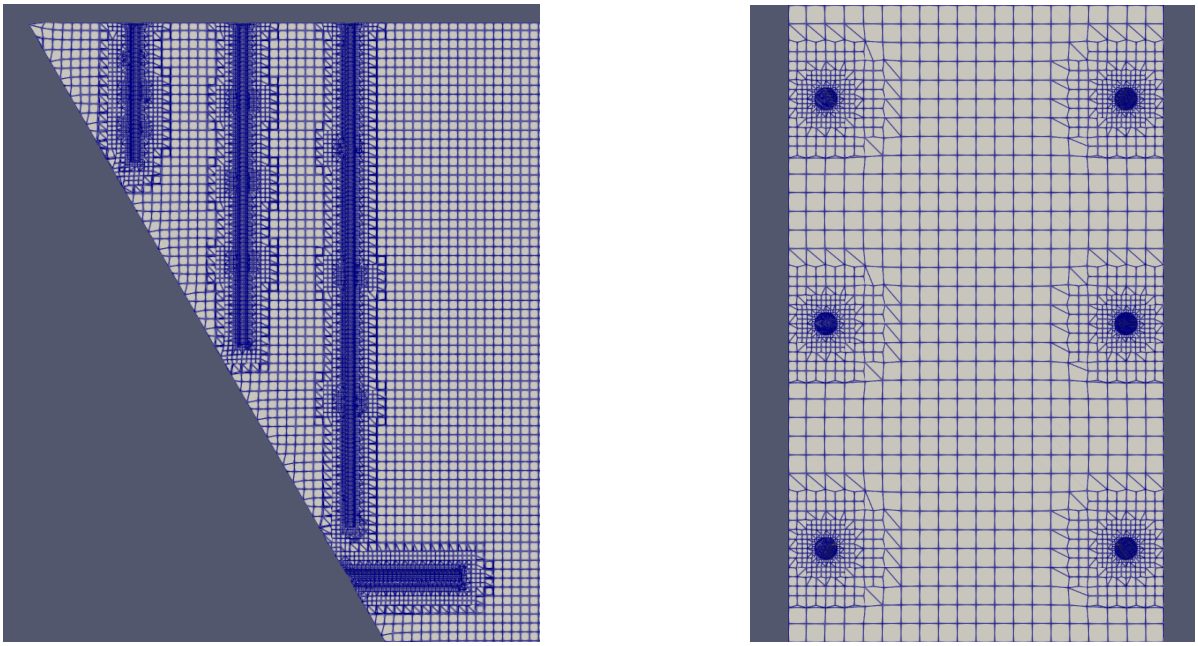

(a) Side view

(b) Top view

Figure 6.4: Refinement of the mesh close to the nozzles 2.1 [m] trench

6.3.4. Pump Pressure and Flow Velocity

The initial conditions for the CFD simulation in this thesis consists of specifying the flow velocity at the exit of the nozzles. The flow velocity is a key parameter that plays a fundamental role in determining the behavior of fluid flow within the trench behind the jetting swords. In this case, the flow velocity is determined by the pump pressure inside the jetting swords using the dynamic pressure equation:

$$q = \frac{1}{2}\rho u^2 \tag{6.10}$$

where q : Dynamic pressure [Pa]
ρ : Fluid density [$\mathrm{kg\,m^{-3}}$]
u : Flow velocity [$\mathrm{m\,s^{-1}}$]

When the pump pressure P is used as the dynamic pressure, the flow velocity can be calculated by:

$$u = \sqrt{\frac{2P}{\rho}} \tag{6.11}$$

where P : Pump pressure [Pa]

In practice, determining the pressure within the jetting swords is not a straightforward task, as it depends on various factors such as the characteristics of the pump system, the fluid properties, and the configuration of the nozzles. In this study, the pressure within the jetting swords is derived from a specific working point of the pump system.

A "pump working point" refers to a specific operating condition of a pump system, where flow rate and pressure are established. It is the point where the pump curve and the flow "demand" of the system meet and the pump power is used most efficiently. This working point is a crucial reference for pump design and operation. In the context of this study, it serves as the basis for defining the initial conditions for the CFD simulation.

DEME uses the expected pump working point based on nozzle count and diameter. The optimal working point is determined by finding the intersect between the pump curve (prescribed by the manufacturer) and the nozzle demand. For instance, a sword with 30 nozzles of 13.5 mm diameter, the ideal working point is illustrated in Figure 6.5. In this study, CFD simulations will be executed with various nozzle configurations, each with different working points, to explore a range of scenarios.

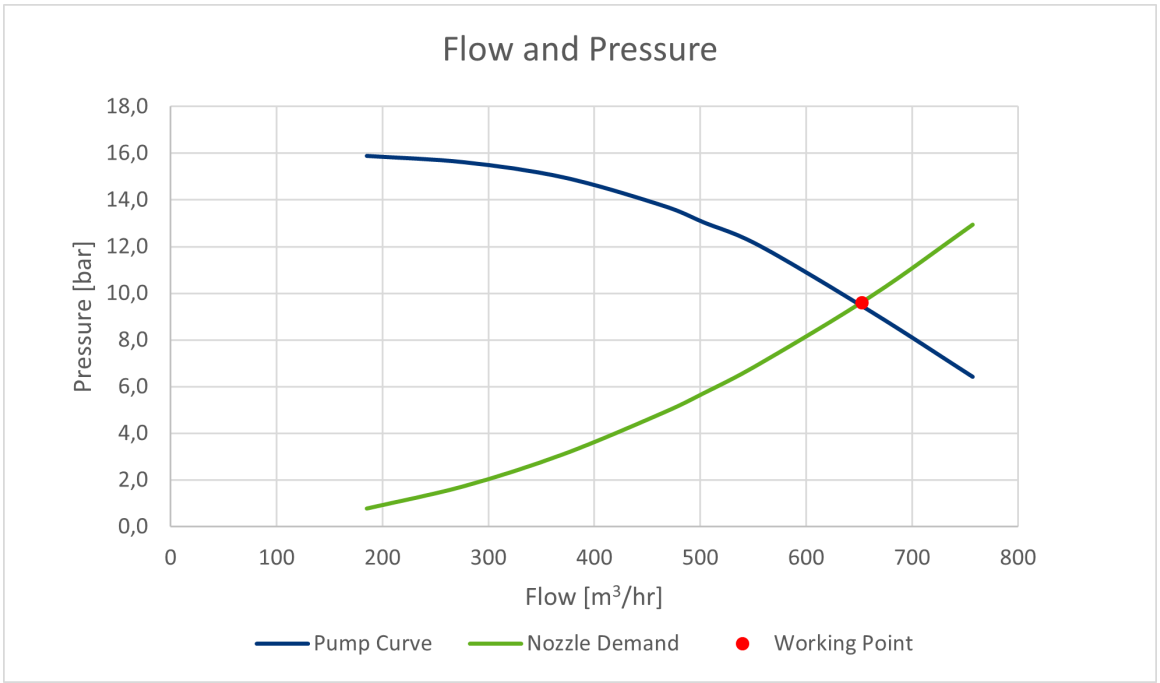

Figure 6.5: Pump working point (DEME, 2021)

6.4. Simulation of Particle Motion

By running the `simpleFOAM` solver from `openFOAM`, within the specified domain, a flow field will be generated describing the flow dynamics in the trench. The next crucial step is to analyze and predict the trajectory of a particle as it moves within this flow field. To accomplish this task, the Verlet integration algorithm is employed. In this section, the details of the Verlet integration method and its application in modelling the motion of particles within the established flow field will be explored.

6.4.1. Verlet Integration

The Verlet integration (Verlet, 1967) is a numerical integration method commonly used in physics and computational science to solve ordinary differential equations (ODEs) that describe the motion of particles or objects under the influence of forces (Newton's second law). It is known for its stability, accuracy, and ability to conserve physical quantities like energy and momentum.

The core concept of the Verlet integration method lies in updating both the position ($\mathbf{r}$) and velocity ($\mathbf{v}$) of a particle at the same time, making it particularly suitable for simulating the dynamics of particles in a changing environment. The method involves two main steps: predicting the new position and velocity and then correcting them based on the computed acceleration.

The Verlet algorithm can be mathematically expressed as follows:

$$\mathbf{r}(t+\Delta t) = \mathbf{r}(t) + \mathbf{v}(t)\Delta t + \frac{1}{2}\mathbf{a}(t)\Delta t^2 \tag{6.12}$$

$$\mathbf{v}(t+\Delta t) = \mathbf{v}(t) + \mathbf{a}(t)\Delta t \tag{6.13}$$

where

$\mathbf{r}$	:	x-y-Coordinates of the particle at time t	[m]
$\mathbf{v}(t)$	:	Velocity vector at time t	[m s^{-1}]
$\mathbf{a}(t)$	:	Acceleration vector at time t	[m s^{-2}]
Δt	:	Time step	[s]

6.4.2. Application of Verlet Integration

To model the trajectory of a particle within the generated flow field, the Verlet integration method is applied as follows:

1. Set the initial position (x_0, y_0) and velocity (u_0, v_0) of the particle at a specific location within the flow field.
2. Iterate through time steps (Δt) until a specified termination condition is met (e.g., when the particle exits the simulation domain).
3. At each time step:
   (a) Interpolate the local fluid velocity at the current position of the particle to obtain the velocity ($\mathbf{u}$) of the flow field at that point.
   (b) Calculate the relative velocity vector ($\mathbf{V}_{\text{rel}}$) between the particle and the local fluid using the interpolated velocity and the particle's current velocity.
   (c) Compute the acceleration vector ($\mathbf{a}$) acting on the particle, which includes the effects of drag force and gravity.
   (d) Update the position and velocity of the particle using the Verlet integration.
   (e) Record the new position to track the trajectory of the particle.

This iterative process continues until the termination condition is satisfied. Throughout the simulation, the velocity Verlet integration method ensures accurate modelling of the particle's motion by considering the changing flow field and its effects on the particle.

In summary, the `CFD` simulation generates a flow field that determines the motion of a particle, and the Verlet integration method is employed to model the particle's trajectory by updating its position and velocity at each time step. This approach provides insights into the behavior of particles within the flow field in the trench.

6.5. Simulation of Particle Motion at the Bottom of the Trench

The Verlet integration method focuses on simulating particle trajectories within the computational domain, in this study specifically tracking particles until they reach the trench bottom. To account for particle movement on the bottom of the trench, Shields criterion and its application will be introduced. This criterion helps determine whether particles at the trench bottom will remain static or initiate motion.

6.5.1. Shields Parameter

The Shields parameter (Shields, 1936) is a dimensionless quantity used in the field of sediment transport. It plays a fundamental role in determining when sediment particles will initiate motion in response to the shear forces exerted by flowing water. The Shields parameter, denoted as θ , quantifies the balance between the driving forces of fluid flow and the resisting forces of sediment particles.

Shields parameter is a dimensionless parameter defined as follows:

$$\theta = \frac{\tau}{(\rho_s - \rho) g d} \tag{6.14}$$

where
θ	:	Shields parameter	[−]
τ	:	Shear stress	[Pa]
ρ_s	:	Particle density	[kg m^{-3}]
ρ	:	Fluid density	[kg m^{-3}]
g	:	Gravitational acceleration	[m s^{-2}]
d	:	Particle diameter	[m]

Shields (1936) conducted a comprehensive series of experiments, comparing various sediment types and flow conditions. From his research, he derived the Shields diagram, a fundamental tool in sediment transport studies. This diagram shows a critical Shields parameter value, beyond which sediment motion occurs, and below which it does not. Multiple versions of this diagram have been developed by subsequent researchers. For this study, a Shields diagram is employed, featuring the critical Shields parameter as a function of the particle diameter as shown in figure 6.6.

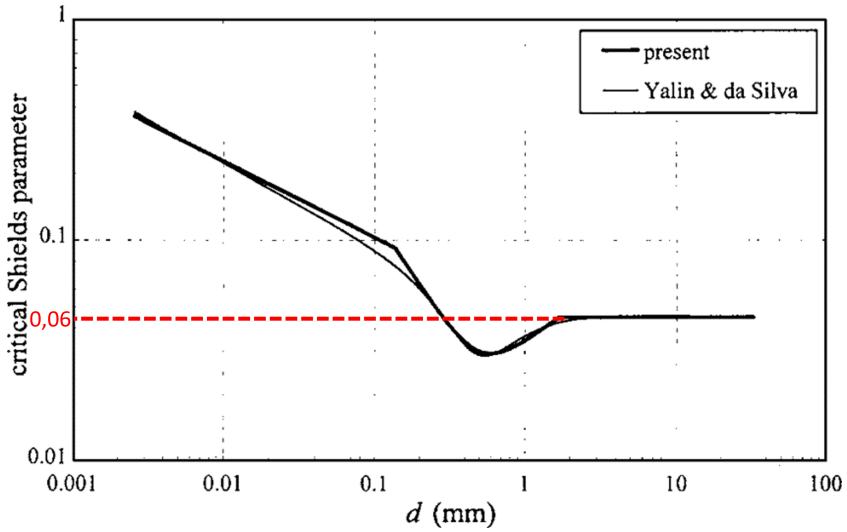

Figure 6.6: Critical shields parameter as a function of particle diameter (Cao et al., 2006)

From Figure 6.6, it becomes evident that the critical Shields parameter attains stability when considering particles with a diameter exceeding 1-2 mm, settling consistently at approximately 0.06. As discussed in Section 4.3, clay block formations are typically much larger than 1-2 mm. In fact, the scope of this study specifically investigates particles ranging from 20 to 100 mm in size. Therefore, to effectively model sediment dynamics within this context, a critical Shields parameter value of 0.06 will be employed, aligning with Shields diagram.

6.5.2. Simulation of the Particle Motion

This section elaborates how Shields parameter is incorporated in the model to account for the movement at the bottom of the trench. To do accomplish this, the following steps will be part of the model:

1. **Verler integration:** The Verlet integration method is used to track particle trajectories until they reach the bottom of the trench. This method ensures a comprehensive representation of particle motion within the computational domain.

2. **Shear stress determination:** When particles reach the bottom of the trench, `openFOAM` is employed to calculate the shear stress exerted by the flowing fluid at this boundary. This calculation considers local flow conditions, fluid properties, and trench geometry, providing essential data for further analysis.

3. **Shields Parameter Calculation:** With the shear stress known, equation 6.14 is used to calculate the local shields parameter at the cell where the particle reaches the bottom of the trench.

4. **Particle Movement Assessment:** Shields parameter is evaluated. If it exceeds the critical Shields value, particles proceed to the next computational cell, simulating their trench floor transport.

5. **Termination Criteria:** The process continues until the Shields parameter falls below the critical threshold, indicating insufficient shear stress to overcome sediment resistance. At this point, particle motion stops, concluding the simulation.

While Shields criterion may not be a direct match for the specific problem under investigation, it serves as a valuable indicator of particle behavior at the trench bottom. This criterion offers insights into whether sediment particles are likely to remain stationary or initiate movement on the trench floor. The critical Shields parameter of 0.06, derived from empirical observations, provides a meaningful reference point.

7

Simulation Results and Analysis

In this chapter, the simulation results of the CFD model, as well as their analysis, are presented and discussed. The integration of CFD simulations has enabled a comprehensive exploration of trenching dynamics, providing valuable insights into the behavior of particles and fluid flow during the trenching process.

The chapter begins with an overview of the simulation setup and parameters used in the CFD model. This includes details such as boundary conditions, fluid properties, and initial particle distributions. Following this, the main results of the simulations are presented, focusing on key findings.

The analysis section delves into the interpretation of the simulation results, examining the influence of various factors such as particle diameter, trench profile, and flow conditions on the outcomes.

Additionally, this chapter discusses the trench profile expected at the end of the simulations, highlighting variations in the depth and shape of the trench. Furthermore, the depth of burial of the cable within the trench is addressed.

7.1. Initial Conditions

In this study, two types of initial conditions are essential. First, the flow velocity at the inlet of the domain, crucial for the CFD simulation in openFOAM, is described. Next, the initial position and size (diameter) of the particles used in the Verlet integration method are outlined. These conditions are vital to determine the particle movement within the trench behind the jetting sword.

7.1.1. Initial Conditions Simulation

As discussed in section 6.3.2, the only initial parameter for the openFOAM simulation is the flow velocity (U) at the inlet of the computational domain. This flow velocity plays a key role in modelling the behavior of the fluid within the trench. To determine the appropriate value for the '`fixedValue`' of U at the inlet, a comprehensive approach is employed.

First, as detailed in section 6.3.1, the grouping of nozzles is considered. This grouping accounts for the fact that modelling each individual nozzle would place a considerable computational burden on the simulation. Instead, the inward and downward-facing nozzles are grouped, and an equivalent nozzle is used to represent each group. This grouping is based on the conservation of mass, efficiently capturing the behavior of the jetting nozzles. The inward nozzles are inclined downwards by 20°, which is specified by DEME.

Next, the pump working point, as described in section 6.3.4, serves as a reference for determining the flow velocity. The pump working point defines the specific operating conditions of the pump system, where the pump pressure is established most efficiently. This point is fundamental to pump design and operation. In this study, the pump pressure inside the jetting swords is determined based on this working point.

A range of scenarios is considered. Two different types of jetting swords are distinguished, both commonly used by DEME. Type 1 has a depth of 1.5 meters, while type 2 has a depth of 2.1 meters. Correspondingly, type 1 is equipped with 13 inward nozzles, 16 downward nozzles, and 2 backward nozzles on each sword, while type 2 features 13 inward nozzles, 22 downward nozzles, and 2 backward nozzles on each sword. The pump pressure for the inward and downward nozzles is set according to the pump working point, as shown in table 7.1. The diameter and pressure for the backward nozzles are fixed to 60 mm and 2 bar as specified by DEME.

For each type of jetting sword, two scenarios are considered, differentiating by nozzle diameter. One scenario employs a nozzle diameter of 10 mm, while the other utilizes a diameter of 13.5 mm. The diameter of the backward nozzles remains consistent at 60 mm for all scenarios. This results in a total of four distinct scenarios, each with unique parameters that influence the flow field.

To calculate the flow velocity for each of these scenarios, equation 6.11, with the pump working point and the given parameters, will be utilized. The flow velocity values will be determined subsequently based on the specific characteristics of each scenario.

To provide a clear overview of these scenarios, the following table outlines the key parameters for each scenario, where the flow velocity values are those for the inward an downward nozzles:

Scenario	Jetting Sword Type	Nozzle Diameter [mm]	Pump Pressure [bar]	Inlet Flow Velocity [m/s]
1	Type 1 (1.5m depth)	10	14.3	52.8
2	Type 1 (1.5m depth)	13.5	9.9	44.0
3	Type 2 (2.1m depth)	10	13.3	50.9
4	Type 2 (2.1m depth)	13.5	8.2	40.0

Table 7.1: Jet setting scenarios

These scenarios cover a spectrum of conditions which are commonly used by DEME. Enabling a comprehensive investigation of the flow field in the trench behind the jetting sword. Comparing these different scenarios is essential for drawing conclusive findings at the study's conclusion.

7.1.2. Initial Conditions Particle Trajectory Integration

Two initial conditions govern the Verlet integration method's particle tracking process. The first one is the starting point within the computational domain where the Verlet integration begins. To facilitate a comprehensive analysis, various scenarios have been defined in section 7.1.1. For each scenario, two lines parallel to the inclination of the jetting swords (as shown in Figure 7.1) are used for the Verlet integration method. The figure is a representation of the trench geometry as defined in section 6.3.1. The figure shows the trench profile for a type 2 (2.1m depth) jetting sword, the same principle has been applied to the type 1 (1.5m depth) jetting sword. On each line, ten equally spaced points are selected as the initial positions. Consequently, multiple particles are released from different locations, allowing to compare the final destination at the bottom of the trench for each particle.

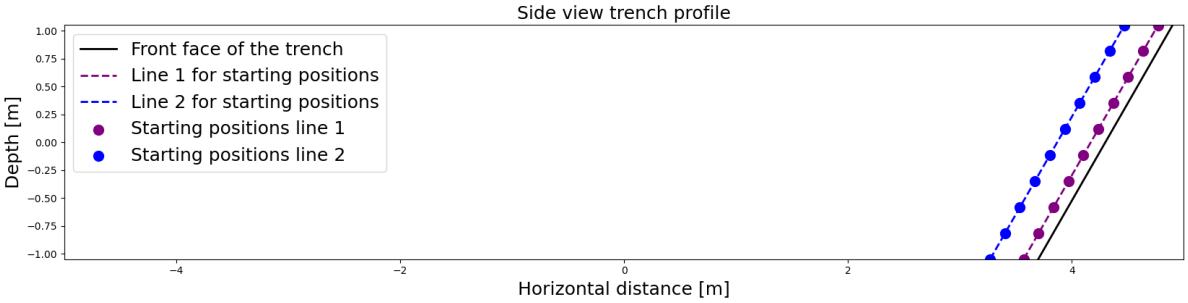

Figure 7.1: Side view of trench profile with starting position lines

The second initial condition is the dimension of the particles, specifically their diameter. Assuming spherical particles, the diameter becomes a critical parameter which influences the forces acting on the particle (gravity and drag). In this research, a range of particle diameters have been selected between 10 mm and 100 mm. These dimensions align with anticipated clay block sizes, as discussed in section 4.3. However, it's important to note that the precise dimensions of clay blocks remain relatively unknown, making these assumptions a practical starting point for the study.

By manipulating both the starting positions and particle diameters, this research covers a broad range of conditions. The combination of diverse starting points and particle sizes enables valuable insights into how these initial parameters affect the trajectories and final positions of the particles within the trench behind the jetting sword. This approach ensures a thorough examination of the complex dynamics in the trench, leading to a more comprehensive understanding of particle behavior in the real-world scenarios under investigation.

7.2. Simulation Results

In this section, the results of the `openFOAM` simulations are presented, providing a detailed perspective on fluid dynamics within the trench behind the jetting swords. The data obtained includes information about flow patterns, velocities, and pressures within the computational domain. These results serve as a foundation for further analysis of particle trajectories and sedimentation behaviors.

7.2.1. Running `openFOAM` simulation

In this section, the process of executing an `openFOAM` simulation on a Linux Ubuntu virtual machine is explained, with additional details about how `simpleFoam` determines the attainment of a steady-state solution.

Prior to running the simulation, a crucial file known as `controlDict` is prepared. This file governs the temporal aspects of the simulation and includes several key parameters:

1. **Starting Time (`startTime`):** The simulation commences at time zero (0 seconds), marking the initial state.
2. **End Time (`endTime`):** The simulation concludes at the specified endpoint, typically set to 20 seconds in this study.
3. **Time Step (`deltaT`):** Time integration relies on this parameter, determining the size of each time step. In this context, `deltaT` is generally set to 0.005 seconds.

4. **Write Interval (`writeInterval`):** `WriteInterval` is a critical parameter that dictates how frequently the solver records values of various simulation parameters into output files. For instance, if `writeInterval` is set to 100, the solver captures data every 100 time steps, offering periodic snapshots of the simulation's progress. The choice of `writeInterval` significantly influences data granularity and storage requirements.

With these settings established within the `controlDict` file, the simulation process begins. The chosen solver, `simpleFoam`, seeks a steady-state solution over time. To determine if a steady-state solution has been reached, `simpleFoam` employs tolerance values:

U Tolerance (`UTolerance`): This parameter is set to 1×10^{-5}, signifying that the solver considers the velocity field (`U`) as converged to a steady state when the changes in velocity between consecutive time steps fall below this tolerance. In simpler terms, it reflects the allowable deviation in velocity as the simulation progresses.

p Tolerance (`pTolerance`): For pressure (`p`), the tolerance (`pTolerance`) is set to 1×10^{-6}. This means that the solver regards the pressure field as converged when the differences in pressure values between time steps are smaller than this tolerance.

When both the velocity and pressure fields meet these defined tolerance criteria, `simpleFoam` concludes that a steady-state solution has been attained and terminates the simulation.

Notably, for all scenarios investigated in this study, `simpleFoam` successfully converged to a steady-state solution within a time range of 6 to 12 seconds.

Following the simulation, a comprehensive dataset is collected, comprising parameter values at every time interval and for every cell as determined in section 6.3.1. This data serves as the foundation for the subsequent analysis of fluid dynamics within the trench behind the jetting swords. These results are essential for understanding particle trajectory behavior, a central focus of this study.

7.2.2. Visualising Results

The visualization of `CFD` simulation outcomes is an important step to understand complex fluid behaviors. In this subsection, the utilization of ParaView, a robust visualization tool, to analyze and interpret the results obtained from the preceding `openFOAM` simulations is explored. ParaView offers a diverse array of visualization techniques, enabling the representation of various fluid flow phenomena in an intuitive and comprehensive manner. Through the application of ParaView, key parameters such as flow patterns, velocity distributions and pressure gradients can be visualized, providing valuable insights into the behavior of fluids within the computational domain. The interactive nature of ParaView facilitates efficient exploration and analysis of large datasets.

In this section, visualizations for one of the simulation cases discussed earlier are presented. The figures below are for scenario 4 from table 7.1. Furthermore, visualizations for the other cases will be presented in appendix D, ensuring a comprehensive overview of the simulated phenomena and their analysis.

For the dataset corresponding to the mentioned scenario, a series of figures were generated to provide comprehensive insights into the flow dynamics within the computational domain. Figure 7.2 showcases the magnitude of the flow velocity at every point within the domain. This figure offers a detailed depiction of how fluid velocities vary throughout the trench, providing valuable information on the intensity and distribution of flow patterns.Additionally, the figure was created to illustrate flow directions, employing arrows to showcase the orientation and magnitude of velocity vectors.

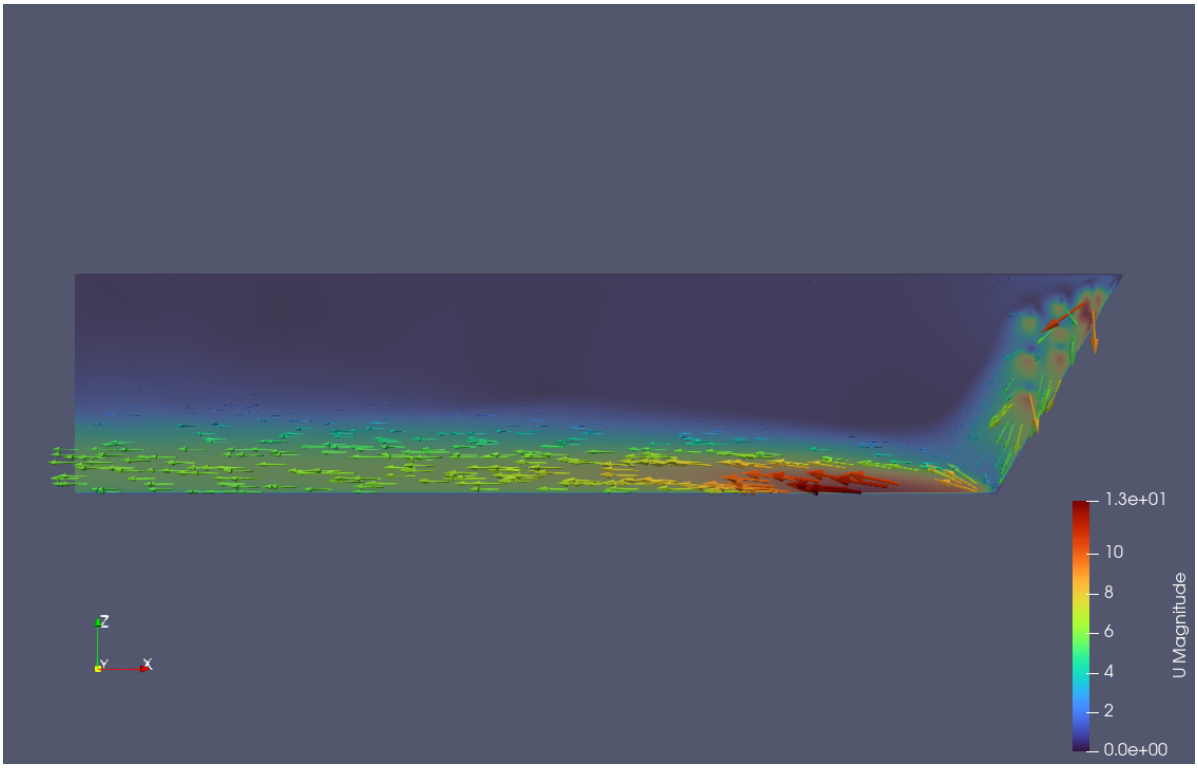

Figure 7.2: Flow velocity direction scenario 4

The figure was specifically generated at a slice in the middle of the trench, by doing this the domain changes from 3D to 2D. Which helps with further processing of the results. The middle of the trench can be assumed to be the best location for a slice, since the cable will also be laid in the middle of the trench.

Moreover, in addition to visualizing flow characteristics, ParaView was utilized to determine shear stress at the bottom of the trench. Shear stress is a crucial parameter for the analysis of shields parameters, which was described in section 6.5.1.

The reliability and accuracy of the CFD simulation outcomes are crucial for gaining insights into complex fluid behaviors. A validation process is essential to ensure that the simulated flow field represents real-world phenomena. In this context, the agreement between simulation results and empirical observations serves as a validation.

An important aspect of validating the simulated flow field is comparing it to real-world observations or experiments. In this study, one particularly compelling validation method involved releasing a sand particle into the simulated flow field and observing its trajectory, Appendix C.1 to C.4. This experiment was conducted to mimic real-world scenarios encountered by DEME in the field.

The trajectory of the sand particle in the simulated flow field was tracked and compared to practical experience by DEME during their field operations. Remarkably, the trajectory of the sand particle in the simulated flow field matched to the expected behavior by DEME. This alignment between simulation results and expectations supports the reliability and accuracy of the simulated flow field.

Importantly, figure 7.2 was generated at the moment when the simulation reached a steady-state solution. As described previously, the steady-state solution marks the point of interest for this study, representing a stable equilibrium state where fluid dynamics have stabilized. By capturing the flow characteristics at this moment, the data can be interpreted at the point of interest. This is because the trencher moves relatively slow forward compared to the flow velocity, which means the steady state flow will always be reached.

7.3. Post-Processing

The slice data, as previously described, was exported from ParaView in a CSV (Comma-Separated Values) format, facilitating easy processing in Python. The exported parameters include the flow velocity magnitude and direction (U), pressure (p), and shear stress at the bottom of the trench. This exportation allows for integration of the data into Python-based analysis, enabling further manipulation, visualization, and interpretation of the simulation results. Again, the processes and figures shown in this section are based on data from scenario 4 from table 7.1, the same process has been applied to the other scenarios. The figures for the other scenarios can be found in Appendix E. The total Python code for all scenarios can be found in Appendix G.

7.3.1. Setting Up the Flow Field

In setting up the flow field analysis in Python, the initial step involved importing and processing the exported data from ParaView as shown in figure 7.3. Following this, the computational domain was established within the Python environment to facilitate further analysis. This involves defining the domain boundaries, grid resolution, and any necessary boundary conditions. Once the computational domain was configured, the data from ParaView was integrated over the grid cells to accomplish the flow field in the trench. Figure 7.4 shows the flowfield as it was used to perform the Verlet integration.

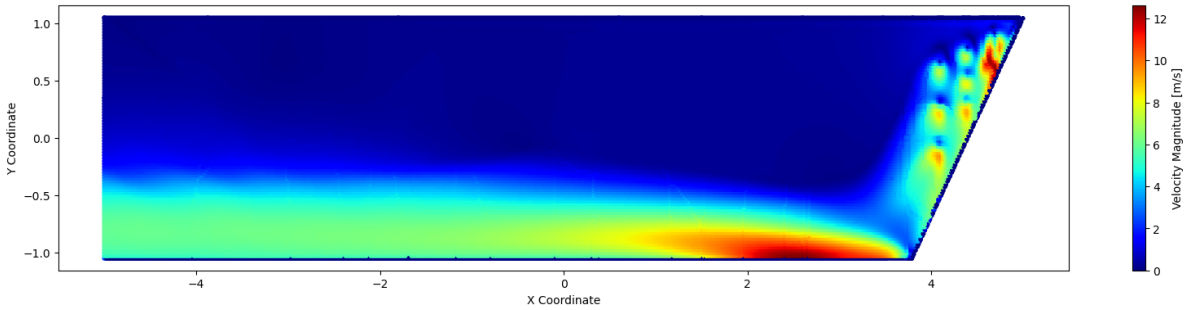

Figure 7.3: Imported data paraView scenario 4

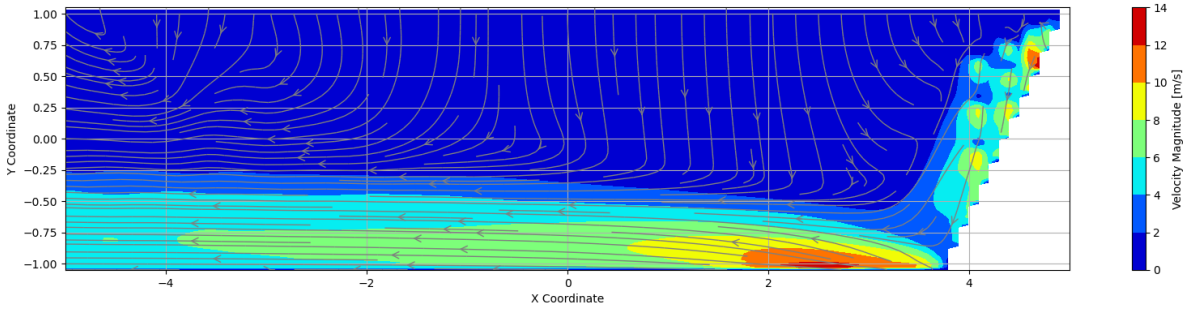

Figure 7.4: Representation of the flowfield in Python scenario 4

7.3.2. Checking Shields Criterion

The wall shear stress data imported from the CSV file was utilized to generate visualizations. A plot depicting the distribution of wall shear stress along the bottom of the trench was created for visualization purposes, providing insights into the spatial variation of shear stress magnitude. This visualization, represented in Figure 7.5, offers a clear depiction of how shear stress is distributed along the trench bottom.

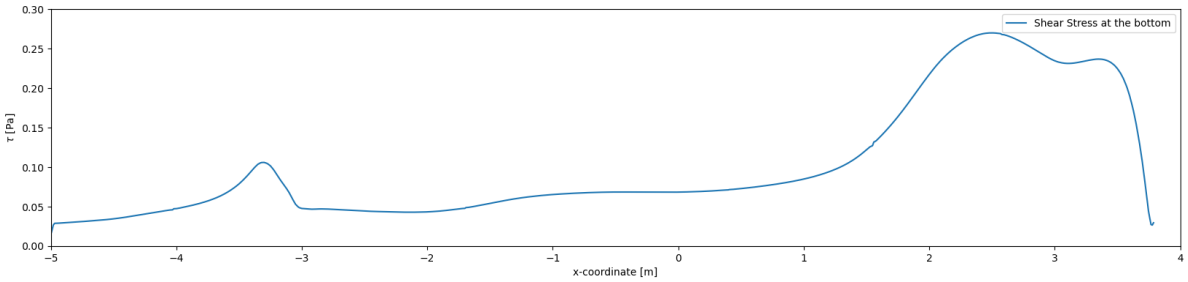

Figure 7.5: Wall shear stress along the bottom of the trench scenario 4

After importing the wall shear stress at the bottom of the trench, the Shields criterion (section 6.5.1) can be checked. Figure 7.6 shows the Shields parameter along the bottom of the trench as well as the critical value. Clearly, in this case the criterion is not met which means the particles (of this diameter) will not move after they have reached the bottom of the trench.

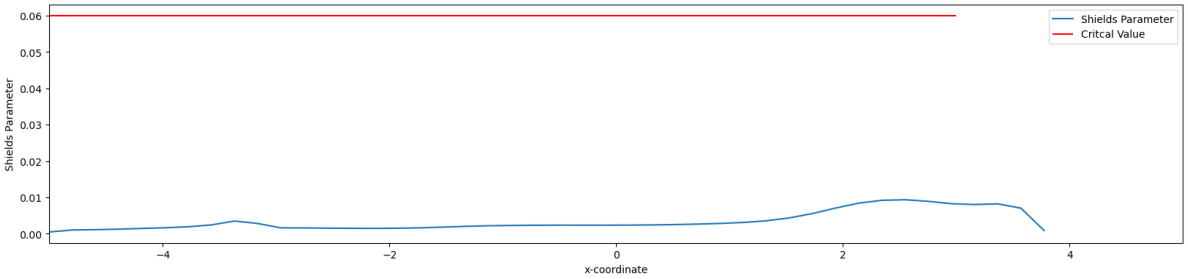

Figure 7.6: Shields parameter along the bottom of the trench scenario 4

7.3.3. Verlet Integration

After setting up the flow field and checking shields criterion, the next step is to perform the Verlet integration. The process and equations described in section 6.4.2 are translated into a `Python` script which can be found in Appendix 7.4. To test the process, first a particle with diameter 50 mm was released at a random location close to the jetting swords. Figure 7.7 showcases the path of the particle with the purple line. The particle was released at the right side of the figure close to the jetting swords.

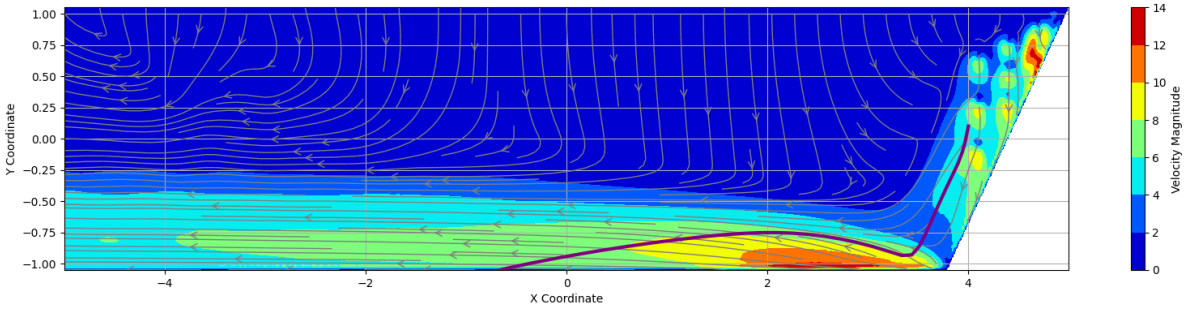

Figure 7.7: Path of a single particle with diameter 50 mm scenario 4

7.3.4. Sensitivity Analysis

As outlined in Section 7.1.2, the Verlet integration method involves two crucial initial conditions: the starting position and the diameter of the particle. Once the process and `Python` code have been confirmed to be functioning correctly, the subsequent phase involves exploring various starting positions for the particles, as described in detail in Section 7.1.2. Specifically, this entails selecting 10 equally spaced points on two lines situated in close proximity to the jetting swords, as illustrated in Figure 7.1. By implementing this approach, the aim is to determine the impact of the starting position on the trajectory endpoints of the particles.

Figures 7.8 and 7.9 illustrate the trajectories of particles originating from the purple and blue dotted lines. Notably, the end positions of the particles appear relatively close to each other. This observation can be attributed to a distinct pattern observed in the particle movement: initially, all particles are transported near the bottom of the trench. Subsequently, the upward flow generated by the backward nozzles and reflection of the downward flow propels the particles upwards and backwards. Following this phase, the particles' trajectories are influenced by both drag force and gravity, leading them to settle at various points along the bottom. This consistency across diverse starting points suggests that the final position of a particle is relatively insensitive to its initial starting point.

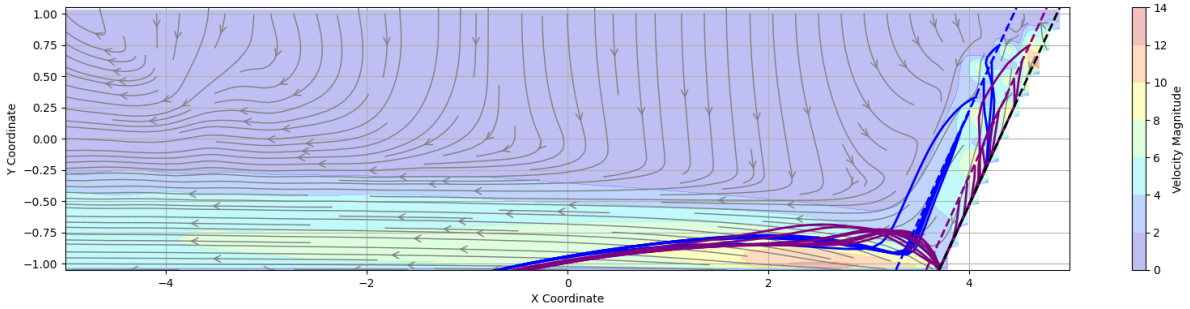

Figure 7.8: Paths of multiple particles with diameter 50 mm scenario 4

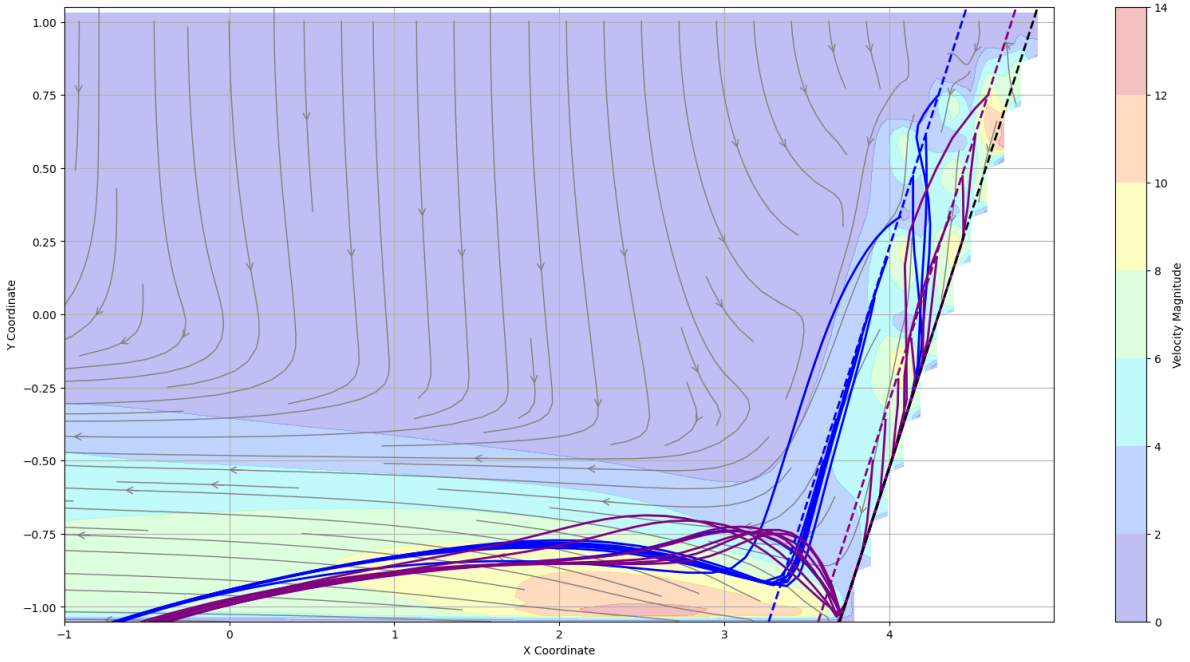

Figure 7.9: Detailed paths of multiple particles with diameter 50 mm scenario 4

To further explore the sensitivity of the bottom endpoint to the second initial condition, namely the particle size, the subsequent phase of the analysis involves varying the diameter rather than the starting position. Since it has been established that the endpoint is not sensitive to the starting position, this aspect remains constant. Instead, particles of various diameters are released from a starting point near the jetting sword. This approach aims to assess how changes in particle size influence the final resting position at the bottom of the trench.

As previously noted, this research focuses on investigating particles with diameters ranging from 10 to 100 mm. Initial findings revealed that for a particle diameter of 50 mm, the shield criterion was not satisfied at any point along the bottom of the trench. To extend this analysis across the entire diameter range, a reassessment of the shield criterion is conducted. The results of this evaluation for the entire range of diameters are presented and visualized in Figure 7.10. Again, for each diameter included in this research, the Shields criterion is not met at any point along the bottom of the trench.

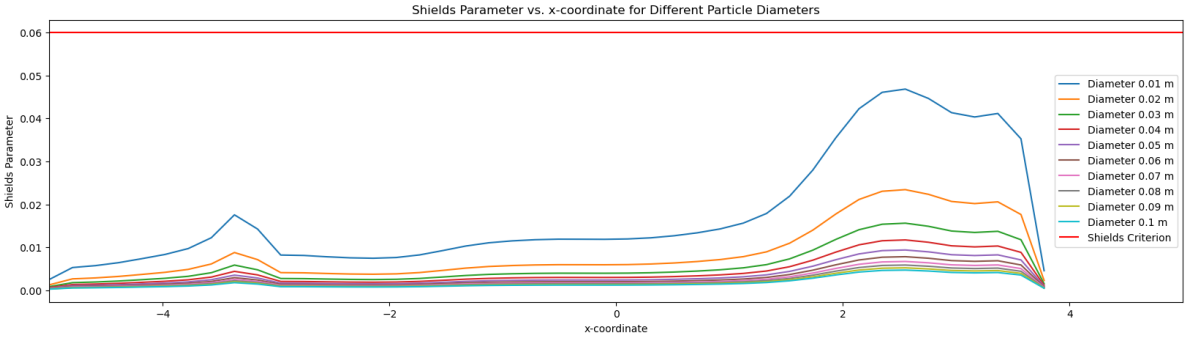

Figure 7.10: Shields parameter along the bottom of the trench for multiple diameters scenario 4

To highlight the sensitivity of the bottom endpoint in the trench, Figure 7.11 displays the trajectories of particles with varying diameters. In contrast to the analysis involving different starting points, it is evident that the endpoints exhibit a significantly greater spread. This observation suggests that the sensitivity to particle size is considerably more pronounced. By showcasing the diverse paths taken by particles of different diameters, this visualization underscores the notable influence that particle size exerts on the final resting position within the trench.

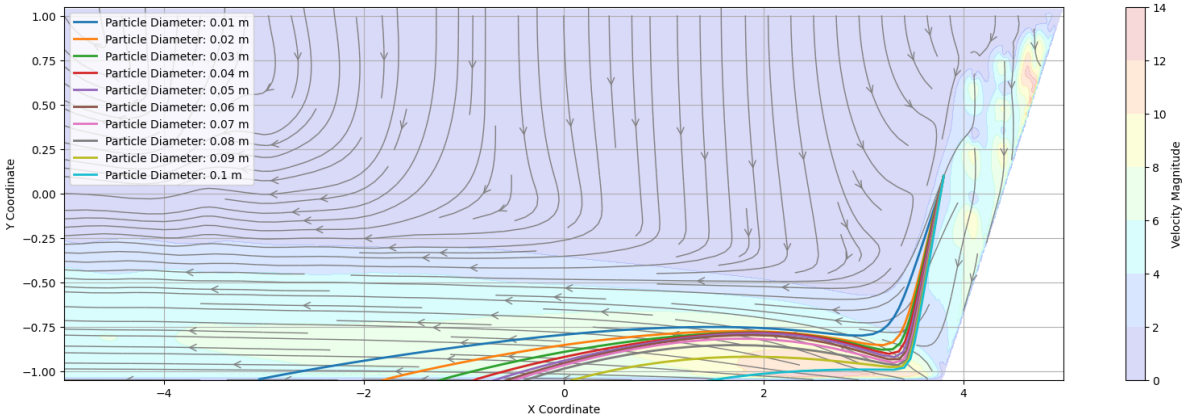

Figure 7.11: Trajectories of particles with different particle size scenario 4

7.4. Interpretation of Results

This section delves into the interpretation of simulation and post-processed results, crucial for extracting meaningful insights and practical implications. To effectively utilize the obtained data, incorporation of the cable shape into the showcased figures is essential. Given the established insensitivity of endpoint positions to starting positions, the analysis focuses on the influence of particle diameter size. In this interpretation, a critical consideration is the relative positioning of particles and the cable at the bottom of the trench. Specifically, if a particle reaches the trench bottom before the cable touchdown point, it suggests that the cable settles on top of the particle, leading to loss of burial depth.

For a comprehensive assessment, trajectories of particles are compared across three different cables commonly used by DEME as presented in table 7.2. The trajectory of the cable can be calculated with equation 7.1, which is derived from a cantilever beam model (Vanden Berghe et al., 2008). A large factor in the cable deflection calculation is the tension in the cable which is depending on the metocean conditions. Therefor a range of values has been used in this analysis. For the cables presented in table 7.2, a range of 1500 - 4500 N is sufficient.

$$z(x) = -[\frac{qL}{T}\sqrt{\frac{EI}{T}}\frac{\cosh\sqrt{\frac{T}{EI}}L}{\sinh\sqrt{\frac{T}{EI}}L}[\cosh\sqrt{\frac{T}{EI}}x - \tanh\sqrt{\frac{T}{EI}}x\sinh\sqrt{\frac{T}{EI}}L - 1] - \frac{q}{2T}x^2 + \frac{qL}{T}x] \tag{7.1}$$

where
- z : Cable deflection [m]
- q : Cable weight [$\mathrm{N\,m^{-1}}$]
- T : Tension in the cable [N]
- EI : Bending stiffness [$\mathrm{N\,m^2}$]
- L : Distance untill touchdown point [m]
- x : Distance from the front of the trench [m]

Characteristic	Unit	240mm^2 (Cable 1)	240mm^2 (Cable 2)	240mm^2 (Cable 3)
Submerged cable Weigth	[N/m]	152	144	155
Tension in the Cable	[N]	1500-4500	1500-4500	1500-4500
Bending Stiffness	[Nm^2]	1530	2000	2700

Table 7.2: Cables included in the research

Figures 7.12 to 7.14 present a comparison between the cable shape and the trajectories of particles with varying diameters within the trench. Upon close examination, a trend emerges: the majority of particle trajectories terminate prior to the cable reaching the bottom of the trench. Notably, the figures presented in this section apply to scenario 4 from table 7.1. However, similar results for other scenarios can be found in Appendix E.

Such findings suggest a notable risk of burial depth loss within the trench for the particle diameters represented in the analysis. Specifically, for these diameters, it appears that a substantial portion of particles settles before the cables touchdown point, leading to compromised burial depth. This phenomenon is crucial to consider in the context of underwater trenching operations, where maintaining desired trench depths is important for successful installation of subsea cables.

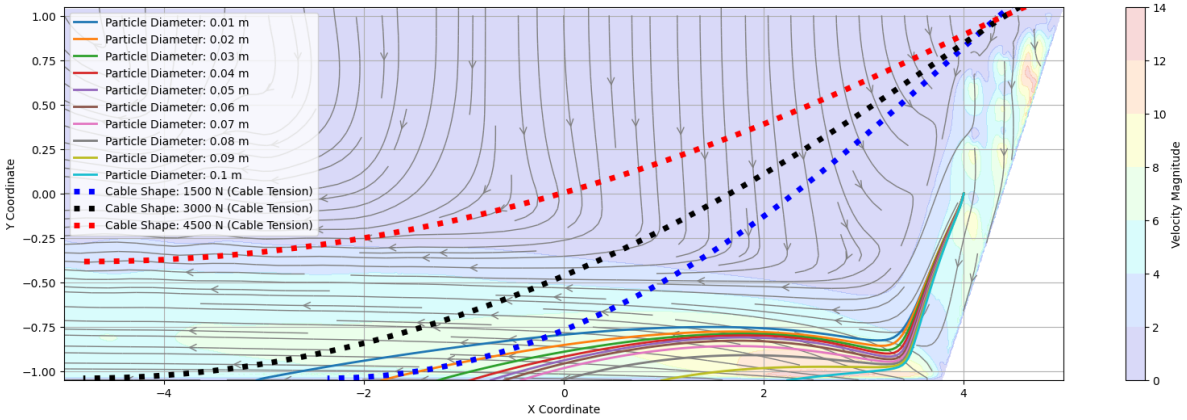

Figure 7.12: Trajectory of particles with different particle size and cable shape scenario 4 (cable 1)

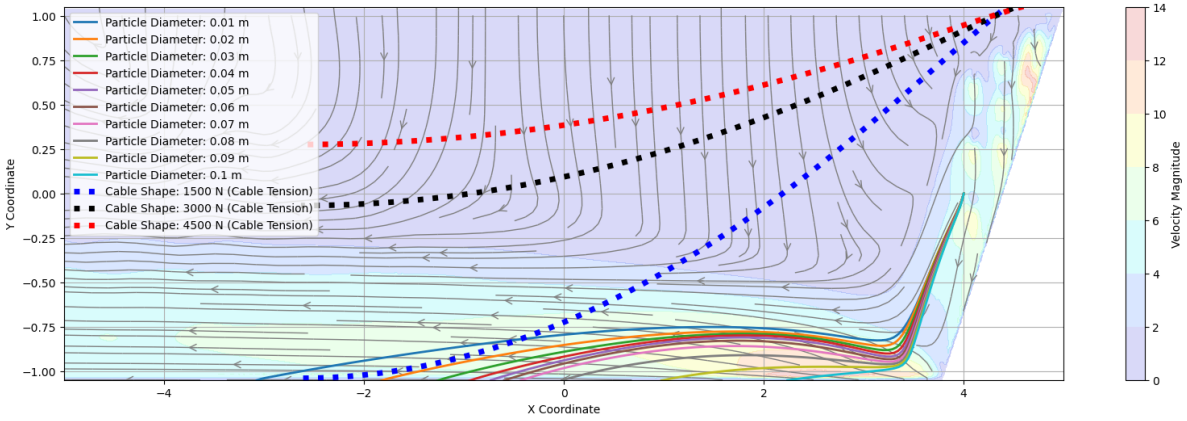

Figure 7.13: Trajectory of particles with different particle size and cable shape scenario 4 (cable 2)

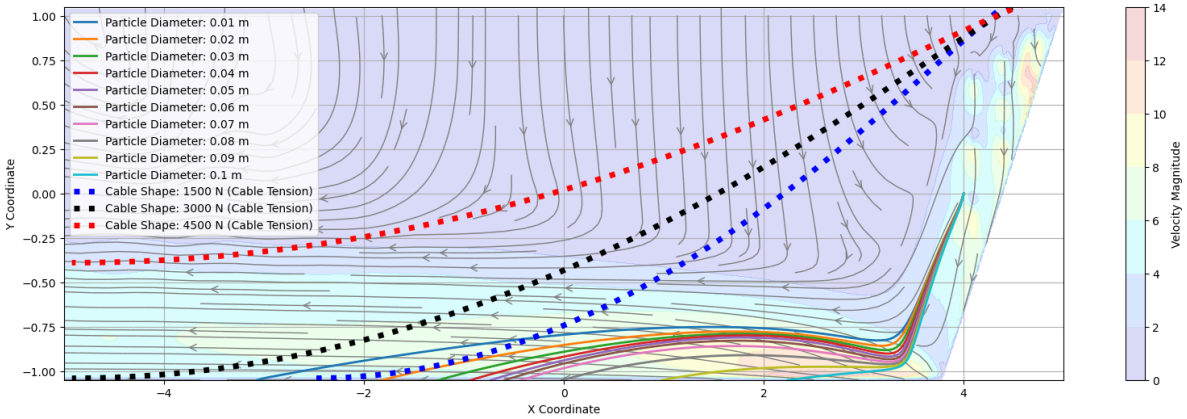

Figure 7.14: Trajectory of particles with different particle size and cable shape scenario 4 (cable 3)

7.5. Loss of Burial Depth

This study examines not only particle trajectories and cable behavior during jet trenching but also addresses the critical aspect of cable burial depth, as depicted in Figure 4.5. Simulation results shown in figure 7.12 to 7.14 revealed an unfavorable cable burial depth, with a notable portion of the trench profile showing inadequate cable coverage by clay particles.

To simulate this scenario, an assumption was made regarding the distribution of clay particles in the trench. Assuming equal distribution of different particle diameters (10% each), 30% of the particles were estimated to be pulverized during trenching, while the remaining 70% formed the sediment bed. Visualizations of the trench profiles, depicted in Figure 7.15 to 7.18, were generated based on this assumption. Visualizations for the other scenarios are given in Appendix F.

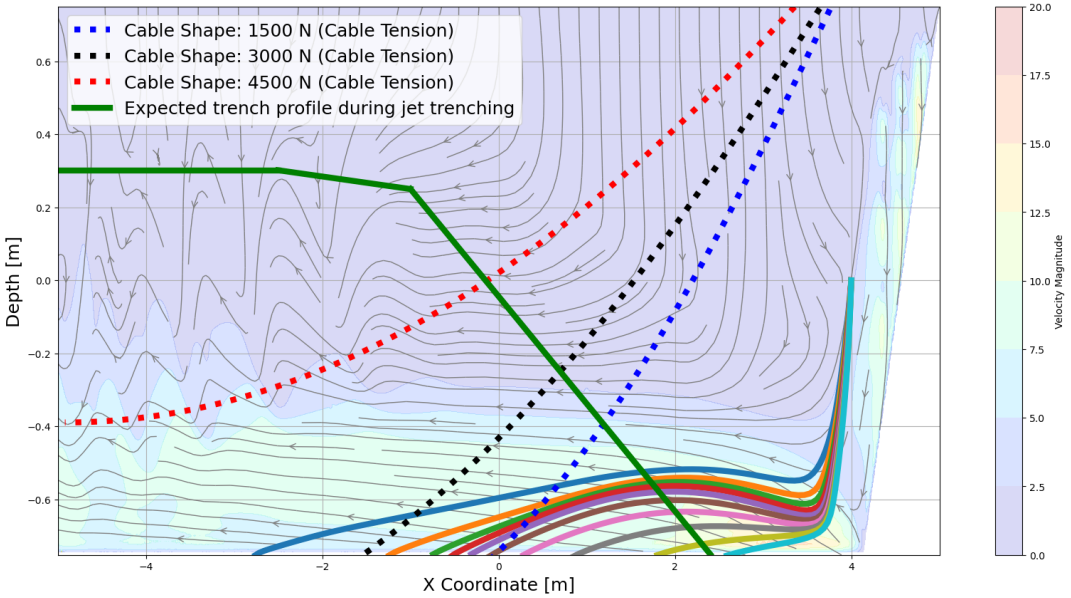

Figure 7.15: Trench profile & touchdown point scenario 1 (cable 1)

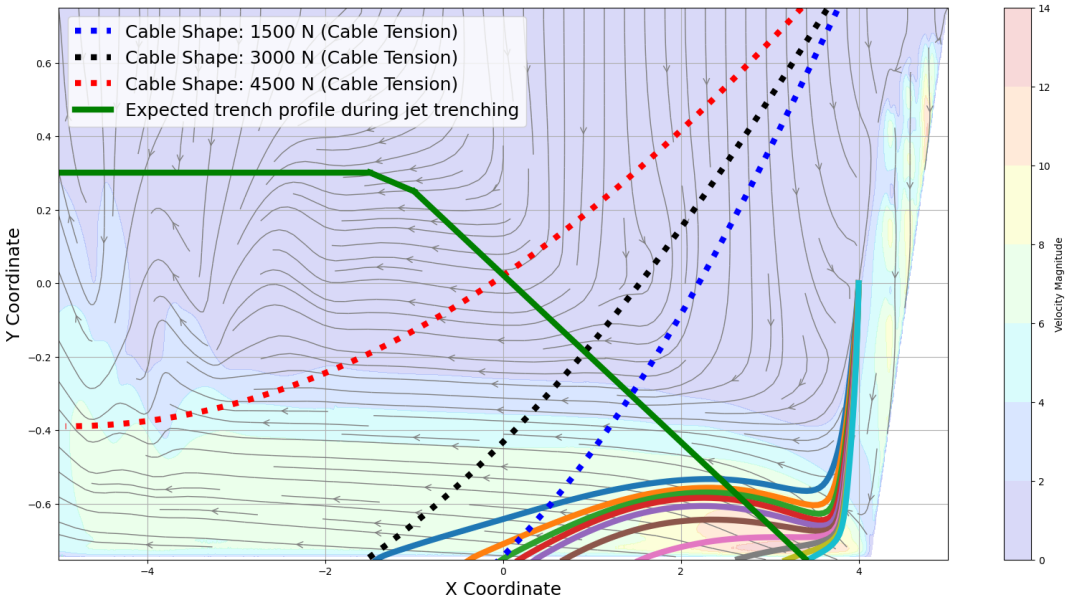

Figure 7.16: Trench profile & touchdown point scenario 2 (cable 1)

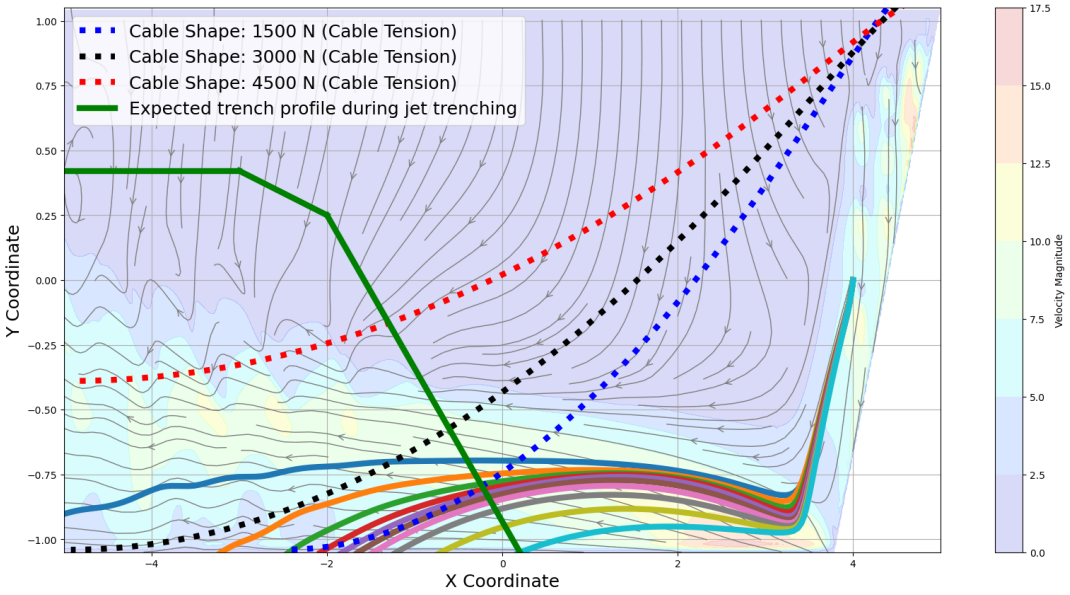

Figure 7.17: Trench profile & touchdown point scenario 3 (cable 1)

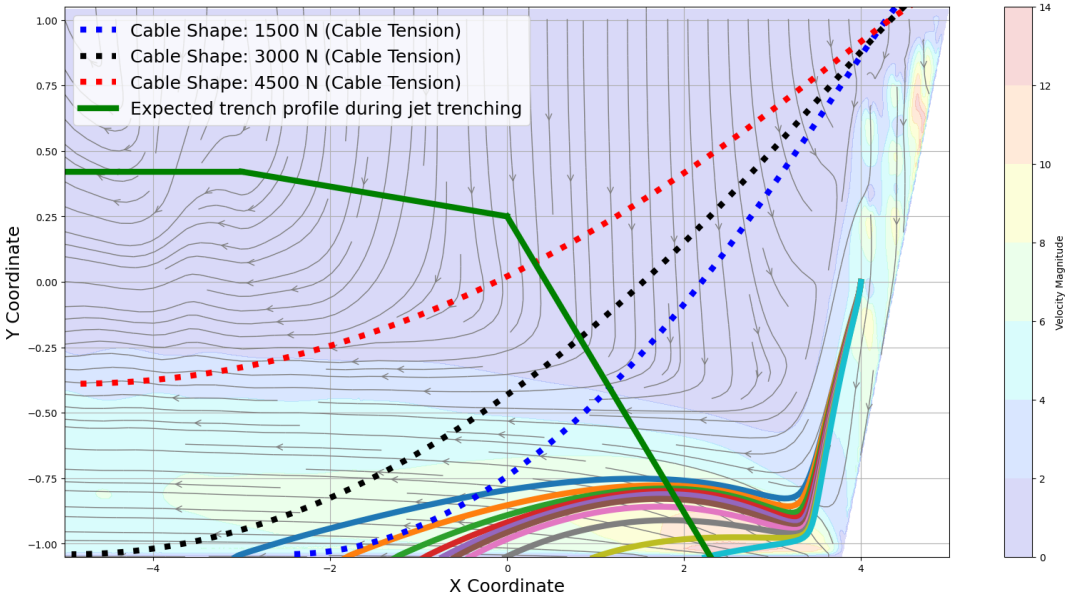

Figure 7.18: Trench profile & touchdown point scenario 4 (cable 1)

These visualizations offer a comprehensive view of the complexities involved in attaining adequate cable burial depth during jet trenching operations in cohesive soils. They illustrate the distribution of clay particles and their interaction with cable placement, shedding light on the challenges associated with ensuring sufficient coverage. Through these simulations, a deeper understanding of the practical implications for subsea cable installation in cohesive soil is gained.

8

Conclusions & Recommendations

The comprehensive analysis and simulation conducted in this thesis shed light on the dynamics of jet trenching operations in clay seabeds, providing valuable insights into the behavior of particles and fluid flow within the trenching environment. Through the utilization of CFD simulations and Verlet integration methods, coupled with post-processing techniques, significant findings have been found, contributing to a deeper understanding of the trenching process and its implications. This section presents a summary of the key findings drawn from the study, followed by recommendations for future research and practical applications.

8.1. Conclusions & Discussion

In the domain of jet trenching modelling, the integration of CFD simulations marks a significant advancement, complementing the models currently utilized by DEME. These models primarily rely on the depth to which jetting sword nozzles penetrate the seabed to forecast jet trenching outcomes. However, by incorporating principles from fluid dynamics and particle behavior, the CFD model offers a more comprehensive understanding of the trenching process

1. **Jet trenching in cohesive soil:** For the diameter sizes explored in this thesis, trenching in clay seabeds may not be feasible due to the observed phenomenon where a significant proportion of particles tend to accumulate at the bottom of the trench before the cable touchdown point. This highlights the challenges associated with jet trenching in clay seabeds, particularly when dealing with larger particle sizes.

2. **Diameter size:** A pivotal finding of this study is the substantial influence of particle diameter on modelling outcomes. The analysis conducted reveals the crucial role that particle size plays in determining the behavior and settling patterns of particles within the trench. On the other hand, the starting position of the particles do not have a significant influence on the trajectory of the particles.

3. **Dimensions clay blocks:** Furthermore, the findings emphasize the necessity for further investigation into the dimensions of clay blocks and particles generated during trenching operations. While the modelling approach made assumptions about particle sizes based on anticipated clay block dimensions, it is crucial to validate these assumptions empirically. Additionally, experimental studies could provide valuable insights into particle behavior under varying flow conditions, thereby improving the refinement of predictive model.

4. **Dimensions trench:** Moreover, the dimensions of the trench itself remain a subject of discussion requiring further exploration. The depth, width, and profile of the trench impact cable burial depth and the stability of trench walls. Future research efforts should prioritize field studies and experimental tests to better understand the optimal trench dimensions across different soil types and environmental conditions.

5. **Trench shape and particle trajectory:** It is important to note that the shape of the trench during jet trenching operation, as depicted in Figure 7.15 to 7.18, is not taken into account regarding the cable shape and the trajectory of particles. This simplification may introduce limitations in the accuracy of the modelling results and requires consideration in future studies.

6. **Flow rate increase:** Increasing the flow rate will possibly have an impact on the outcome of the jet trenching operation. However, this factor has not been taken into account in this research. This research is based on the working point as discussed in section 6.3.4.

7. **Pulverization:** An important factor not fully addressed in this research is the pulverization of clay blocks by jets below their starting point. If pulverization occurs, it leads to a reduction in particle diameter, which in turn affects sediment transport dynamics within the trench and ultimately impacts cable burial depth. The assumption of 30%/70% distribution, plays a significant role in determining the outcomes of the cable burial depth calculation in this study. Further investigation into this assumption is needed to ensure the accuracy and reliability of the results.

In summary, the importance of particle diameter in trenching operations cannot be overstated. It was found to be a critical factor influencing trenching dynamics and cable burial depth. Consequently, further investigation into particle diameter is essential to develop a comprehensive understanding of trenching processes. While the CFD model enhances understanding of flow behavior behind the trench, its direct application may be limited due to the significant impact of particle diameter.

8.2. Recommendations

Based on the conclusions drawn from the study, several recommendations emerge that could enhance the understanding and validity of the model.

1. **Investigate Particle Diameter:** The study highlights the significant influence of particle diameter on trenching dynamics and cable burial depth. Therefore, further investigation into particle diameter is important. This can be achieved through experiments and field tests aimed at determination of the particle sizes which affect sediment transport and settling patterns within the trench. By conducting experiments, researchers can validate assumptions made in modelling approaches and refine predictive models accordingly.

2. **Higher flow rates:** Investigate the effects of increased flow rates on jet trenching outcomes. Higher flow rates are likely to significantly impact the trenching process, warranting further investigation.

3. **Investigate Trench Profile and Dimensions:** The dimensions of the trench, including depth, width, and profile, are important factors impacting cable burial depth and trench stability. Field studies and experimental tests can provide valuable insights into how different trench profiles and dimensions influence trenching outcomes.

4. **Investigate Pulverization:** A significant aspect not addressed in current models is the potential pulverization of clay blocks by jets below their starting point. Understanding this phenomenon and its impact on particle diameter is essential for accurately predicting trenching outcomes. Future research endeavors should focus on investigating the extent of pulverization and its implications for sediment transport dynamics and cable burial depth. Experimental studies and field observations can help to understand this process and inform the refinement of trenching models.

5. **Validate Model with Field Data:** While CFD simulations offer valuable insights into trenching processes, it is crucial to validate model predictions with field data. Field studies conducted in real-world marine environments can provide valuable empirical evidence to validate model outputs and ensure their accuracy and reliability. By comparing model predictions with field observations, researchers can identify areas for improvement and refine modelling approaches to better reflect actual trenching conditions.

In conclusion, the findings of this study offer valuable insights into the complexities of jet trenching operations in clay seabeds. While the challenges are significant, the advancements in modelling techniques and the insights gained from this research provide a solid foundation for further exploration and optimization of trenching methodologies. By addressing the recommendations outlined above, further research can work towards enhancing the efficiency, reliability, and sustainability of offshore cable installation processes.

Bibliography

Albertson, M., Dai, Y., Jensen, R., & Rouse, H. (1950). Diffusion of Submerged Jets. *American Society of Civil Engineers*.

Atmatzidis, D., & Ferrin, F. (1983). *LABORATORY INVESTIGATION OF SOIL CUTTING WITH A WATER JET* (tech. rep.).

Blevins, R. (1984). *Applied Fluid Mechanics Handbook* (tech. rep.).

Brunning, P., & Machin, J. (2014). Applications and performance of trenching technologies in Asia-Pacific. *Proceedings of the Annual Offshore Technology Conference*, *2*. https://doi.org/10.4043/24833-ms

Camp, T. R. (1936). *A Study of the Rational Design of Settling Tanks* (tech. rep. No. 5). https://www.jstor.org/stable/25028680

Camp, T. R. (1946). Sedimentation and the Design of Settling Tanks. *Transactions of the American Society of Civil Engineers*, *111*(1), 895–936. https://doi.org/10.1061/TACEAT.0005912

Cao, Z., Pender, G., & Meng, J. (2006). Explicit Formulation of the Shields Diagram for Incipient Motion of Sediment. *Journal of Hydraulic Engineering, 132*(10), 1097–1099. https://doi.org/10.1061/(asce)0733-9429(2006)132:10(1097)

Caretto, L. S., Gosman, A. D., Patankar, S. V., & Spalding, D. B. (2007). Two calculation procedures for steady, three-dimensional flows with recirculation. In *Proceedings of the third international conference on numerical methods in fluid mechanics* (pp. 60–68). Springer Berlin Heidelberg. https://doi.org/10.1007/bfb0112677

Cathie, D. (2018). *CBT1100 Trencher Performance Model Theory Manual* (tech. rep.). www.cathie-associates.com

DEME. (2021). Submarine Cable System.

Dietrich, W. E. (1982). *Settling Velocity of Natural Particles* (tech. rep. No. 6).

Dobbins, W. E. (1944). Effect of Turbulence on Sedimentation. *Transactions of the American Society of Civil Engineers*, *109*(1), 629–656. https://doi.org/10.1061/TACEAT.0005696

Fischer, H. B. (1979). *Mixing in inland and coastal waters*. Academic Press.

Ho, C. E. (2005). *Turbulent fluid jet excavation in cohesive soil with particular application to jet grouting* (tech. rep.).

Issa, R. I. (1985). *Solution of the Implicitly Discretised Fluid Flow Equations by Operator-Splitting* (tech. rep.).

Kamphuis, J., & Hall, K. (1983). Cohesive material erosion by unidirectional current. *Journal of Hydraulic Engineering*.

Lodhi, A. S., Jain, R. K., & Karna, N. (2017). *Temporal variation of scour at wake of the spur dikes in cohesive sediment mixtures* (tech. rep.). https://www.researchgate.net/publication/322683427

Machin, J., Allan, P., & Geomarine Limited, U., Newcatle. (2011). *State-of-the-art jet trenching analysis in stiff clays*. CRC Press/Balkema.

Machin, J., Messina, F., Mangal, J., Girard, J., & Finch, M. (2001). Recent Research on Stiff Clay Jetting. https://doi.org/10.4043/13139-ms

Miedema, S. A., & Vlasblom, W. J. (1995). *THEORY FOR HOPPER SEDIMENTATION* (tech. rep.).

Mitchell, J. K., & Soga, K. (2005). *Fundamentals of Soil Behaviour, 3rd Edition* (tech. rep.).

Njock, P. G. A., Zheng, Q., Zhang, N., & Xu, Y. S. (2020). Perspective review on subsea jet trenching technology and modeling. https://doi.org/10.3390/jmse8060460

Nobel, A. J. (2013). *On the excavation process of a moving vertical jet in cohesive soil* (tech. rep.).

Prandtl, L. (1920). Theory of Lifting Surfaces.

Rajaratman, N. (1982). Erosion by submerged circular jets.

Richardson, J. F., & Zaki, W. N. (1954). *The sedimentation of a suspension of uniform spheres under conditions of viscous flow* (tech. rep.). Pergamon Press Ltd.

Rowe, P. (1987). A convenient emperical equation for estimation of the Richardson-Zaki exponent.

Shearer, S. A., & Hudson, J. R. (2008). *Fluid Mechanics: Stokes' Law and Viscosity* (tech. rep.).

Shields, A. (1936). *Application of Similarity Principles and Turbulence Research to Bed-Load Movement* (tech. rep.).

Srinil, N. (2016). Cabling to connect offshore wind turbines to onshore facilities. In *Offshore wind farms: Technologies, design and operation* (pp. 419–440). Elsevier Inc. https://doi.org/10.1016/B978-0-08-100779-2.00013-1

Terzaghi, K., Wiley, J., York, N., & Peck, R. B. (1943). *Soil Mechanics in Engineering Practice* (tech. rep.).

Van Rhee, I. C. (2017). *Lecture Notes OE4727* (tech. rep.).

Van Rijn, L. (2020). Settling Velocity of Mud.

Van Rijn, L. C. (2007). Unified View of Sediment Transport by Currents and Waves. I: Initiation of Motion, Bed Roughness, and Bed-Load Transport. https://doi.org/10.1061/ASCE0733-94292007133:6649

Vanden Berghe, J.-f., Engineers, F. S., Capart, H., & C Su, J. C. (2008). *OTC 19441 Jet Induced Trenching Operations: Mechanisms Involved* (tech. rep.).

Verlet, L. (1967). *Computer "Experiments" on Classical Fluids. I. Thermodynamical Properties of Lennard-Jones Molecules* (tech. rep.).

Verruijt, A. (2001). *Soil Mechanics* (tech. rep.). http://geo.verruijt.net/.

Versteeg, H. K., & Malalasekera, W. (2007). *An Introduction to Computational Fluid Dynamics Second Edition* (tech. rep.). www.pearsoned.co.uk/versteeg

Waltham, T. (1994). *Foundations of Engineering Geology*.

Wang, B., van Rhee, C., Nobel, A., & Keetels, G. (2021). Modeling the hydraulic excavation of cohesive soil by a moving vertical jet. *Ocean Engineering, 227*. https://doi.org/10.1016/J.OCEANENG.2021.108796

Zhang, S., Ge, T., Zhao, M., & Wang, C. (2016). *The Prediction of Traveling Jet Trenching in Stiff Clay Based on the Erosion Failure Mechanism* (tech. rep.).

Zhang, S., Zhao, M., Ge, T., & Wang, C. (2016). Experimental Research on Trenching in Stiff Clay by Submerged Vertical Traveling Jets. *Journal of Coastal Research*, *32*(2), 365–373. https://doi.org/10.2112/JCOASTRES-D-14-00038.1

Zhou, T., & Li, H. (2000). *Force balance modelling for agglomerating fluidization of cohesive particles* (tech. rep.). www.elsevier.comrlocaterpowtec

Appendices

A

Equipment CBT 1100

DEME OFFSHORE

CBT 1100

ALLROUND OFFSHORE CABLE BURIAL SOLUTION

CBT 1100

ALLROUND OFFSHORE CABLE BURIAL SOLUTION

CONSTRUCTION YEAR	2012
TYPE	Subsea cable trencher
CLASSIFICATION	Lloyds CLAME

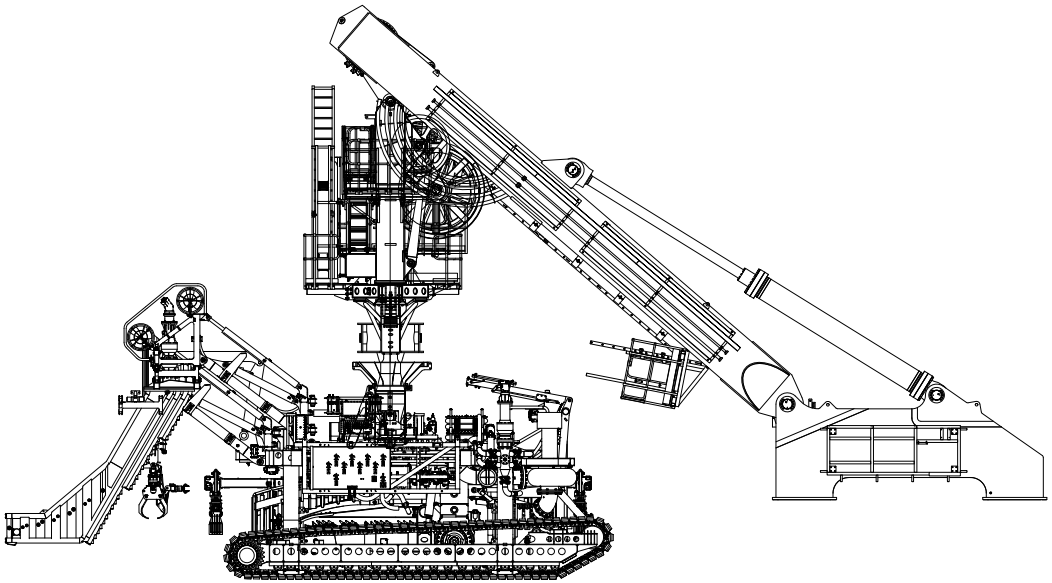

MAIN SPECIFICATIONS	length	14.5 m
	width	7.5 m
	height	5.5 m
	weight in air	45 - 55 ton
	depth rating	max. 1000 m
	track speed	max. 1000 m/hr
	installed power	1100 hp
	product diameter	max. 700 mm
	cutter highway MBR	4 m
OPERATIONAL MODES (1100 HP)	jetting FWD / AFT	max 3 m
	mechanical cutting	max 2.35 m
	hybrid	max 3 m
LAUNCH & RECOVERY	A-Frame	60 ton
	liftwinch	80 ton dual drum
	workability	seastate 6
SPECIAL FEATURES	high flow pumps	max. 1500 m^3/hr, max. 7 bar (per pump)
	high pressure pumps	max. 850 m^3/hr, max 20 bar (per pump)
	dredge pump	max. 2500 m^3/hr, max 3 bar
	cable guide	incl. live DoB indication
	cable grabs	2 pc 2 tonne cable grabs
	positioning	2 pc 500mm thrusters
	manipulator crane	palfinger PK110001 M
	monitoring / survey	cable tracker system, TSS440 & 350 blueview / cameras MBES / ADCP

DEME OFFSHORE

www.deme-group.com

B

Geometry

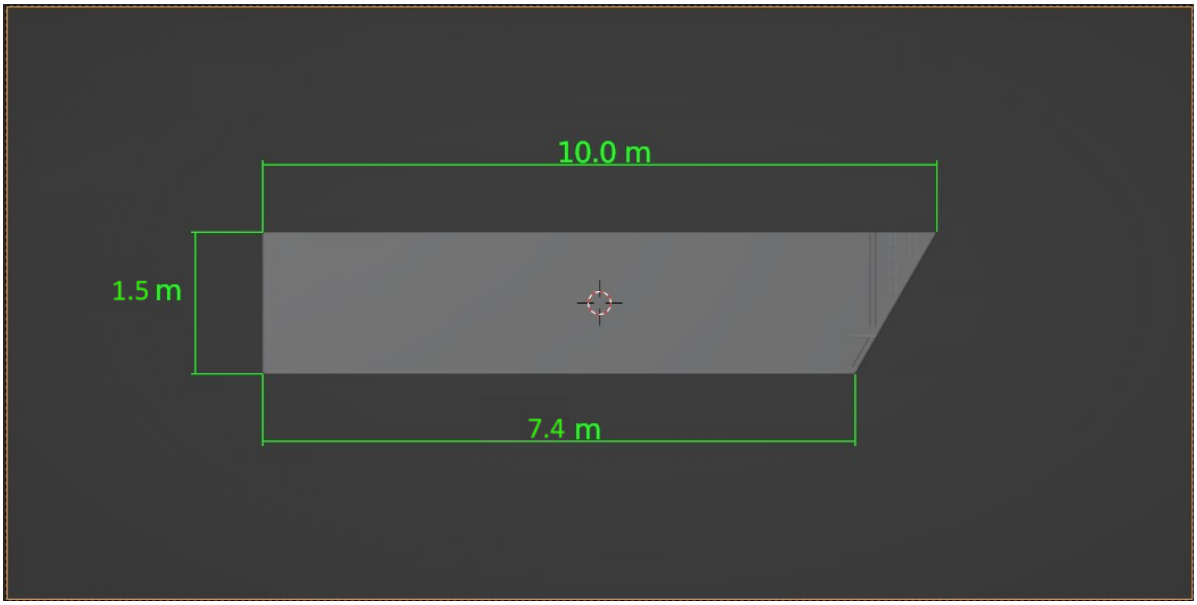

Figure B.1: Side view trench 1.5 [m]

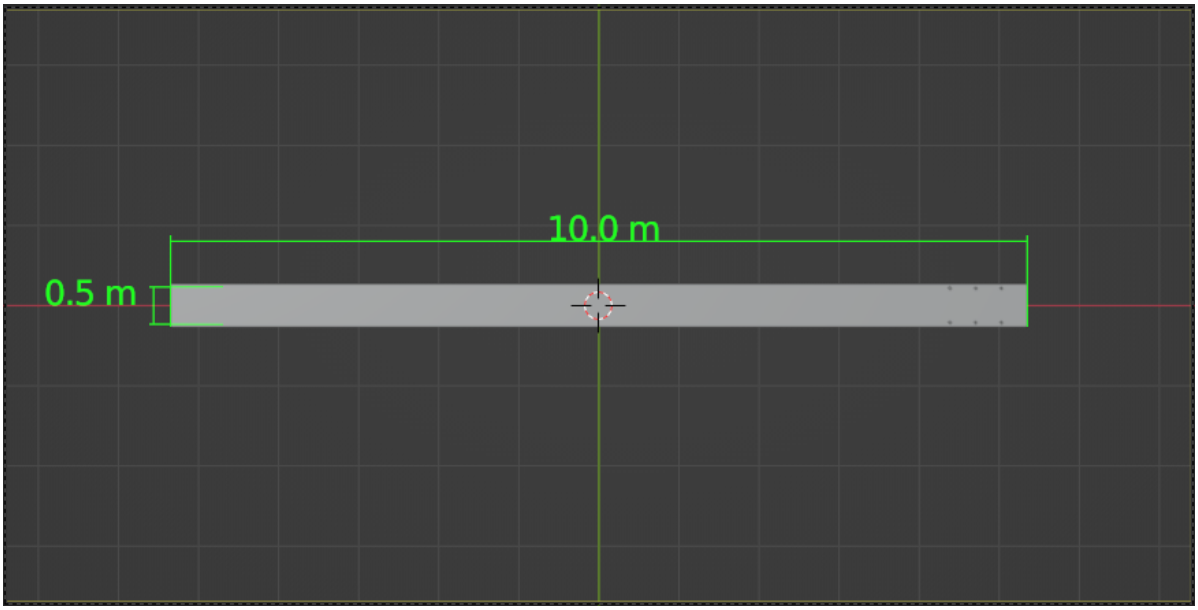

Figure B.2: Top view trench 1.5 [m]

C

Validation Flowfield

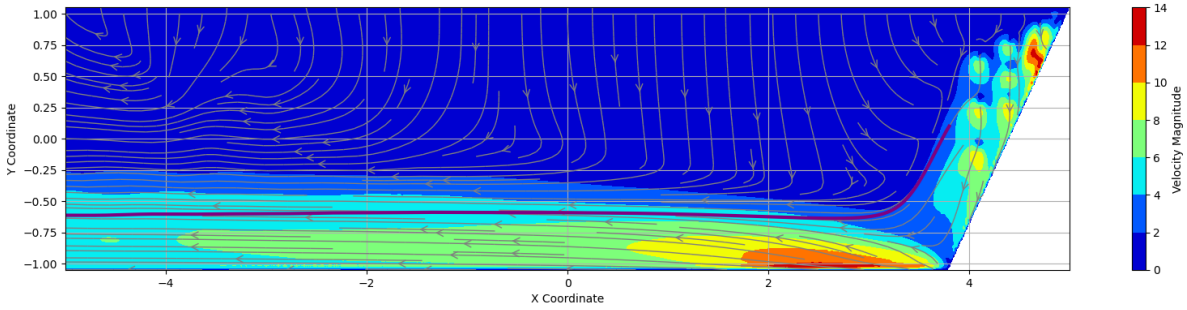

Figure C.1: Validation flowfield sand particle 1

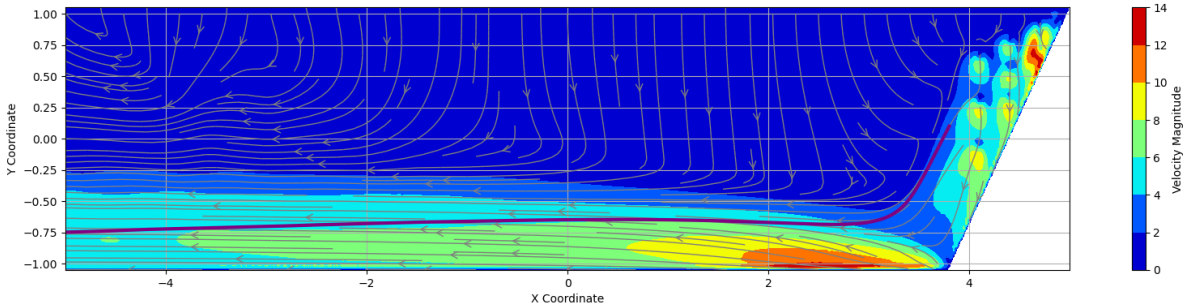

Figure C.2: Validation flowfield sand particle 2

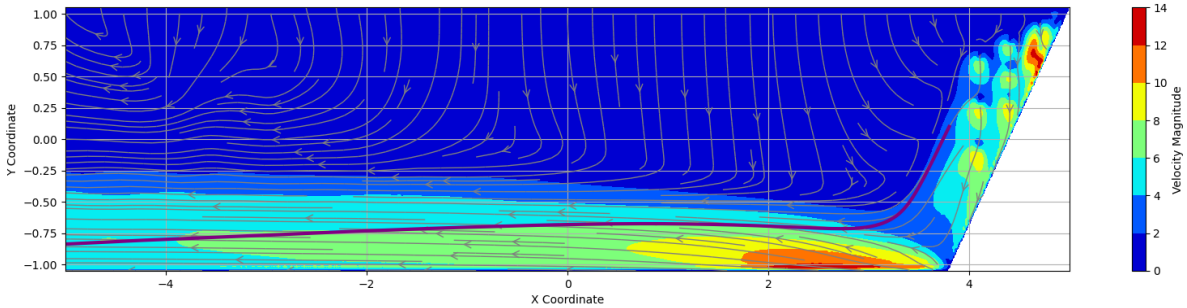

Figure C.3: Validation flowfield sand particle 3

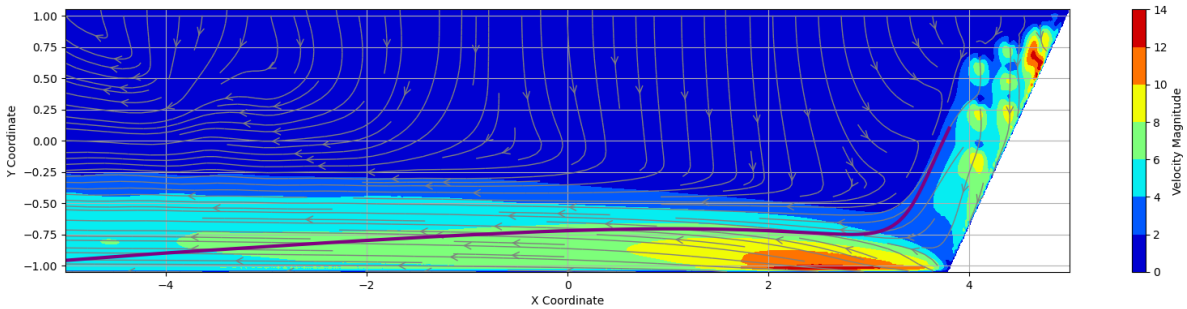

Figure C.4: Validation flowfield sand particle 4

D

Visualization Results

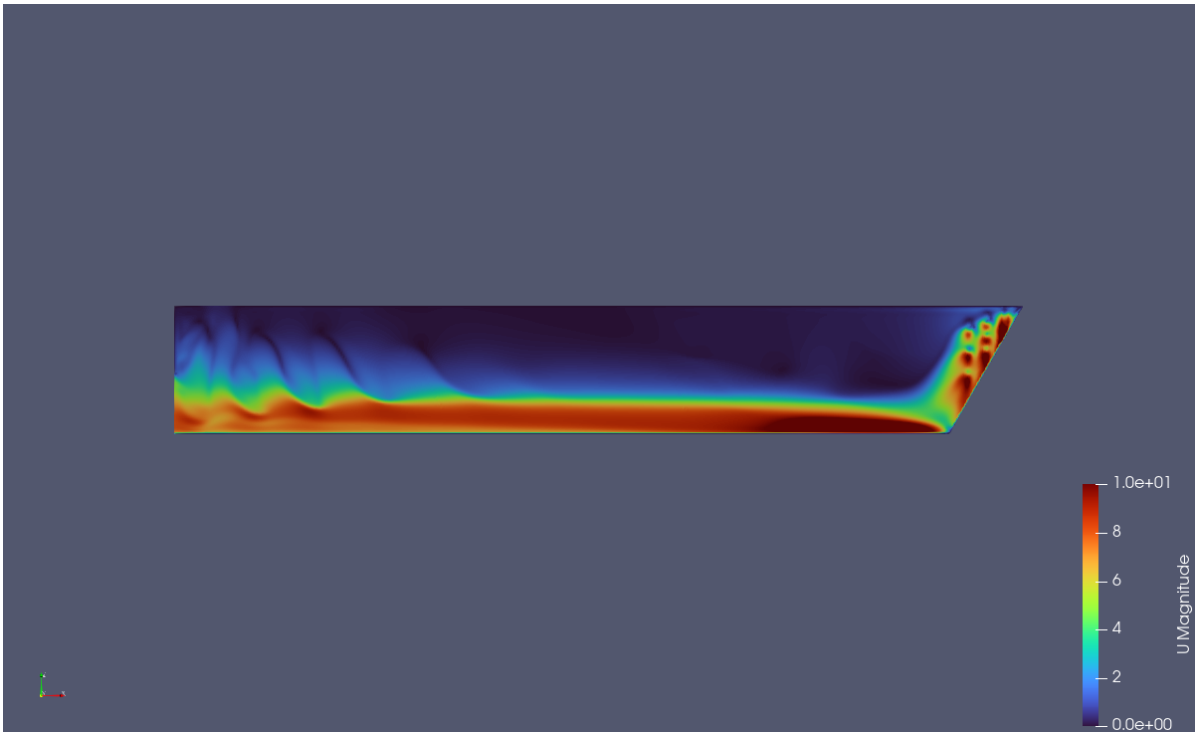

Figure D.1: Flow velocity magnitude scenario 1

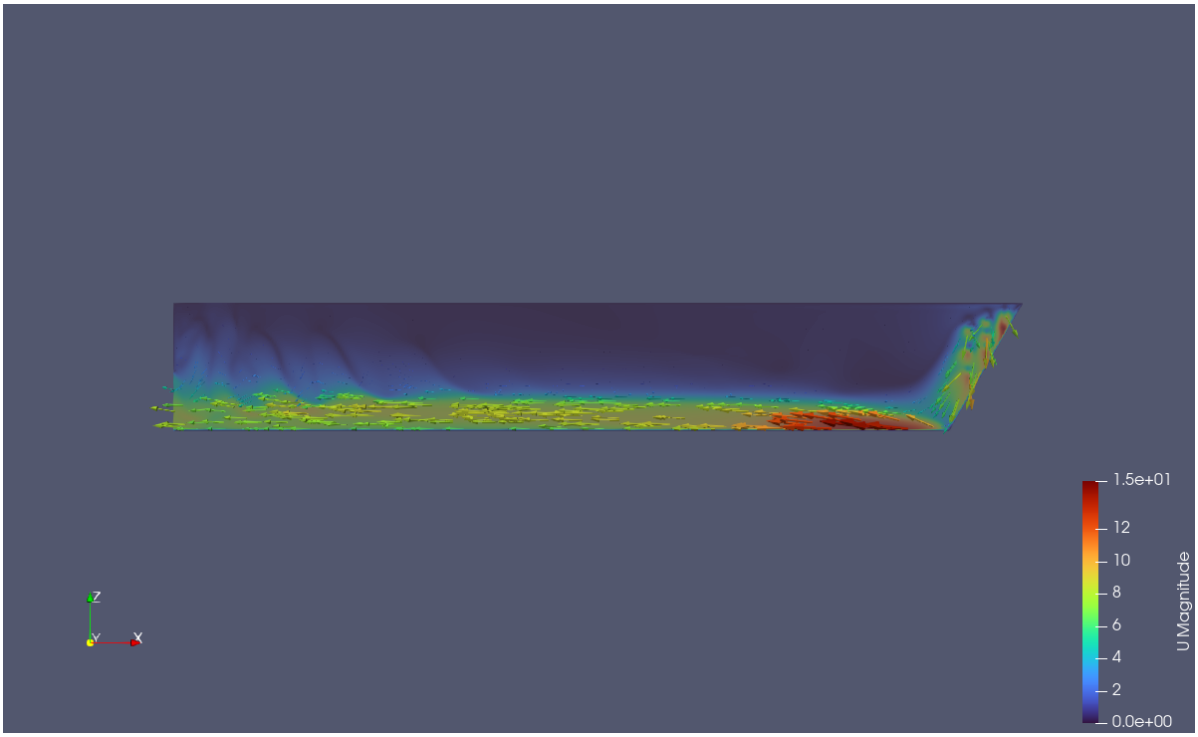

Figure D.2: Flow velocity direction scenario 1

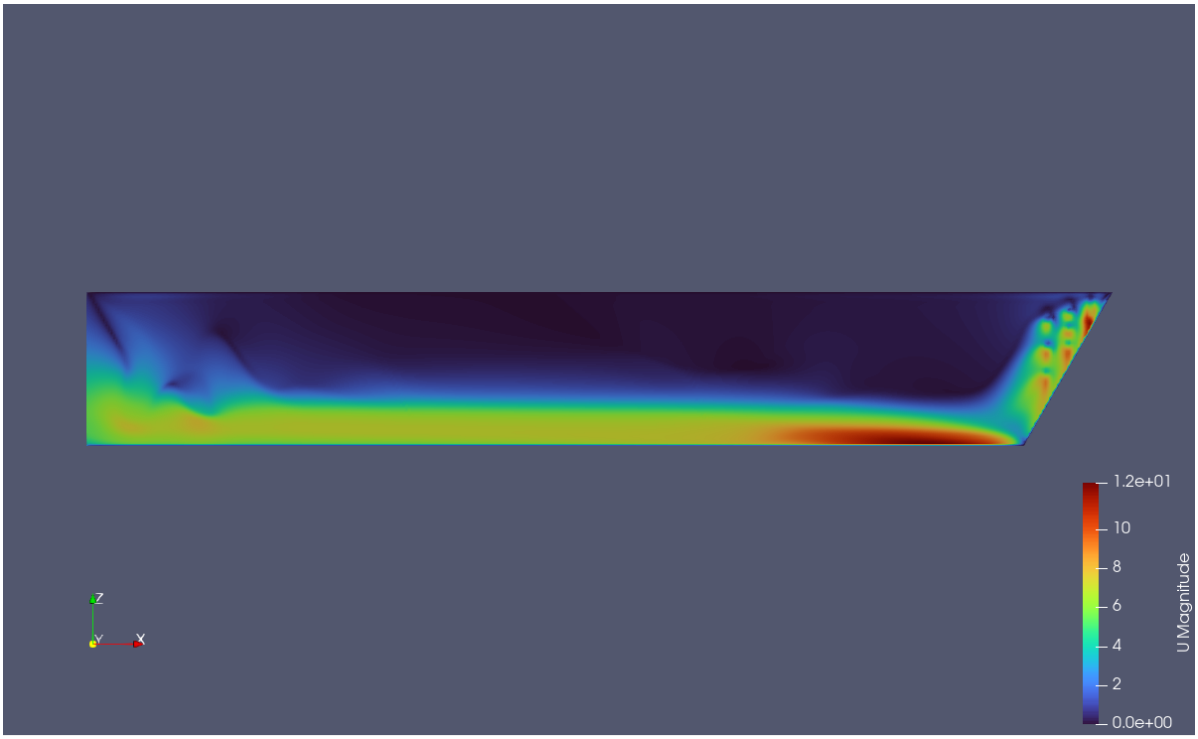

Figure D.3: Flow velocity magnitude scenario 2

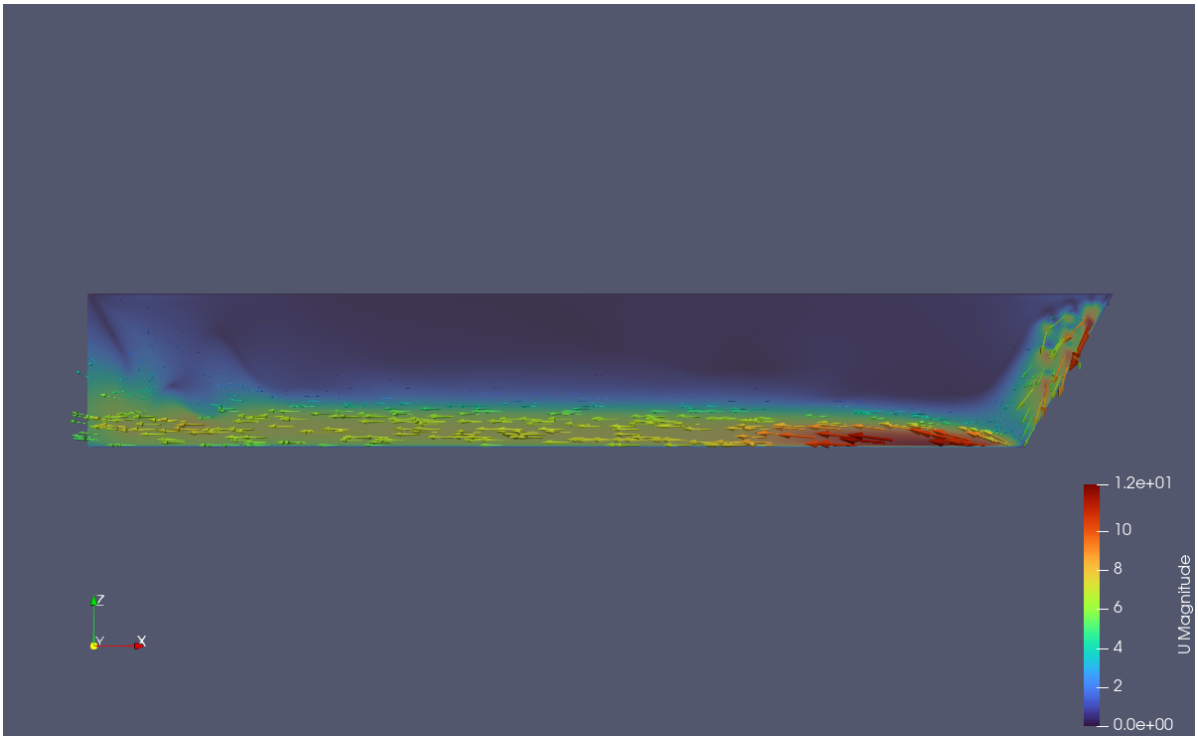

Figure D.4: Flow velocity direction scenario 2

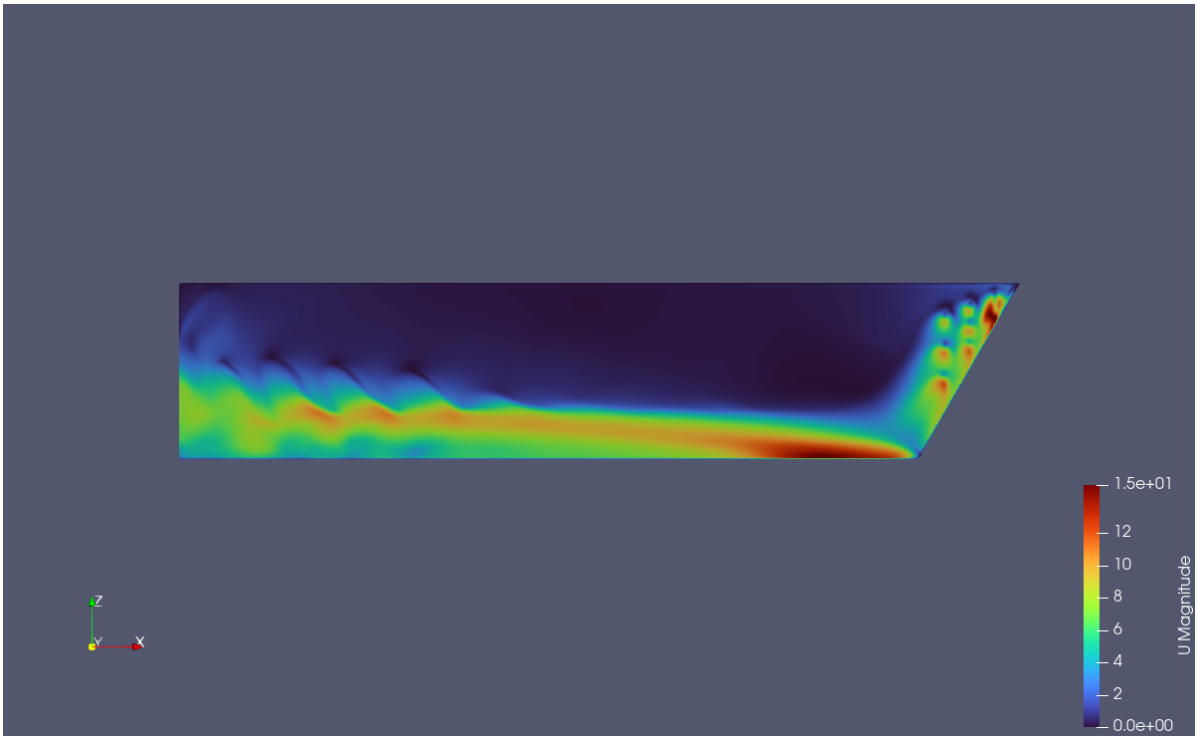

Figure D.5: Flow velocity magnitude scenario 3

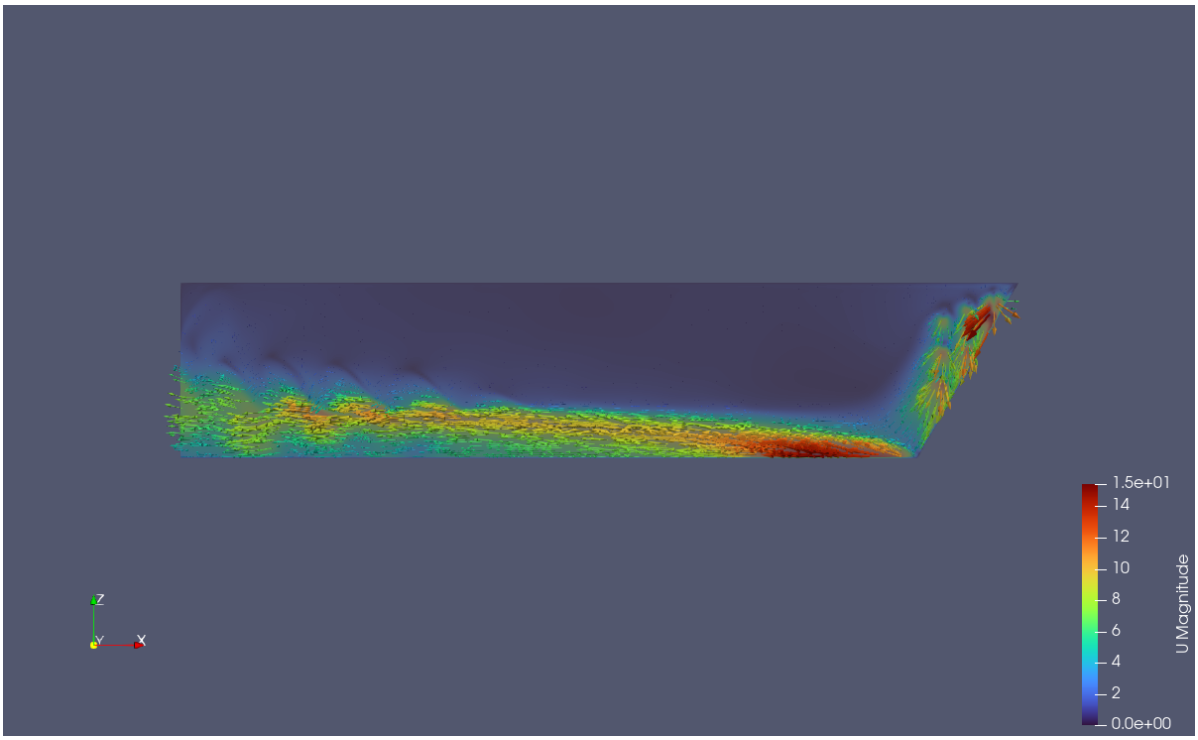

Figure D.6: Flow velocity direction scenario 3

E

Post-Processing

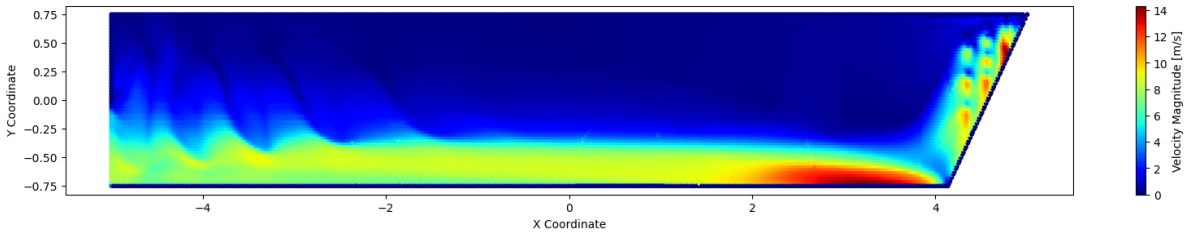

Figure E.1: Imported data paraView scenario 1

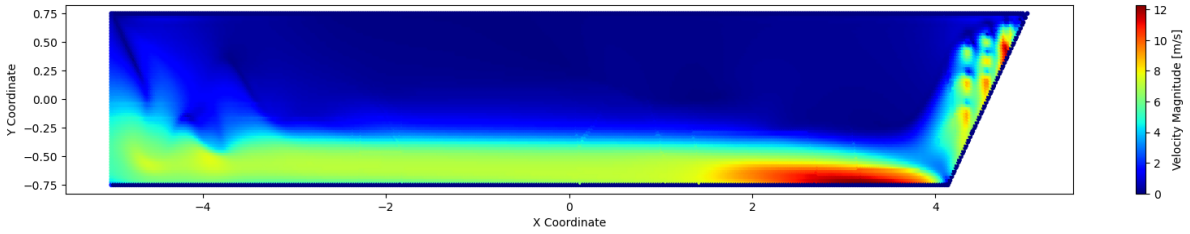

Figure E.2: Imported data paraView scenario 2

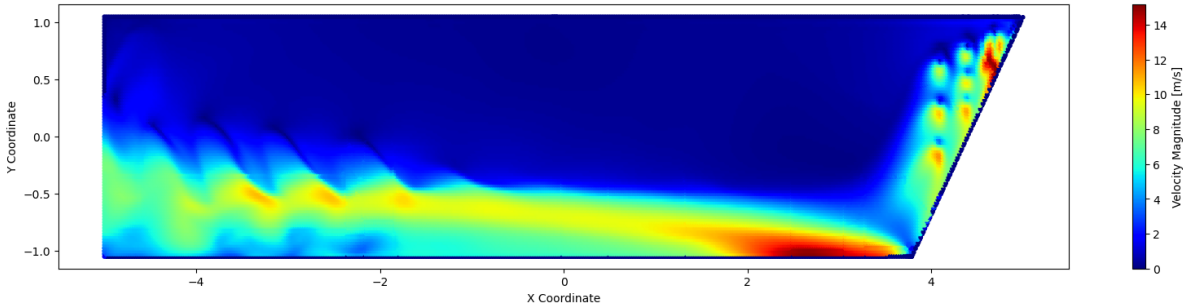

Figure E.3: Imported data paraView scenario 3

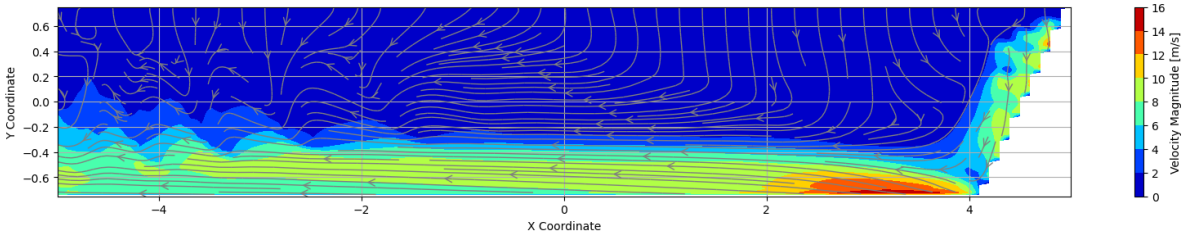

Figure E.4: Representation of the flowfield in Python scenario 1

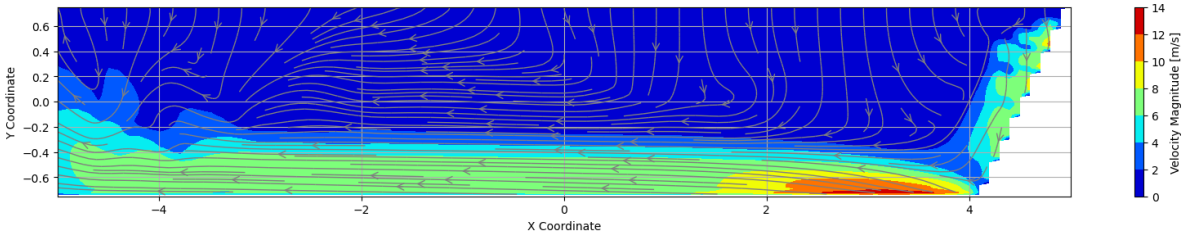

Figure E.5: Representation of the flowfield in Python scenario 2

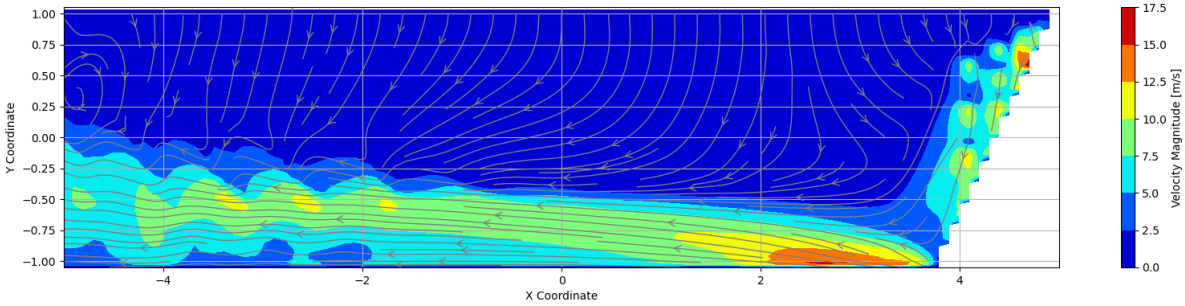

Figure E.6: Representation of the flowfield in Python scenario 3

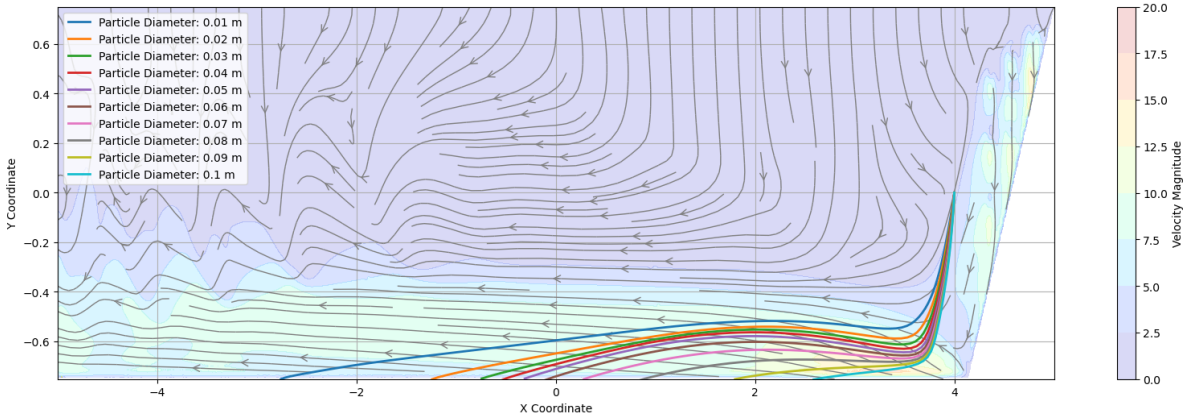

Figure E.7: Trajectories of particles with different particle size scenario 1

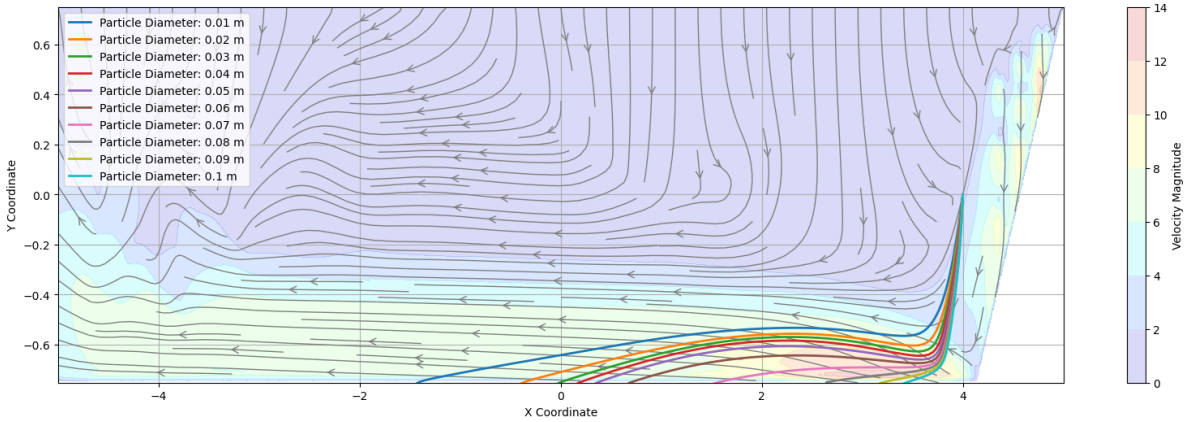

Figure E.8: Trajectories of particles with different particle size scenario 2

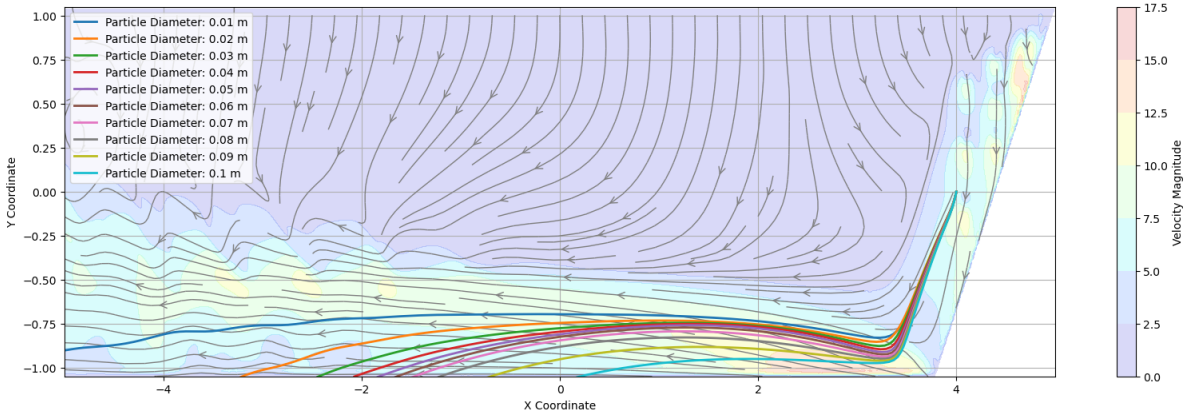

Figure E.9: Trajectories of particles with different particle size scenario 3

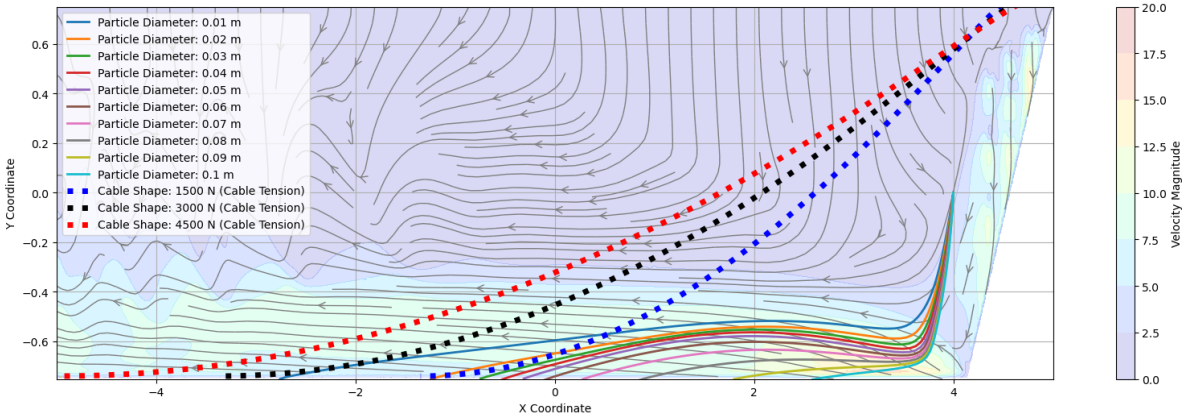

Figure E.10: Trajectory of particles with different particle size and cable shape scenario 1 (cable 1)

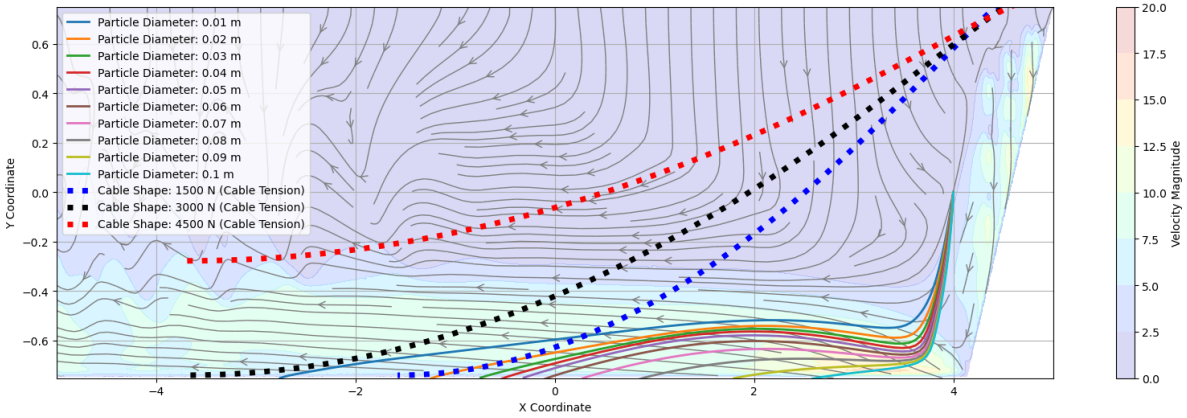

Figure E.11: Trajectory of particles with different particle size and cable shape scenario 1 (cable 2)

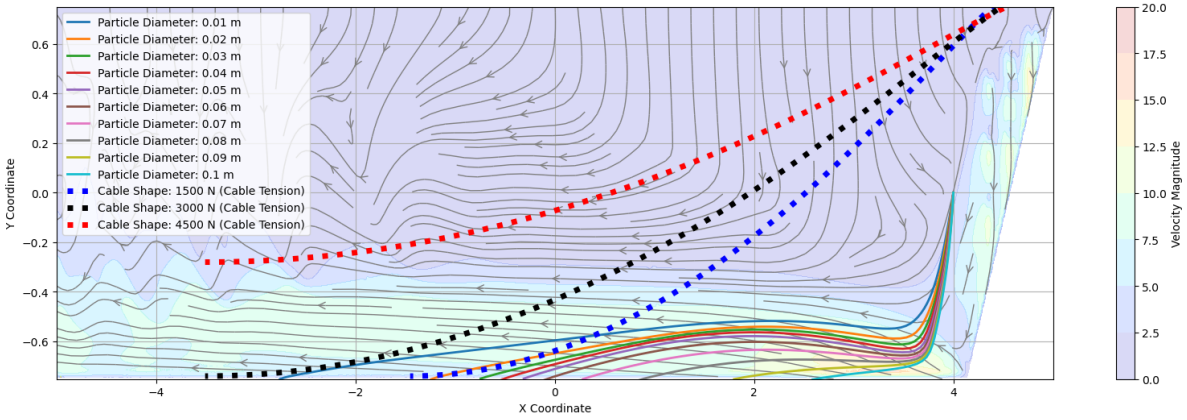

Figure E.12: Trajectory of particles with different particle size and cable shape scenario 1 (cable 3)

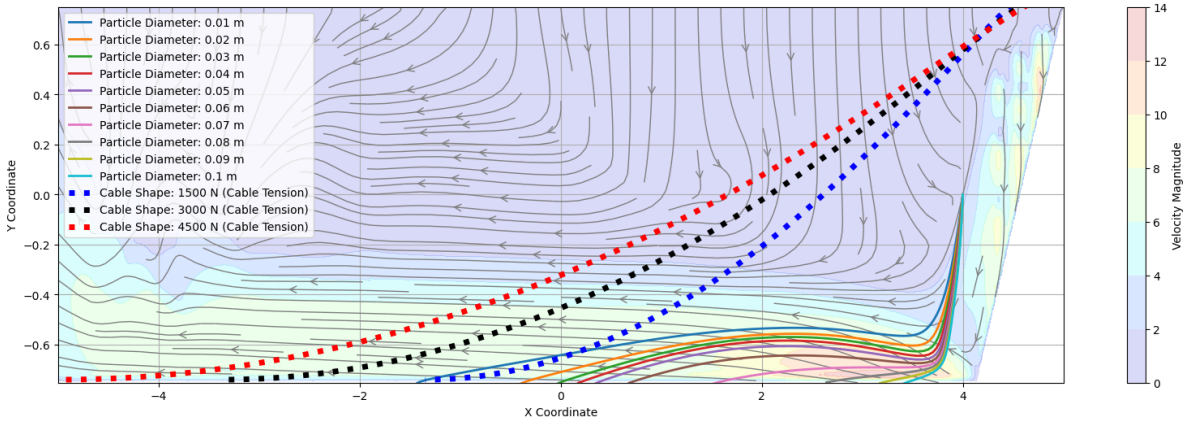

Figure E.13: Trajectory of particles with different particle size and cable shape scenario 2 (cable 1)

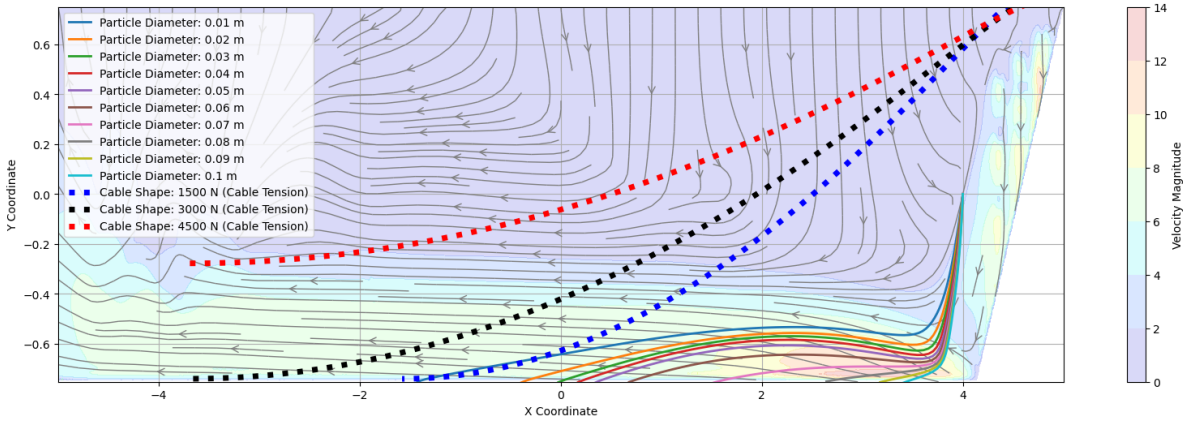

Figure E.14: Trajectory of particles with different particle size and cable shape scenario 2 (cable 2)

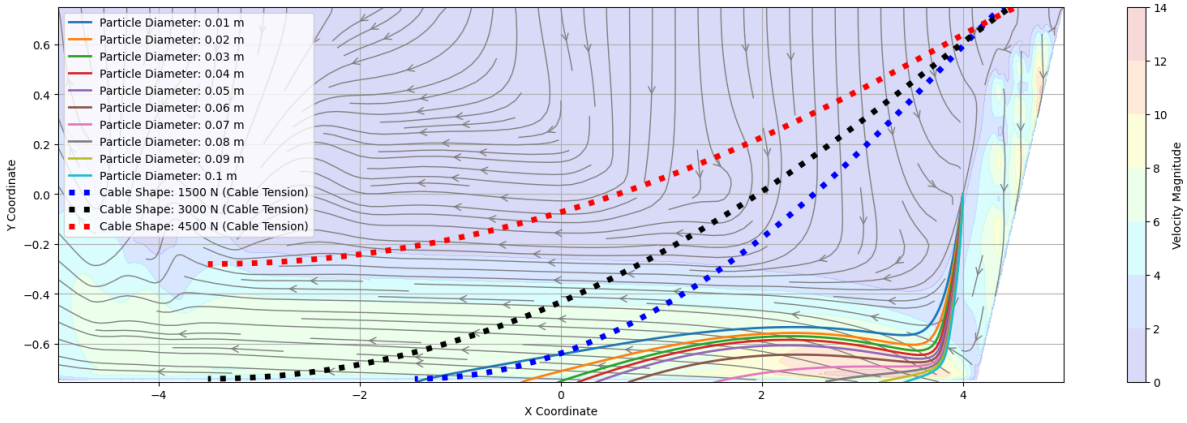

Figure E.15: Trajectory of particles with different particle size and cable shape scenario 2 (cable 3)

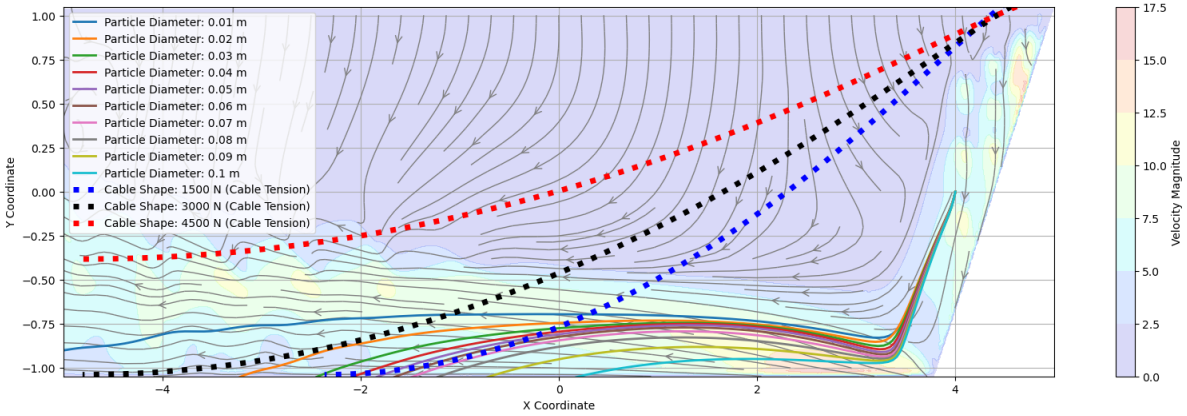

Figure E.16: Trajectory of particles with different particle size and cable shape scenario 3 (cable 1)

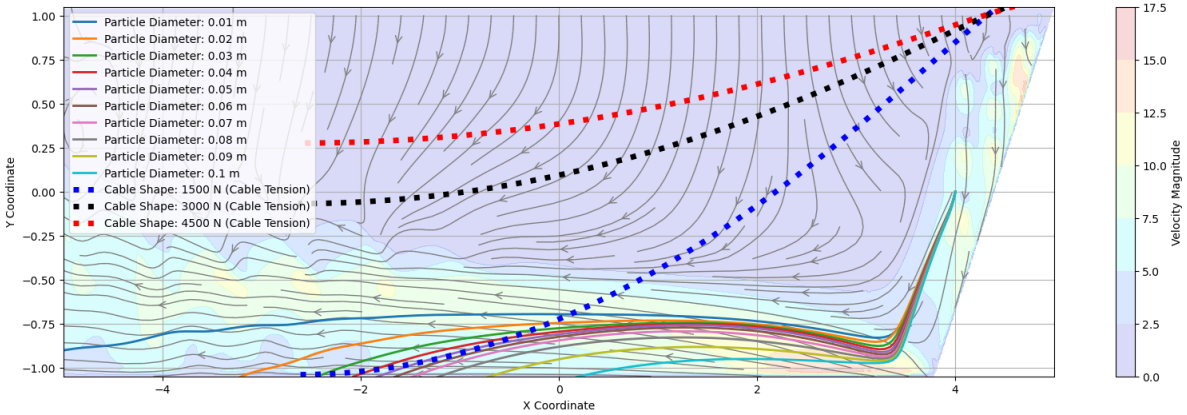

Figure E.17: Trajectory of particles with different particle size and cable shape scenario 3 (cable 2)

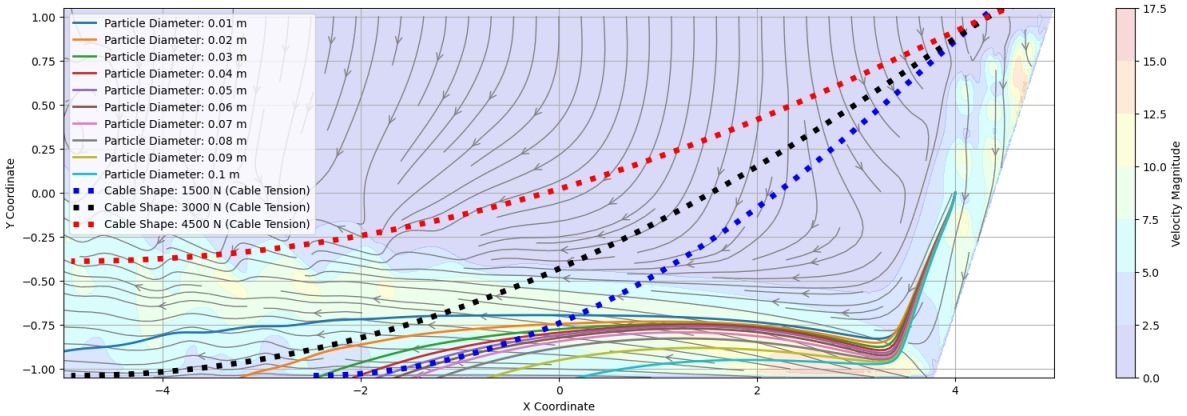

Figure E.18: Trajectory of particles with different particle size and cable shape scenario 3 (cable 3)

F

Loss of Burial Depth

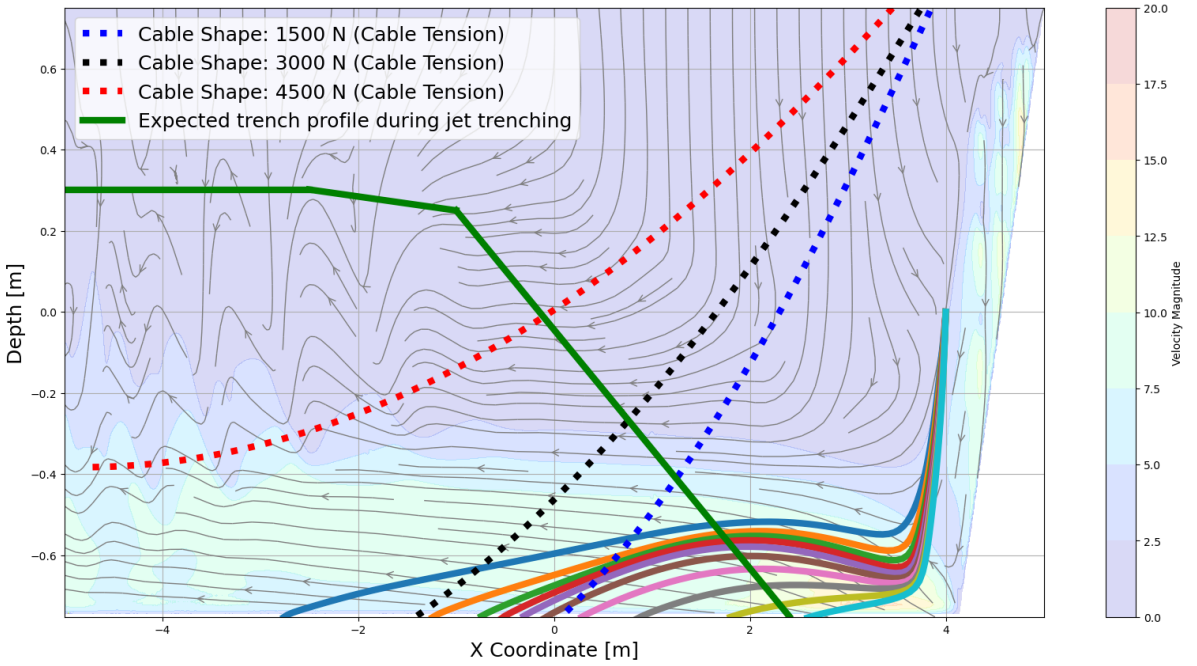

Figure F.1: Trajectory of particles with different particle size and cable shape scenario 1 (cable 1)

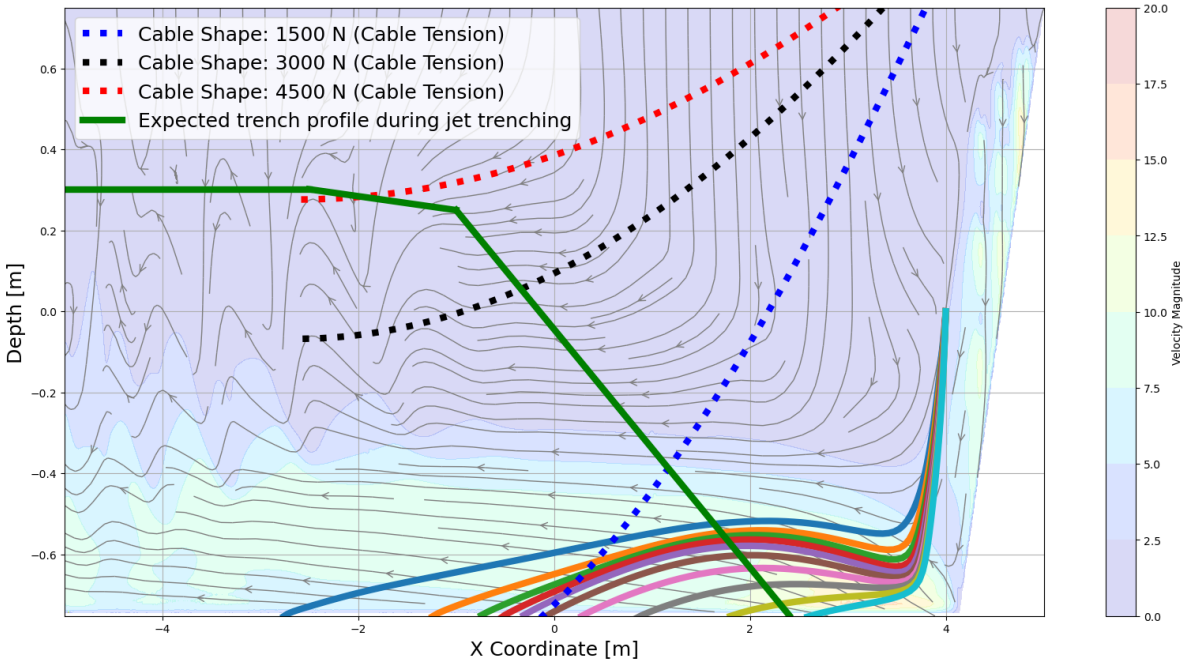

Figure F.2: Trajectory of particles with different particle size and cable shape scenario 1 (cable 2)

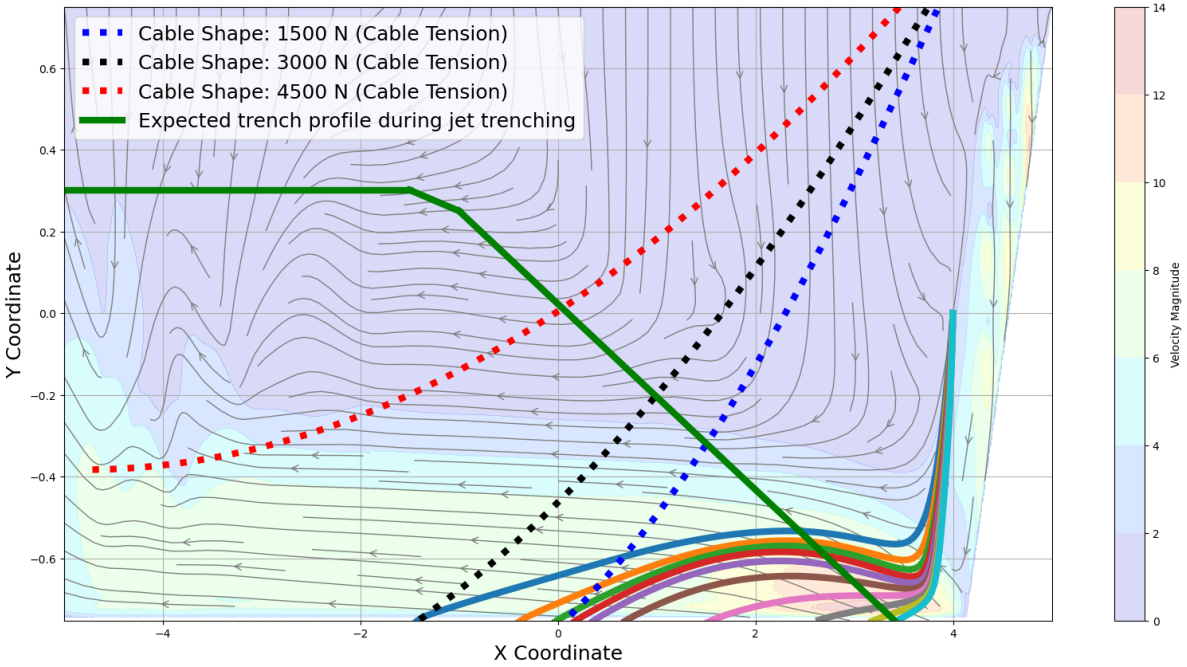

Figure F.3: Trajectory of particles with different particle size and cable shape scenario 2 (cable 1)

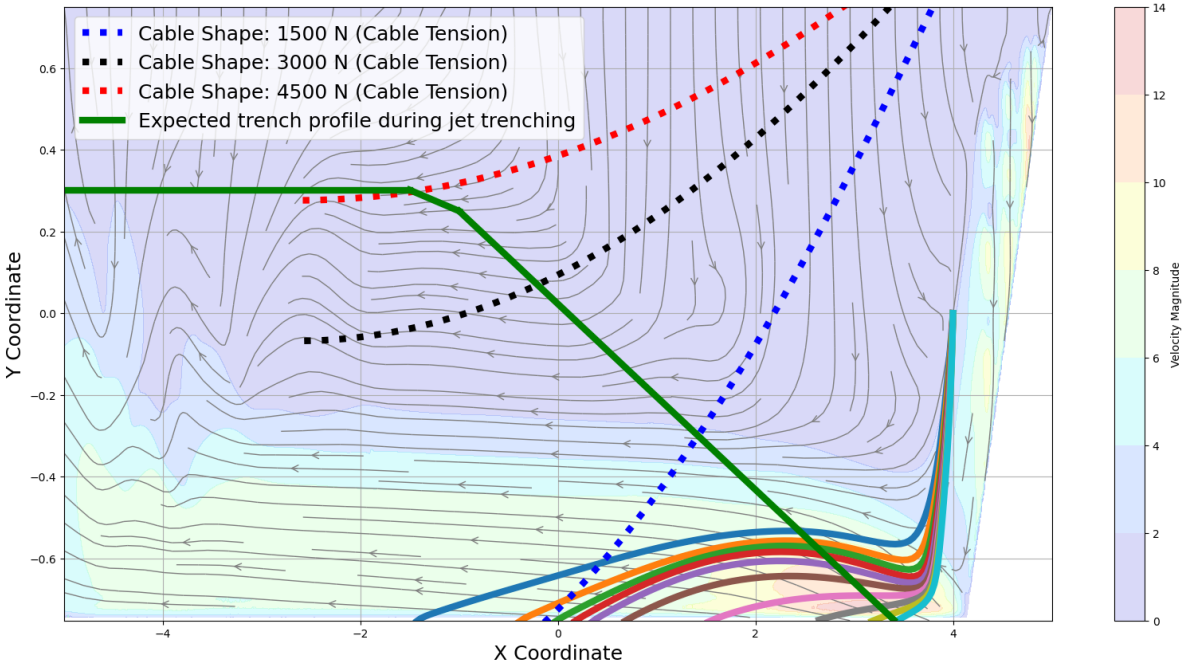

Figure F.4: Trajectory of particles with different particle size and cable shape scenario 2 (cable 2)

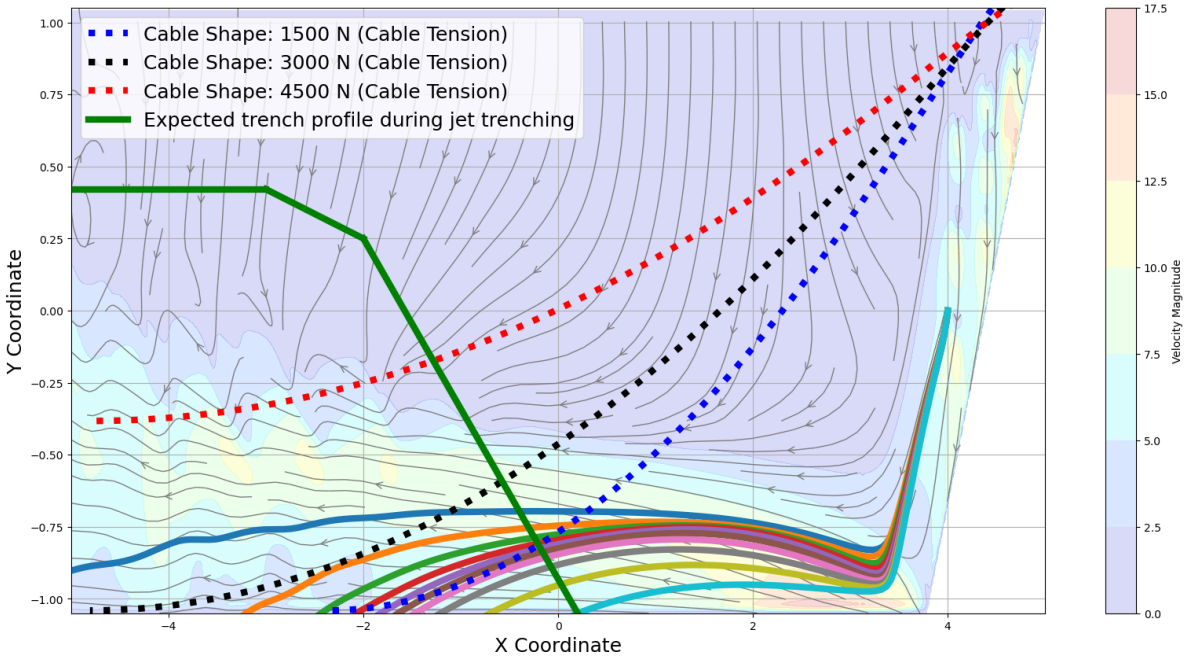

Figure F.5: Trajectory of particles with different particle size and cable shape scenario 3 (cable 1)

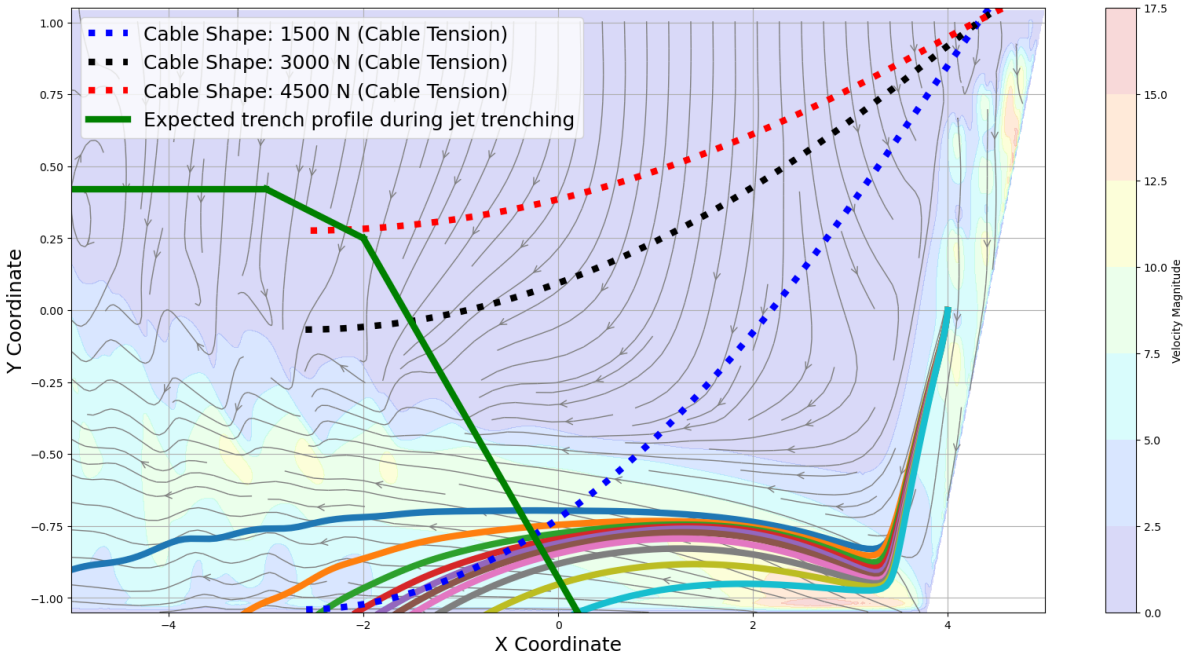

Figure F.6: Trajectory of particles with different particle size and cable shape scenario 3 (cable 2)

G

Python Code

```
import pandas as pd
import matplotlib.pyplot as plt
import matplotlib.colors as colors
from matplotlib.cm import ScalarMappable
import numpy as np
from scipy.interpolate import griddata
from scipy.ndimage import gaussian_filter
from scipy.interpolate import interp1d
import math
from IPython.display import display, HTML
display(HTML("<style>.container { width:100% !important; }</style>"))
```

Listing G.1: Import packages

```
df = pd.read_csv("Velocity_Data.csv")
df_WSS = pd.read_csv("wallShearStress.csv").dropna()
# Adding Velocity Magnitude
df['Velocity_Magnitude'] = np.sqrt(df['U:0']**2 + df['U:2']**2)
df
```

Listing G.2: Import data

```
# Wall shear stress at the bottom
WSS = df_WSS['wallShearStress:0']
x_WSS = df_WSS['Points:0']

# Shear stress on the bottom over the length of the trench
plt.figure(figsize=(20,4.2))
plt.plot(x_WSS,WSS, label = "Shear Stress at the bottom")
plt.xlim(-5,4)
plt.ylim(0,0.3)
plt.ylabel(r'$\tau$ [Pa]')
plt.xlabel('x-coordinate [m]')
plt.legend();
```

Listing G.3: Wall shear stress

```
# Create a Matplotlib figure and axis
fig, ax = plt.subplots(figsize=(20, 4.2))

# Plot the original grid points using a scatter plot
ax.scatter(df['Points:0'], df['Points:2'], c=df['Velocity_Magnitude'], cmap='jet', s
    =10, marker='o')

# Define a colormap and normalize velocity magnitude for the colorbar
cmap = plt.get_cmap('jet')
norm = colors.Normalize(vmin=df['Velocity_Magnitude'].min(), vmax=df['
    Velocity_Magnitude'].max())
```

```
10
11 # Create a dummy ScalarMappable object for colorbar
12 sm = ScalarMappable(cmap=cmap, norm=norm)
13 sm.set_array([])
14
15 # Add colorbar to indicate velocity magnitude
16 cbar = plt.colorbar(sm, orientation='vertical', ax=ax, label='Velocity Magnitude [m/s]'
       )
17
18 # Set labels for the x and y axes
19 ax.set_xlabel('X Coordinate')
20 ax.set_ylabel('Y Coordinate')
21
22 # Show the plot
23 plt.show()
24 # Create a Matplotlib figure and axis
25 fig, ax = plt.subplots(figsize=(20, 4.2))
26
27 # Define the grid for interpolation
28 x_grid = np.linspace(df['Points:0'].min(), df['Points:0'].max(), 100)
29 y_grid = np.linspace(df['Points:2'].min(), df['Points:2'].max(), 100)
30 x_grid, y_grid = np.meshgrid(x_grid, y_grid)
31
32 # Interpolate velocity components onto the grid
33 u_grid = griddata((df['Points:0'], df['Points:2']), df['U:0'], (x_grid, y_grid), method
       ='cubic')
34 v_grid = griddata((df['Points:0'], df['Points:2']), df['U:2'], (x_grid, y_grid), method
       ='cubic')
35
36 # Calculate velocity magnitude on the grid
37 velocity_magnitude = np.sqrt(u_grid**2 + v_grid**2)
38
39 # Create smoother streamlines
40 ax.streamplot(x_grid, y_grid, u_grid, v_grid, color='gray', linewidth=1, density=1.5,
       arrowstyle='->', arrowsize=1.5)
41
42 # Create a contour plot for velocity magnitude
43 contour = ax.contourf(x_grid, y_grid, velocity_magnitude, cmap='jet')
44 cbar = plt.colorbar(contour, orientation='vertical', ax=ax, label='Velocity Magnitude [
       m/s]')
45
46 # Set labels for the x and y axes
47 ax.set_xlabel('X Coordinate')
48 ax.set_ylabel('Y Coordinate')
49
50 # Add grid lines
51 plt.grid()
52
53 # Set axis limits
54 plt.xlim(df['Points:0'].min(), df['Points:0'].max())
55 plt.ylim(df['Points:2'].min(), df['Points:2'].max())
56
57 # Show the plot
58 plt.show()
```

Listing G.4: Setting up flowfield

```
1 # Create the grid for interpolation
2 interpolation_grid = (df['Points:0'], df['Points:2'])
3
4 # Function to interpolate velocity & WSS at a given point
5 def interpolate_velocity(x, y):
6     u = griddata(interpolation_grid, df['U:0'], (x, y), method='cubic')
7     v = griddata(interpolation_grid, df['U:2'], (x, y), method='cubic')
8     return u, v
9
10 # Function for the relative Velocity
11 def relative_velocity(flow_velocity, particle_velocity):
12     V = flow_velocity - particle_velocity
13     return V
```

```

# Function for the acceleration due to drag
def drag_acceleration(relative_velocity):
    drag_force =  0.5 * water_density * relative_velocity * abs(relative_velocity) *
    drag_coefficient * particle_area
    a_drag = drag_force / particle_mass
    return a_drag

# Create an interpolation function with extrapolation allowed
interpolation_function = interp1d(x_WSS, WSS, kind='cubic', bounds_error=False)

# Define a function that takes an x value and returns the interpolated WSS value
def get_interpolated_WSS(x):
    return abs(interpolation_function(x))
```

Listing G.5: Functions

```
# Parameters
particle_radius = np.linspace(0.005, 0.05, 10) #np.array([0.01, 0.025, 0.05])  # Radius
     of the particle (adjust as needed) [m]
particle_area = np.pi * particle_radius ** 2  # Cross-sectional area for drag force [m2
    ]
water_density = 1025  # Density of sea water [kg/m3]
particle_density = 1600  # Density of the clay [kg/m3]
gravity = 9.81  # Acceleration due to gravity [m/s2]
drag_coefficient = 0.47  # Drag coefficient (adjust as needed)
particle_mass = 4 / 3 * np.pi * particle_radius ** 3 * particle_density  # Mass of the
    particle [kg]
# Function for Shields parameter
def theta(x, D):
    theta = get_interpolated_WSS(x) / ((particle_density - water_density) * D)
    return theta

# Critical Shields parameter
theta_c = 0.06 # For particles with diameter larger than 5 mm

# Create a single figure to contain all the plots
plt.figure(figsize=(20, 5))

# Loop over different particle radii
for i in particle_radius:
    x = np.linspace(-5, 5)
    plt.plot(x, theta(x, D=2 * i), label=f"Diameter {round(2 * i, 2)} m")

# Plot the critical Shields parameter as a horizontal line
plt.hlines(theta_c, -5, 5, color="red", label="Shields Criterion")

# Add legend, labels, and axis limits
plt.legend(loc='center right')
plt.xlim(-5, 5)
plt.xlabel('x-coordinate')
plt.ylabel('Shields Parameter')
plt.title('Shields Parameter vs. x-coordinate for Different Particle Diameters')

# Show the combined plot
plt.show()
```

Listing G.6: Simulation for clay blocks

```
# Parameters
particle_radii = np.linspace(0.005, 0.05, 10)  # List of particle radii (adjust as
    needed) [m]
water_density = 1025  # Density of sea water [kg/m3]
particle_density = 1600  # Density of the clay [kg/m3]
gravity = 9.81  # Acceleration due to gravity [m/s2]
drag_coefficient = 0.47  # Drag coefficient (adjust as needed)

# Lists to store the paths of particles for different radii
particle_paths = []

```

```
# Loop through different particle radii
for particle_radius in particle_radii:
    # Calculate particle area and mass for the current radius
    particle_area = np.pi * particle_radius ** 2  # Cross-sectional area for drag force [m2]
    particle_mass = 4 / 3 * np.pi * particle_radius ** 3 * particle_density  # Mass of the particle [kg]

    # Initial conditions
    start_x = 4  # Initial X-coordinate of the particle [m]
    start_y = 0  # Initial Y-coordinate of the particle [m]
    dt = 0.01  # Time step (smaller value for smoother path, larger value for faster computation) [s]

    # Lists to store the path of the particle
    path_x = [start_x]
    path_y = [start_y]

    # Starting particle velocities
    x_dot, y_dot = 0, 0

    # Verlet integration
    while start_y >= -1.05:
        u, v = interpolate_velocity(start_x, start_y)

        # Relative velocity
        V_rel_x = relative_velocity(u, x_dot)
        V_rel_y = relative_velocity(v, y_dot)

        # Acceleration
        a_x = drag_acceleration(V_rel_x)
        a_y = drag_acceleration(V_rel_y) - gravity

        # New points
        start_x += x_dot * dt + (1/2) * a_x * dt ** 2
        start_y += y_dot * dt + (1/2) * a_y * dt ** 2

        # New velocities
        x_dot += a_x * dt
        y_dot += a_y * dt

        # Append the current position to the path
        path_x.append(start_x)
        path_y.append(start_y)

    # Append the path of the particle to the list of particle paths
    particle_paths.append((path_x, path_y))

    import matplotlib.pyplot as plt

# Create a Matplotlib figure and axis
fig, ax = plt.subplots(figsize=(20, 6))

# Define the grid for interpolation (you can adjust this based on your data)
x_grid = np.linspace(df['Points:0'].min(), df['Points:0'].max(), 1000)
y_grid = np.linspace(df['Points:2'].min(), df['Points:2'].max(), 200)
x_grid, y_grid = np.meshgrid(x_grid, y_grid)

# Interpolate velocity components onto the grid (you should replace this with your actual data)
u_grid = griddata((df['Points:0'], df['Points:2']), df['U:0'], (x_grid, y_grid), method='cubic')
v_grid = griddata((df['Points:0'], df['Points:2']), df['U:2'], (x_grid, y_grid), method='cubic')

# Calculate velocity magnitude on the grid
velocity_magnitude = np.sqrt(u_grid**2 + v_grid**2)

# Create smoother streamlines (you can adjust these settings)
ax.streamplot(x_grid, y_grid, u_grid, v_grid, color='gray', linewidth=1, density=1.5, arrowstyle='->', arrowsize=1.5)
```

```

# Create a contour plot for velocity magnitude (you can adjust the colormap and alpha)
contour = ax.contourf(x_grid, y_grid, velocity_magnitude, cmap='jet', alpha=0.15)
cbar = plt.colorbar(contour, orientation='vertical', ax=ax, label='Velocity Magnitude')

# Set labels for the x and y axes
ax.set_xlabel('X Coordinate')
ax.set_ylabel('Y Coordinate')

# Add grid lines
plt.grid()

# Set axis limits (you can adjust these based on your data)
plt.xlim(df['Points:0'].min(), df['Points:0'].max())
plt.ylim(df['Points:2'].min(), df['Points:2'].max())

# Plot the paths for different radii with custom colors and labels
for i, (path_x, path_y) in enumerate(particle_paths):
    ax.plot(path_x, path_y, label=f'Particle Diameter: {round(2*particle_radii[i],2)} m', linewidth=2)



# Create a legend
ax.legend(loc='upper left')

# Show the plot
plt.show()
```

Listing G.7: Flow path of clay particles of different diameter

```
def cable_def(x, L):
    z = -((q * L / T) * np.sqrt(EI / T) * (np.cosh(np.sqrt(T * L / EI)) / np.sinh(np.sqrt(T * L / EI))) *
         (np.cosh(np.sqrt(T * x / EI)) - np.tanh(np.sqrt(T * L / EI)) * np.sinh(np.sqrt(T * x / EI)) - 1) -
         (q / (2 * T)) * x ** 2 + q * L * x / T)
    return z
# Constants
q = 155  # Cable weight per unit length (N/m)
T = 1000  # Tension in the cable (N)
EI = 2700  # Bending stiffness (Nm^2)
for i in np.linspace(0,10,10000):
    if -2.11 < cable_def(i,i) < -2.09:
        L = i
        print(L)
        break
import matplotlib.pyplot as plt

# Create a Matplotlib figure and axis
fig, ax = plt.subplots(figsize=(20, 6))

# Define the grid for interpolation (you can adjust this based on your data)
x_grid = np.linspace(df['Points:0'].min(), df['Points:0'].max(), 1000)
y_grid = np.linspace(df['Points:2'].min(), df['Points:2'].max(), 200)
x_grid, y_grid = np.meshgrid(x_grid, y_grid)

# Interpolate velocity components onto the grid (you should replace this with your actual data)
u_grid = griddata((df['Points:0'], df['Points:2']), df['U:0'], (x_grid, y_grid), method='cubic')
v_grid = griddata((df['Points:0'], df['Points:2']), df['U:2'], (x_grid, y_grid), method='cubic')

# Calculate velocity magnitude on the grid
velocity_magnitude = np.sqrt(u_grid**2 + v_grid**2)

# Create smoother streamlines (you can adjust these settings)
ax.streamplot(x_grid, y_grid, u_grid, v_grid, color='gray', linewidth=1, density=1.5, arrowstyle='->', arrowsize=1.5)
```

```
34
35 # Create a contour plot for velocity magnitude (you can adjust the colormap and alpha)
36 contour = ax.contourf(x_grid, y_grid, velocity_magnitude, cmap='jet', alpha=0.15)
37 cbar = plt.colorbar(contour, orientation='vertical', ax=ax, label='Velocity Magnitude')
38
39 # Set labels for the x and y axes
40 ax.set_xlabel('X Coordinate')
41 ax.set_ylabel('Y Coordinate')
42
43 # Add grid lines
44 plt.grid()
45
46 # Set axis limits (you can adjust these based on your data)
47 plt.xlim(df['Points:0'].min(), df['Points:0'].max())
48 plt.ylim(df['Points:2'].min(), df['Points:2'].max())
49
50 # Plot the paths for different radii with custom colors and labels
51 for i, (path_x, path_y) in enumerate(particle_paths):
52     ax.plot(path_x, path_y, label=f'Particle Diameter: {round(2*particle_radii[i],2)} m
    ', linewidth=2)
53
54 # Plot cable shape as calculated above
55 ax.plot(-x+5, cable_def(x, L)+1.05, linewidth=5, linestyle=":", color='black', label="
    Cable Shape")
56
57
58 # Create a legend
59 ax.legend(loc='upper left')
60
61 # Show the plot
62 plt.show()
```

Listing G.8: Cable definition and plots

```
1 # Create a Matplotlib figure and axis
2 fig, ax = plt.subplots(figsize=(20, 6))
3
4 # Define the grid for interpolation (you can adjust this based on your data)
5 x_grid = np.linspace(df['Points:0'].min(), df['Points:0'].max(), 1000)
6 y_grid = np.linspace(df['Points:2'].min(), df['Points:2'].max(), 200)
7 x_grid, y_grid = np.meshgrid(x_grid, y_grid)
8
9 # Interpolate velocity components onto the grid (you should replace this with your
    actual data)
10 u_grid = griddata((df['Points:0'], df['Points:2']), df['U:0'], (x_grid, y_grid), method
    ='cubic')
11 v_grid = griddata((df['Points:0'], df['Points:2']), df['U:2'], (x_grid, y_grid), method
    ='cubic')
12
13 # Calculate velocity magnitude on the grid
14 velocity_magnitude = np.sqrt(u_grid**2 + v_grid**2)
15
16 # Create smoother streamlines (you can adjust these settings)
17 ax.streamplot(x_grid, y_grid, u_grid, v_grid, color='gray', linewidth=1, density=1.5,
    arrowstyle='->', arrowsize=1.5)
18
19 # Create a contour plot for velocity magnitude (you can adjust the colormap and alpha)
20 contour = ax.contourf(x_grid, y_grid, velocity_magnitude, cmap='jet', alpha=0.15)
21 cbar = plt.colorbar(contour, orientation='vertical', ax=ax, label='Velocity Magnitude')
22
23 # Set labels for the x and y axes
24 ax.set_xlabel('X Coordinate')
25 ax.set_ylabel('Y Coordinate')
26
27 # Add grid lines
28 plt.grid()
29
30 # Set axis limits (you can adjust these based on your data)
31 plt.xlim(df['Points:0'].min(), df['Points:0'].max())
32 plt.ylim(df['Points:2'].min(), df['Points:2'].max())
```

```

# Plot the paths for different radii with custom colors and labels
for i, (path_x, path_y) in enumerate(particle_paths):
    ax.plot(path_x, path_y, label=f'Particle Diameter: {round(2*particle_radii[i],2)} m
    ', linewidth=2)

# Plot cable shape as calculated above
colors = ['blue', 'black', 'red']
T_values = [1500, 3000, 4500]
for i, T in enumerate(T_values):
    for j in np.linspace(0,10,10000):
        if -2.11 < cable_def(j,j) < -2.09:
            L = j
            break
    x = np.linspace(0,L,1000)
    ax.plot(-x+5, cable_def(x, L)+1.05, linewidth=5, linestyle=":", color=colors[i],
    label=f"Cable Shape: {T} N (Cable Tension)")



# Create a legend
ax.legend(loc='upper left')

# Show the plot
plt.show()
```

Listing G.9: Cable range

```
# Create a Matplotlib figure and axis
fig, ax = plt.subplots(figsize=(20, 6))

# Define the grid for interpolation (you can adjust this based on your data)
x_grid = np.linspace(df['Points:0'].min(), df['Points:0'].max(), 1000)
y_grid = np.linspace(df['Points:2'].min(), df['Points:2'].max(), 200)
x_grid, y_grid = np.meshgrid(x_grid, y_grid)

# Interpolate velocity components onto the grid (you should replace this with your
    actual data)
u_grid = griddata((df['Points:0'], df['Points:2']), df['U:0'], (x_grid, y_grid), method
    ='cubic')
v_grid = griddata((df['Points:0'], df['Points:2']), df['U:2'], (x_grid, y_grid), method
    ='cubic')

# Calculate velocity magnitude on the grid
velocity_magnitude = np.sqrt(u_grid**2 + v_grid**2)

# Create smoother streamlines (you can adjust these settings)
ax.streamplot(x_grid, y_grid, u_grid, v_grid, color='gray', linewidth=1, density=1.5,
    arrowstyle='->', arrowsize=1.5)

# Create a contour plot for velocity magnitude (you can adjust the colormap and alpha)
contour = ax.contourf(x_grid, y_grid, velocity_magnitude, cmap='jet', alpha=0.15)
cbar = plt.colorbar(contour, orientation='vertical', ax=ax, label='Velocity Magnitude')

# Set labels for the x and y axes
ax.set_xlabel('X Coordinate')
ax.set_ylabel('Y Coordinate')

# Add grid lines
plt.grid()

# Set axis limits (you can adjust these based on your data)
plt.xlim(df['Points:0'].min(), df['Points:0'].max())
plt.ylim(df['Points:2'].min(), df['Points:2'].max())

# Plot the paths for different radii with custom colors and labels
for i, (path_x, path_y) in enumerate(particle_paths):
    ax.plot(path_x, path_y, label=f'Particle Diameter: {round(2*particle_radii[i],2)} m
    ', linewidth=2)

```

```
# Plot cable shape as calculated above
colors = ['blue', 'black', 'red']
T_values = [1500, 3000, 4500]
for i, T in enumerate(T_values):
    for j in np.linspace(0,10,10000):
        if -2.11 < cable_def(j,j) < -2.09:
            L = j
            break
    x = np.linspace(0,L,1000)
    ax.plot(-x+5, cable_def(x, L)+1.05, linewidth=5, linestyle=":", color=colors[i],
    label=f"Cable Shape: {T} N (Cable Tension)")



# Create a legend
ax.legend(loc='upper left')

# Show the plot
plt.show()
```

Listing G.10: Cable range